Trends of stratospheric chlorine and fluorine reservoir species

Zur Erlangung des akademischen Grades eines
DOKTORS DER NATURWISSENSCHAFTEN
von der Fakultät für Physik des
Karlsruher Instituts für Technologie

genehmigte

DISSERTATION

von

Dipl.-Met. Regina Kohlhepp
aus Wolfratshausen

Tag der mündlichen Prüfung:	6. Juli 2012
Referent:	Prof. Dr. Herbert Fischer
Korreferent:	PD Dr. Michael Höpfner

Abstract

In the present thesis, ground-based measurements with Fourier transform infrared (FTIR) spectrometers are evaluated and compared with calculations by atmospheric models of different architecture. The species of primary interest are the chlorine and fluorine reservoir gases hydrogen chloride (HCl), chlorine nitrate ($ClONO_2$), and hydrogen fluoride (HF). Their source gases are mainly anthropogenic chlorofluorocarbons (CFCs), hydrochlorofluorocarbons (HCFCs), and halons, which are so-called ozone-depleting substances. Because of this property, their emission was restricted in the Montreal Protocol in 1987 and its amendments and adjustments, leading to a subsequent phase-out. As a result of these reductions in the source gas emissions, the stratospheric inorganic chlorine content decreases with time since the late 1990s. This decline is confirmed by the FTIR measurements of HCl and $ClONO_2$ total column abundances reported in the present thesis, at nearly all of the 17 measurement sites taking part in this study and belonging to the Network for the Detection of Atmospheric Composition Change (NDACC). The calculations of five atmospheric chemistry models (i.e., the Bremen 2-D model, KASIMA, SLIMCAT, EMAC, and SOCOL) reproduce this decrease. The main reason for including HF in this comparison study of models and measurements is that this substance is an indicator of anthropogenic influences. Besides, it is often used as a tracer due to its high stability and a resulting long stratospheric lifetime. Although the emission of fluorine is not explicitly prohibited because it practically does not deplete stratospheric ozone, HF is expected to be also influenced by the Montreal protocol and its amendments because some of its source gases are restricted. However, CFC substitutes (e.g., hydrofluorocarbons) are allowed to contain fluorine so that the HF total column abundance is expected to have reached its peak value later than the two chlorine species. This can also be confirmed with the here-presented FTIR measurements and reproduced by the atmospheric models. In addition to the overall temporal evolution and absolute total column abundances of the three species, also the mean seasonal cycle of models and measurements at the 17 NDACC sites is compared.

Trends from the above-described model and measurement time series are calculated by fitting a linear function combined with a (third- or first-order) Fourier series accounting for the seasonal cycle of the species to the available data between 2000 and 2009. The error bars for the trends are determined with a bootstrap method. The influence of the type of fitting function, of time series length, the time period used, and sampling on the resulting trend and its confidence intervals is investigated. Furthermore, by multiple linear regression, the effect on the trend of including time series representing the 11-year solar variation and the quasi-biennial oscillation in the fitting function is studied.

The trends of HCl and $ClONO_2$ from models and measurements for the period 2000–2009 amount to roughly about -1 and -2%/yr, respectively, while HF increases by about 1%/yr during this period. However, there are differences between the measured trends and those simulated by the models. In the HCl and $ClONO_2$ measurements, the calculated trends exhibit a dependence on hemisphere, with a stronger decrease in the northern than in the southern hemisphere. Analogously, the measured HF increase is stronger in the southern than in the northern hemisphere. These differences can be attributed to the time required for transport from the emission sources of the organic chlorine and fluorine species, which are mostly located in the northern hemisphere, to the southern hemisphere. This results in later peaks of stratospheric inorganic chlorine and fluorine in the southern than in the northern hemisphere. The models obviously do not include this effect. Furthermore, the $ClONO_2$ trends from the FTIR measurements depend on latitude, with the strongest decreases at high and low latitudes, which is reproduced only by some of the models. Trends for the time range 2004–2009 show no significant trend or even a decrease of HF at many northern hemisphere sites. This confirms the stabilisation of the HF total column abundance in the northern hemisphere during the last few years.

The second part of the present thesis investigates the difference between the trends of HCl and $ClONO_2$ that was found before for example in the Kiruna data by Mikuteit (2008) and Kohlhepp et al. (2011). Also in the analyses described above, the $ClONO_2$ total column abundance decreases stronger than the HCl abundance in the FTIR total column measurements at most of the included NDACC sites, and also in the model results. In the reactions forming HCl and $ClONO_2$, methane (CH_4) and nitrous oxide (N_2O) are involved, the latter only indirectly via NO_2. This is why sensitivity studies with the EMAC (ECHAM/MESSy Atmospheric Chemistry) model are conducted by analysing trends between 2000 and 2050 from a long-term simulation where CH_4 and N_2O increase according to the A1B scenario from IPCC (2007), and from two other simulations where once CH_4 and once N_2O were kept fixed on their value of the year 2000. These studies reveal a strong influence of the considerable CH_4 increase during 2000–2050 in the reference simulation on chlorine partitioning into HCl and $ClONO_2$. Although the stratospheric temperature decrease with time present in all three simulations is expected to result in an enhancement of $ClONO_2$ production, HCl is strongly favoured if CH_4 increases at the rate projected by the A1B scenario. Examination of FTIR trends of HCl and $ClONO_2$ during a period of constant atmospheric CH_4 abundance (about 1999 to 2006 in the troposphere) leads to the conclusion that some of the observed changes in the measured chlorine trends above Kiruna may indeed be attributable to CH_4. In contrast, at the Jungfraujoch, the CH_4 influence may be ruled out by the peak in stratospheric inorganic chlorine occurring at the end of the 1990s.

Kurzfassung

Im Rahmen der vorliegenden Arbeit werden bodengebundene Messungen mit Fourier-Transformations-Infrarot-(FTIR-)Spektrometern durchgeführt und untersucht und mit den Ergebnissen verschiedener Atmosphärenmodelle verglichen. Das Augenmerk liegt hierbei auf Gesamtsäulengehalten der Chlor- bzw. Fluor-Reservoir-Spezies Chlorwasserstoff (HCl), Chlornitrat ($ClONO_2$) und Fluorwasserstoff (HF). Deren Hauptquellen sind anthropogene Fluorchlorkohlenwasserstoffe (FCKW), teilhalogenierte FCKW und Halone, also bromhaltige Halogenverbindungen. Da Chlor eine wichtige Rolle in der globalen Zerstörung der stratosphärischen Ozonschicht spielt, wurde die Emission der wichtigsten seiner auch als ODS (ozone-depleting substances) bezeichneten Vorläufergase im Jahre 1987 im Rahmen eines internationalen Abkommens zunächst eingeschränkt und im Folgenden vollständig verboten. Dieses sogenannte Montrealer Protokoll und seine nachfolgenden Ergänzungen führten schließlich zu einer Verringerung des stratosphärischen Chlorgehalts seit etwa Ende der 1990er Jahre. Die im Rahmen dieser Arbeit durchgeführten Auswertungen von Zeitreihen bodengebundener FTIR-Messungen von HCl und $ClONO_2$ an 17 Stationen des globalen Messnetzwerks NDACC (Network for the Detection of Atmospheric Composition Change) bestätigen diese Abnahme. Auch die fünf globalen Atmosphärenmodelle, von denen ebenfalls Ergebnisse vorliegen (das Bremer 2-D-Modell, KASIMA, SLIMCAT, EMAC und SOCOL) reproduzieren diesen Verlauf. Im Gegensatz zu Chlor ist Fluor nicht an der Ozonzerstörung beteiligt und deshalb seine Emission im Montrealer Protokoll nicht explizit verboten. Trotzdem wird erwartet, dass HF ebenfalls durch diese internationalen Abkommen beeinflusst wird, weil die verbotenen ODS auch zu seinen Hauptquellen zählen. Ein weiterer Grund für das Interesse an der zeitlichen Entwicklung von HF ist, dass es wegen seiner hohen Stabilität in der Stratosphäre häufig als sogenannter Tracer verwendet wird. Da Fluor auch beispielsweise in FCKW-Ersatzstoffen enthalten ist (z.B. in teilhalogenierten Fluorkohlenwasserstoffen), wird erwartet, dass der atmosphärische HF-Gehalt erst einige Jahre nach dem der beiden untersuchten Chlorspezies abzunehmen beginnt.

Im Rahmen des oben beschriebenen Vergleichs von Modell- und Messdaten wird nicht nur die generelle zeitliche Entwicklung der drei Spezies verglichen, sondern auch quantitativ die resultierenden Gesamtsäulengehalte und zudem die mittleren Jahresgänge an den 17 NDACC-Stationen. Der Schwerpunkt liegt jedoch auf der Bestimmung von Trends zwischen den Jahren 2000 und 2009. Diese werden durch Anpassung einer linearen Funktion berechnet, die mit einer Fourierreihe erster oder dritter Ordnung kombiniert wird, um den Jahresgang zu repräsentieren. Die Konfidenzintervalle werden mit Hilfe einer sogenannten Bootstrap-Methode ermittelt. Es wird gezeigt, inwieweit die Wahl der angepassten Funktion bzw. des betrachteten Zeitraums und die Länge des Zeitraums das Trendergebnis beeinflussen. Ebenso werden die

Auswirkungen des unregelmäßigen Samplings der Messdaten auf den resultierenden Trend untersucht. Mit Hilfe einer multiplen linearen Regression wird überprüft, wie stark das Trendergebnis von längerfristigen Schwankungen atmosphärischer Parameter abhängt, die sich möglicherweise in den Zeitreihen der beobachteten Gase widerspiegeln. Hierzu werden Zeitreihen, die den 11-jährigen Sonnenzyklus bzw. die quasi-zweijährige Oszillation (QBO) repräsentieren, in die Anpassungsfunktion miteinbezogen.

Die für HCl und $ClONO_2$ aus den Modell- und Messergebnissen der Gesamtsäulengehalte ermittelten Trends für den Zeitraum 2000–2009 betragen rund -1 bzw. -2%/Jahr, wohingegen HF noch mit etwa 1%/Jahr zunimmt. Teilweise bestehen jedoch deutliche Unterschiede zwischen den gemessenen und simulierten Trends. So zeigen die FTIR-Messungen eine stärkere Abnahme der beiden Chlorspezies auf der Nord- als auf der Südhemisphäre, während analog dazu der HF-Gehalt auf der Südhemisphäre stärker ansteigt. Dies liegt vermutlich an der unterschiedlichen geographischen Verteilung der ODS-Quellen mit Schwerpunkt in den nördlichen mittleren Breiten, die aber von den Modellen offensichtlich nicht berücksichtigt wird. Die $ClONO_2$-Trends aus den Messungen zeigen zusätzlich eine Abhängigkeit von der geographischen Breite, mit stärkeren relativen Abnahmen in höheren und niedrigen als in mittleren Breiten. Dieser Effekt ist jedoch nur in manchen der Modelle wiederzufinden. Trends von HF aus den FTIR-Messungen zwischen 2004 und 2009 zeigen eine Stabilisierung des Gesamtsäulengehalts in den letzten Jahren.

Der zweite Schwerpunkt der Arbeit liegt auf Untersuchungen der unterschiedlich starken Abnahme von HCl und $ClONO_2$. Sowohl in den Messungen als auch den Modellen nimmt der $ClONO_2$-Gesamtsäulengehalt an den meisten der betrachteten Stationen stärker ab als der von HCl. Die Produktion von HCl ist direkt mit der Methan-(CH_4-)Konzentration und die von $ClONO_2$ indirekt mit Distickstoffoxid (N_2O) gekoppelt. Aus diesem Grund werden Sensitivitätsstudien mit dem EMAC-Modell analysiert, bei denen einmal die CH_4- und einmal die N_2O-Konzentration am Boden konstant gehalten wird. Die Ergebnisse dieser Simulationen werden mit denen einer Referenzsimulation verglichen, in der CH_4 und N_2O dem A1B-Szenario aus IPCC (2007) entsprechend zunehmen. Das Ergebnis dieser Studien ist ein deutlicher Hinweis auf einen starken Einfluss des atmosphärischen CH_4-Gehalts auf die Partitionierung zwischen HCl und $ClONO_2$. Je mehr CH_4 zur Verfügung steht, umso stärker wird die HCl- gegenüber der $ClONO_2$-Bildung bevorzugt, was zu einer schwächeren Abnahme des HCl-Gesamtsäulengehalts mit der Zeit führt. Der starke CH_4-Anstieg überkompensiert zudem die Tatsache, dass sich als Folge abnehmender stratosphärischer Temperaturen die Reaktionsgeschwindigkeiten verändern, was eine Verstärkung der $ClONO_2$-Produktion erwarten ließe. Die Stabilisierung des troposphärischen CH_4-Volumenmischungsverhältnisses zwischen 1999 und 2006 zusammen mit seiner Zunahme vorher und nachher eröffnet die außergewöhnliche Möglichkeit, den Einfluss des CH_4-Trends auf die Chlor-Partitionierung in der realen Atmosphäre zu untersuchen. Die Trends der Gesamtsäulengehalte über der Station Kiruna scheinen den aus den Studien mit EMAC erwarteten Zusammenhang zu bestätigen, während er am Jungfraujoch vermutlich vom etwa zeitgleich mit dem Trendwendepunkt in der CH_4-Zeitreihe erreichten Maximum des anorganischen stratosphärischen Chlors überdeckt wird.

Contents

1 Introduction

The focus of this thesis is on the analysis of time series of hydrogen chloride (HCl), chlorine nitrate ($ClONO_2$), and hydrogen fluoride (HF) from measurements and model results. The main reason for the broad scientific interest in atmospheric chlorine species is their involvement in stratospheric ozone depletion. The stratospheric ozone layer essentially protects life on earth from harmful ultra-violet (UV) radiation, thus mankind has a strong interest in preserving it. Crutzen (1970) and Molina and Rowland (1974) were among the first to investigate catalytic cycles of ozone destruction involving nitrogen oxides and chlorine, respectively. In the following years, measurements confirmed an efficiency increase of these catalytic cycles, which was attributed especially to the increasing emission of anthropogenic chlorine source gases (e.g., Chubachi, 1984; Farman et al., 1985; Rosenfield et al., 2005; McLinden and Fioletov, 2011). These species were therefore also called ozone-depleting substances (ODS). Stratospheric ozone depletion due to anthropogenic ODSs manifests itself on the one hand in a global decrease of the ozone content, and on the other hand in the so-called ozone hole occurring in the polar regions in spring (Seinfeld and Pandis, 1998). This ozone hole is characterised by a temporary, very strong decrease in lower stratospheric ozone, especially above Antarctica, resulting mainly from heterogeneous chlorine activation on the surface of polar stratospheric clouds (PSCs).

Since these discoveries, not only stratospheric ozone was monitored very closely, but also total stratospheric inorganic chlorine ($Cl_y = HCl + ClONO_2 + ClO + 2\,Cl_2O_2 + OClO + 2\,Cl_2 + Cl + HOCl + BrCl$) and its anthropogenic organic source gases, mainly chlorofluorocarbons (CFCs), hydrochlorofluorocarbons (HCFCs), carbon tetrachloride (CCl_4), methyl chloride (CH_3Cl), methyl chloroform (CH_3CCl_3), and halons. In order to improve the international cooperation and the global coverage of these observations, the Network for the Detection of Stratospheric Change (NDSC) was founded in the beginning of the 1990s that was later renamed to Network for the Detection of Atmospheric Composition Change (NDACC). Moreover, in 1987, the "Montreal Protocol on Substances That Deplete the Ozone Layer" was signed and subsequently ratified by many countries, who therein agreed on a regulation of ODS emissions. More precisely, the most effective restrictions and a subsequent phase-out were decided upon in amendments and adjustments to this protocol, as can be seen in Figure 1.1. As a result of these international agreements, the tropospheric content of the anthropogenic chlorine source gases reached its maximum in the beginning of the 1990s. The stratospheric inorganic chlorine abundance peaked a few years later, towards the end of the 1990s, due to the time lag resulting from the transport from the troposphere to the stratosphere (WMO, 2003, 2007, 2011). In studies performed in the 1980s and early 1990s, before the Montreal Protocol regulations took effect, an increase of HCl was reported, e.g. by

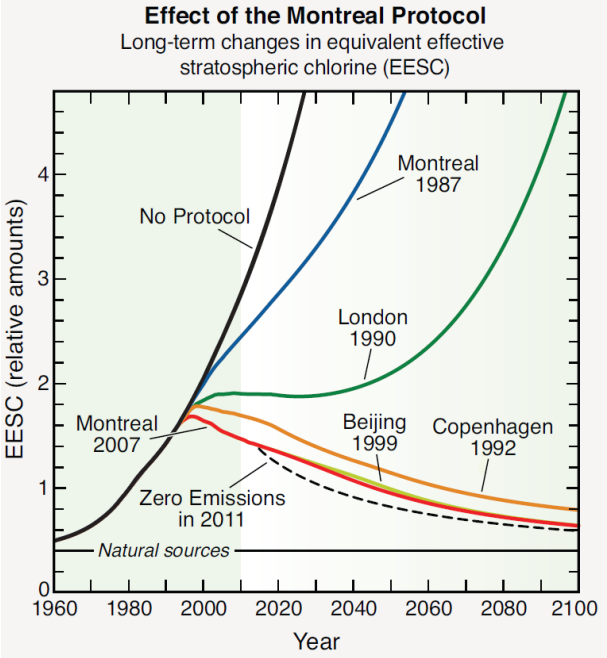

Figure 1.1: Effect of the Montreal Protocol as seen in the long-term changes in equivalent effective stratospheric chlorine (EESC). Projections are shown for different amendments and adjustments to the Protocol. The figure was taken from WMO (2011).

Zander et al. (1987), Rinsland et al. (1991), Wallace and Livingston (1991), and Wallace et al. (1997). A few years later, for example Considine et al. (1999), Newchurch et al. (2003), Rinsland et al. (2003), Froidevaux et al. (2006), and Lary et al. (2007) were able to confirm the expected stabilisation of stratospheric HCl and total Cl_y. Under normal, non-activated conditions, HCl and $ClONO_2$ constitute the major part of stratospheric inorganic chlorine. It is the shorter-lived, highly-reactive ClO_x species (i.e. $Cl + ClO + 2\,Cl_2O_2$) that efficiently decompose ozone. However, from the temporal development of the HCl and $ClONO_2$ abundances, it is possible to infer the evolution of total inorganic chlorine and to draw conclusions on the effectiveness of the Montreal Protocol and its amendments and adjustments. One of the major topics of the present thesis is to determine whether the expected decrease of the atmospheric inorganic chlorine burden since the end of the 1990s can be confirmed with measurements from a global network of ground-based Fourier transform spectrometers.

In addition to chlorine, the inorganic fluorine ($F_y = HF + 2\,COF_2 + COFCl$) content is important to be monitored via the total column abundance of HF, which constitutes about 80% of total F_y in 40 km altitude, for example (Duchatelet, 2011, and references therein). Although fluorine would in principle also be able to destroy ozone in catalytic cycles (analogously to chlorine), it is practically not involved in stratospheric ozone depletion because, after being released from its organic source gases, it rapidly reacts to form HF, which is very stable. This is the reason why fluorine is not explicitly restricted in the Montreal Protocol and its amendments. It is therefore allowed to be contained in substitutes of the

restricted anthropogenic chlorine and bromine source gases, e.g., in hydrofluorocarbons (HFCs), so that the atmospheric fluorine abundance is expected to start decreasing later than the chlorine content. A stabilisation of the HF total column abundance above the Jungfraujoch was found around 2003–2004 by Zander et al. (2008), for example. Due to its chemical stability, HF is often used as a dynamic tracer (e.g., Chipperfield et al., 1997).

Before reliable climate projections can be performed with an atmospheric model, it is essential to verify that the model is able to reproduce the past. This must be done by comparison with measurements. For this reason, the measurements performed and analysed within this work are compared with the results of five different global atmospheric chemistry models. The main purpose thereby is to get an overview on the overall ability of the models to reproduce the measured total column abundances, seasonal cycles, and trends. Only the results for the three above-mentioned species are available, from only one simulation of each model, so that it is impossible to conduct detailed analyses on the reasons for differences between the models or between models and measurements.

Moreover, atmospheric chemistry models may also be used to explain features detected in the measurements, such as the difference in the strengths of the HCl and $ClONO_2$ trends that was described e.g. by Mikuteit (2008), in the SPARC-CCMVal (2010) report or by Kohlhepp et al. (2011) before. A model allows to conduct experiments with atmospheric composition that are not possible in the real atmosphere.

In the framework of this thesis, a global comparison of the temporal evolution of the species HCl, $ClONO_2$, and HF from ground-based measurements and models at 17 sites is performed. Furthermore, the reason for the difference between the trends of HCl and $ClONO_2$ is investigated with the help of a three-dimensional chemistry climate model. Chapter 2 contains meteorological, chemical, and physical basics necessary for the discussion of the results in the later chapters. The function principle of a Fourier transform spectrometer and the data retrieval from its spectra are explained in Chapter 3. The trend determination method is discussed in Chapter 4, along with sensitivity studies of the resulting trend. In the following chapter (5), the comparison of the measurement and model data of the three species is presented, including analyses of the absolute total column abundances, the mean seasonal cycles, and the trends. Moreover, in Chapter 6, sensitivity studies with the EMAC model are discussed that were performed in order to find an explanation for the difference in the strengths of the HCl and $ClONO_2$ trends. A summary is made and final conclusions are drawn in Chapter 7.

2 Meteorological, chemical, and physical basis

This chapter contains some basic information on the atmospheric structure and its tropospheric and stratospheric circulation patterns (Section 2.1). Furthermore, in Section 2.2, important chemical reactions in the stratosphere are discussed, with a focus on ozone depletion and the involvement of the species HCl, $ClONO_2$, and HF, which are investigated in the present thesis. The third part of this chapter (Section 2.3) describes the absorption of radiation by atmospheric trace gases which constitutes the essential physical basis for the solar absorption measurements with FTIR instruments that were performed and analysed within this work.

2.1 Overview on the atmospheric structure and circulation patterns

Solar irradiation is the primary reason and driver for many important properties of earth and its atmosphere. Without energy from the sun, no life on earth would be possible, nor would there be any weather (Petty, 2004). In the following, the resulting vertical temperature structure and global circulation patterns will be explained, after a short description of the composition of the atmosphere.

Composition and vertical structure of the atmosphere

The earth's atmosphere mainly consists of nitrogen (N_2, about 78.08%), molecular oxygen (O_2, about 20.95%), argon (Ar, about 0.93%), water (vapour) (H_2O, very variable), and carbon dioxide (CO_2, about 0.04%) (Kraus, 2004). Besides, many other gaseous, liquid or solid compounds are contained. In this thesis, the main focus is on the three trace species hydrogen chloride (HCl), chlorine nitrate ($ClONO_2$), and hydrogen fluoride (HF). Their peak mixing ratios are in the order of 10^{-9} (i.e., parts per billion, ppb). Despite these small numbers, they have a strong impact especially on the atmospheric ozone (O_3) mixing ratio (see Section 2.2). Ozone in turn has a remarkable influence on the vertical atmospheric temperature profile, according to which the atmosphere can be separated into various layers exhibiting different properties and circulation patterns (Figure 2.1). In the lowermost layer, i.e., the troposphere, temperature decreases with height. This results from the absorption of solar irradiation occurring primarily at the earth's surface, the radiative transfer processes in the air, and the strong vertical mixing in this layer (Kraus, 2004). The troposphere is the layer where the weather as we know it happens, with clouds and precipitation, especially due to its high water content (Kraus, 2004). On average, at about 8 km in polar latitudes and 15 km in the tropics, temperature stabilises. This thin intermediate layer is called the tropopause. Above, the stratosphere begins, reaching up to about 50 km above sea level. This is the layer

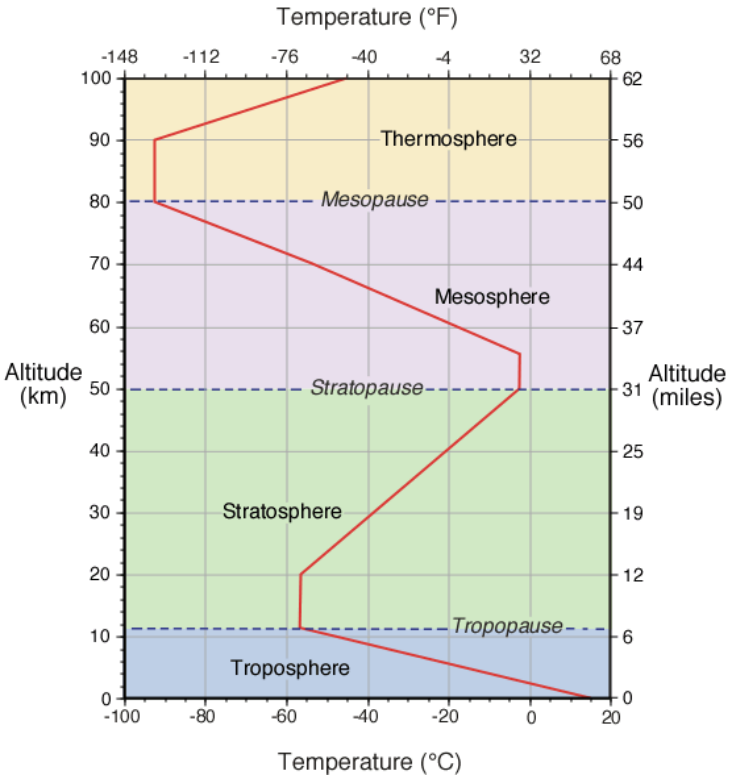

Figure 2.1: Schematic sketch of the average temperature distribution in the different layers of the atmosphere, from the troposphere to the thermosphere (Picture taken with permission from Pidwirny (2006, at http://www.physicalgeography.net/fundamentals/chapter7.html)).

which is most important for the investigations in the present PhD thesis because it is where the primarily investigated species reach their largest volume mixing ratios. In contrast, stratospheric water vapour has a much smaller volume mixing ratio than in the troposphere so that clouds rarely occur, except for example so-called polar stratospheric clouds (PSCs; see Section 2.2). The stratosphere is characterised by a constant temperature in the lower part, and its increase with height above. This results from the absorption of solar ultra-violet (UV) radiation by stratospheric ozone and molecular oxygen (O_2) within the so-called stratospheric ozone layer. The O_3 mixing ratio peaks in about 30–40 km altitude. A photochemical equilibrium is reached between ozone destruction by UV radiation or reaction with atomic oxygen and ozone production by the reaction of molecular oxygen with atomic oxygen that had been produced by photolysis before. In addition, catalytic processes are involved. The most important of these reactions are explained in more detail in Section 2.2. The temperature increases from the lower stratosphere until about 50 km altitude, where it stabilises slightly below 0°C, before starting to decrease with height. This intermediate layer with constant temperature is called the stratopause. In the layer above, the mesosphere, temperature decreases with height until the mesopause at about 85 km altitude. The mesopause is close to the turbopause (at about 90–110 km) which marks an important change in the

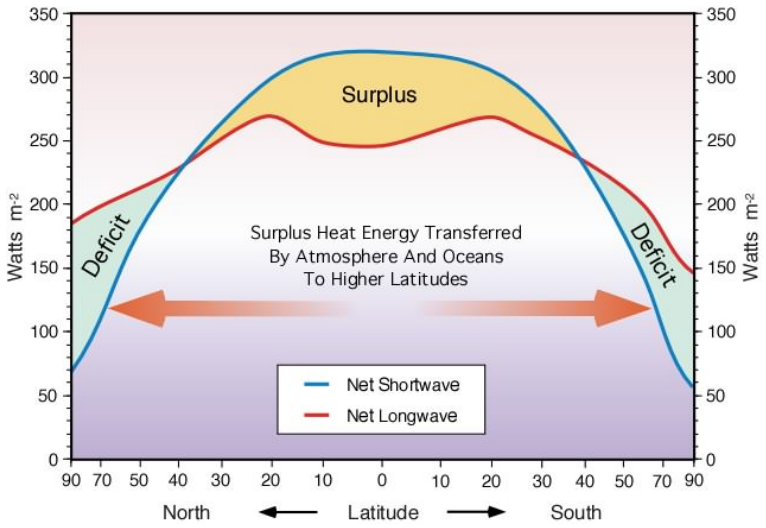

Figure 2.2: Annual average radiation budget at the top of the atmosphere as a function of latitude (Picture taken with permission from Pidwirny (2006, at http://www.physicalgeography.net/fundamentals/chapter7.html)).

overall chemical composition of the atmosphere. Up to here, the volume mixing ratios of the most abundant species are more or less constant, but above, they are unmixed due to gravitational effects (Kraus, 2004). For this reason, the part of the atmosphere below the turbopause is also called homosphere, while the part above then is the heterosphere. The layer between the mesopause in 85 km, and about 800 km altitude is the thermosphere, or ionosphere. The latter name results from the many ions being produced by solar radiation there. The ionosphere is very important for radio signals which are reflected at different layers, depending on their wavelength (Kraus, 2004). In the thermosphere, temperature increases again with height. However, the air density is so low there that temperature could not be measured with the instruments used at the surface. It can only be defined from the mean kinetic energy of the molecules at these altitudes. In the exosphere, above 800 km and until about 60000 km, the non-ionised particles are able to escape to space, while the ionised ones are attracted by the earth's magnetic field and therefore do not leave the atmosphere. This is why the outer part of the exosphere is also called magnetosphere, and the border to space is the magnetopause.

Atmospheric circulation patterns

The sun's energy reaches earth with maximum intensity between 0.2 and 5 μm wavelength, corresponding roughly to the emission of a black body with 6000 K, which is approximately the temperature of the sun's photosphere (Kraus, 2004; Petty, 2004). A radiative equilibrium is reached with the thermal emission of the earth-atmosphere system back to space, otherwise the earth would continuously heat up. An illustration of the annual average radiation budget at the top of the atmosphere as a function of latitude can be found in Figure 2.2 or for example also in Petty (2004, p.4). More solar energy is absorbed at lower

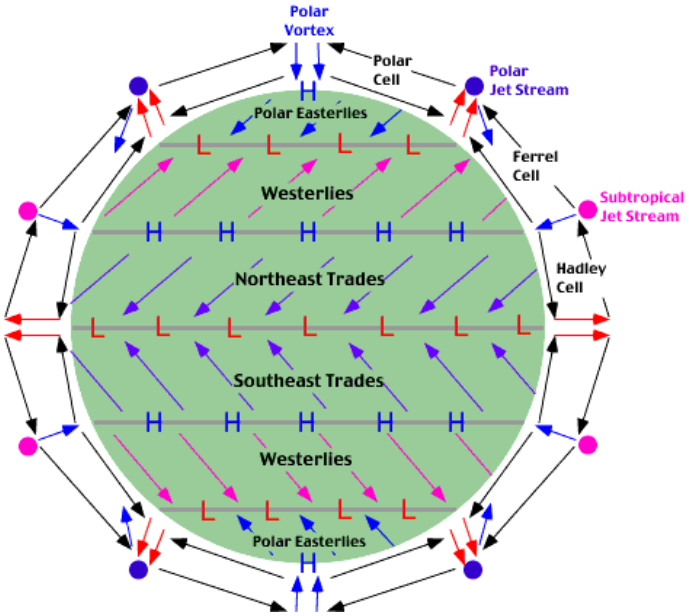

Figure 2.3: Average lower atmospheric global circulation (Picture taken with permission from Pidwirny (2006, at http://www.physicalgeography.net/fundamentals/chapter7.html)).

latitudes than closer to the poles, and only slightly more energy in form of longwave radiation is emitted to space from the tropical than from the polar regions. This leads to an overall negative radiative budget in high and a positive budget in low latitudes. It is obvious that compensation mechanisms are necessary to prevent the tropics from heating up and the poles from cooling down (Petty, 2004). This is the purpose of the global atmospheric and oceanic circulations. However, the energy exchange in the atmosphere is not possible through one direct cell with ascending air over the tropical region and subsidence above the poles because the earth is rotating. This results in a compensating rotation of the air masses aiming at the conservation of angular momentum (Kraus, 2004). This effect can be expressed as an additional force acting on the air parcels which only exists in a rotating coordinate system, the so-called Coriolis force. Also the ocean currents are affected by this force, of course. However, in this thesis, the focus is on the atmosphere. The tropospheric part of the atmospheric general circulation pattern is presented in many textbooks, for example Seinfeld and Pandis (1998, p.12) or Ahrens (1994, p.285), and in Figure 2.3. In a very generalised view, there are three major cells on each hemisphere. Two of them are so-called direct cells, driven mainly by diabatic heating and cooling, the tropical one (also called the Hadley cell), and the polar one. The first one originates primarily from the ascent of air parcels above the equator, or rather the region with the largest energy input and therefore strongest heating of the surface. In this region, the pressure is relatively low in the lower troposphere. It is also called the inter-tropical convergence zone (ITCZ). The air that ascended above the ITCZ moves towards the poles in order to transport energy there, but as already mentioned above, due to the Coriolis force this is not possible directly. Instead, the air descends at only about 30°latitude, creating the subtropical surface high. The second direct one of the three

cells, the polar cell, is driven mostly by air cooling and descending above the poles, creating the polar high. The cell in midlatitudes, between roughly 30 and 60°latitude, is an indirect cell, forced by the other two via mass conservation. It is called the Ferrel cell. The major part of the energy exchange between tropics and poles happens in the midlatitudes. Due to the Coriolis force, this can only be achieved with large-scale waves and eddies, associated with high and low pressure systems. The lower tropospheric mean flow in these regions is westerly, i.e., directed from west to east. Close to the earth's surface, it is more south-westerly due to friction. A low pressure range results on average at very roughly about 60°latitude. The easterly winds in the high latitude regions are necessary for the overall momentum conservation of the earth-atmosphere system. In the Hadley cell, a lower tropospheric transport towards the equator results, basically from mass conservation. These so-called trade winds are also affected by the Coriolis force and are therefore more north-easterly winds in the northern hemisphere and south-easterly winds in the southern hemisphere. However, the overview presented above on the general circulation of the atmosphere is only a schematic explanation of a very complex system that is highly non-linear, i.e., many factors influence each other, and it is often impossible to distinguish between cause and effect (Kraus, 2004).

The global circulation pattern in the middle atmosphere (i.e., the stratosphere and mesosphere) differs from the tropospheric one. A schematic illustration of the stratospheric and mesospheric circulation is given by Dunkerton (1978) which can also be found in Graedel and Crutzen (1994, p.65), for example. The dominant feature in the stratosphere is the so-called Brewer-Dobson circulation. It describes an ascent of air above the tropics and a descent above the poles. This circulation is driven by planetary wave activity which is stronger in winter than in summer, resulting in a stronger Brewer-Dobson circulation in the winter hemisphere (Müller, 2012). Furthermore, the planetary wave activity is in general stronger in the northern hemisphere than it is in the southern hemisphere due to the different distribution of topography and land-sea thermal contrasts (Müller, 2012, and references therein). The Brewer-Dobson circulation leads to an accumulation of O_3 in the extra-tropical lower stratosphere during winter and spring because its lifetime is long enough at these altitudes to be transported towards higher latitudes. From the explanations above, it follows that this build-up is greater in the northern than in the southern hemisphere (Müller, 2012, and references therein). At higher altitudes, the mesospheric circulation transports air from the summer to the winter pole. This circulation is believed to be driven mainly by inertia-gravity waves which propagate upward (Plumb, 2002). They are selectively dissipated in the stratosphere, leading to a mean transport from the pole to the equator in the summer hemisphere, and a mean poleward transport in the winter hemisphere.

The general movement of stratospheric air masses towards the winter pole results in the formation of the so-called stratospheric polar vortex, as the air masses are deflected by the Coriolis force. This leads to relatively strong westerly winds so that to a certain degree the stratospheric air above the winter pole is isolated from the rest of the stratosphere. As a result, the air inside cools down even stronger, thereby enabling the formation of polar stratospheric clouds (please see Section 2.2). The Antarctic polar vortex

is stronger and longer-lived than the Arctic one which is mainly a result of the stronger planetary wave activity in the northern hemisphere that disturbs the vortex.

2.2 Stratospheric ozone chemistry

In this section, some aspects of stratospheric chemistry are presented, with a certain focus on the role of chlorine and fluorine species as some of them are the topic of the present thesis. Seinfeld and Pandis (1998) describe ozone (O_3) as the most important trace constituent of the stratosphere. In Section 2.1, the influence of the stratospheric ozone layer on the temperature distribution in the stratosphere was explained. The photochemical ozone production and destruction processes essentially protect life on earth via the absorption of short-wave solar irradiation which is harmful due to its high energy content. In addition, catalytic reactions are involved in maintaining the natural ozone equilibrium. In the following, the processes involved in the production and destruction of the stratospheric ozone layer shall be explained, with a focus on the role of chlorine.

For about 40 years after its publication, the photochemical mechanism suggested by Chapman (1930) was thought to be able to explain the existence and properties of the ozone layer (Seinfeld and Pandis, 1998). This so-called Chapman cycle starts with the photolysis of molecular oxygen by solar radiation of wavelengths less than 242 nm,

$$\mathrm{O_2} + h\nu \rightarrow \mathrm{O} + \mathrm{O} \qquad [2.1]$$

The produced atomic oxygen quickly reacts with molecular oxygen to form ozone, in the presence of a third molecule M (usually N_2 or O_2):

$$\mathrm{O} + \mathrm{O_2} + \mathrm{M} \rightarrow \mathrm{O_3} + \mathrm{M} \qquad [2.2]$$

This reaction is practically the only one which produces ozone in the atmosphere (Seinfeld and Pandis, 1998). By the following two processes, ozone molecules are destroyed:

$$\mathrm{O_3} + h\nu \rightarrow \mathrm{O_2} + \mathrm{O} \qquad [2.3]$$

$$\mathrm{O_3} + \mathrm{O} \rightarrow \mathrm{O_2} + \mathrm{O_2} \qquad [2.4]$$

For the photolysis reaction [2.3], sunlight with wavelengths shorter than 1140 nm is necessary. However, measurements showed that the ozone concentrations calculated from this Chapman cycle are about a factor of 2 too high (Seinfeld and Pandis, 1998).

The investigation on the reasons for this discrepancy led to the discovery of additional, catalytic cycles that can be summarised as (e.g., Müller, 2012)

$$\mathrm{X} + \mathrm{O_3} \rightarrow \mathrm{XO} + \mathrm{O_2} \qquad [2.5]$$

$$\mathrm{XO} + \mathrm{O} \rightarrow \mathrm{X} + \mathrm{O_2} \qquad [2.6]$$

$$\text{Net: } \mathrm{O_3} + \mathrm{O} \rightarrow \mathrm{O_2} + \mathrm{O_2}$$

where X represents a free radical catalyst, i.e., H, OH, NO, Cl, or Br. The relevance of the catalytic cycles involving NO_x (= NO + NO_2) and ClO_x (= Cl + ClO) and their anthropogenic efficiency increase was discussed by Crutzen (1970) and Molina and Rowland (1974) in the 1970s, respectively. For these investigations on the formation and decomposition of ozone, Paul Crutzen, Mario Molina and Sherwood Rowland were awarded the Nobel prize in chemistry in 1995. For more information on the HO_x and NO_x cycles, please see for example Seinfeld and Pandis (1998) or Crutzen (1970). In the following, only ClO_x will be discussed in more detail due to its relevance for the present thesis.

The major natural source of stratospheric inorganic chlorine is methyl chloride (CH_3Cl), which is emitted mainly by marine algae or tropical biomass burning. In addition, volcanic eruptions may enhance the stratospheric chlorine content (Graedel and Crutzen, 1994). CH_3Cl accounts for about 16% of the total stratospheric chlorine abundance today (Müller, 2012, and references therein). However, in addition to these natural sources, anthropogenic species such as chlorofluorocarbons (CFCs), hydrochlorofluorocarbons (HCFCs), and halons (bromine-containing halocarbons) contribute to the stratospheric chlorine loading. Due to their high stability and non-reactivity in the troposphere, they are able to reach the stratosphere, mostly through the tropical tropopause. In the stratosphere, they are decomposed mainly by photolysis in the 185 to 210 nm spectral window between O_2 and O_3 absorption (Seinfeld and Pandis, 1998). For the two most abundant CFCs, i.e., CFC-11 ($CFCl_3$) and CFC-12 (CF_2Cl_2), the photolysis reactions are

$$CFCl_3 + h\nu \rightarrow CFCl_2 + Cl \qquad [2.7]$$

$$CF_2Cl_2 + h\nu \rightarrow CF_2Cl + Cl \qquad [2.8]$$

The $CFCl_2$ and CF_2Cl radicals rapidly perform other reactions, resulting in the release of the remaining chlorine atoms (Seinfeld and Pandis, 1998). All these additional chlorine atoms released by the above-mentioned anthropogenic species lead to an increase in the efficiency of the catalytic ClO_x ozone-destroying cycles, thereby disturbing the natural equilibrium of the ozone layer. Of course, this is analogously the case for anthropogenic emissions of NO_x or its precursors (mainly N_2O), for example.

After the release of Cl atoms, the ozone-depleting catalytic chlorine cycle can take place:

$$Cl + O_3 \rightarrow ClO + O_2 \qquad [2.9]$$

$$ClO + O \rightarrow Cl + O_2 \qquad [2.10]$$

This ClO_x cycle can be interrupted by conversion of the reactive forms of chlorine (i.e., Cl and ClO) into so-called reservoir forms, i.e., HCl and $ClONO_2$. These reservoir species do not destroy ozone. For the NO_x cycle, such a reservoir species would be nitric acid (HNO_3), for example. HCl and $ClONO_2$ are formed mainly by the reactions

$$Cl + CH_4 \rightarrow HCl + CH_3 \qquad [2.11]$$

$$ClO + NO_2 + M \rightarrow ClONO_2 + M \qquad [2.12]$$

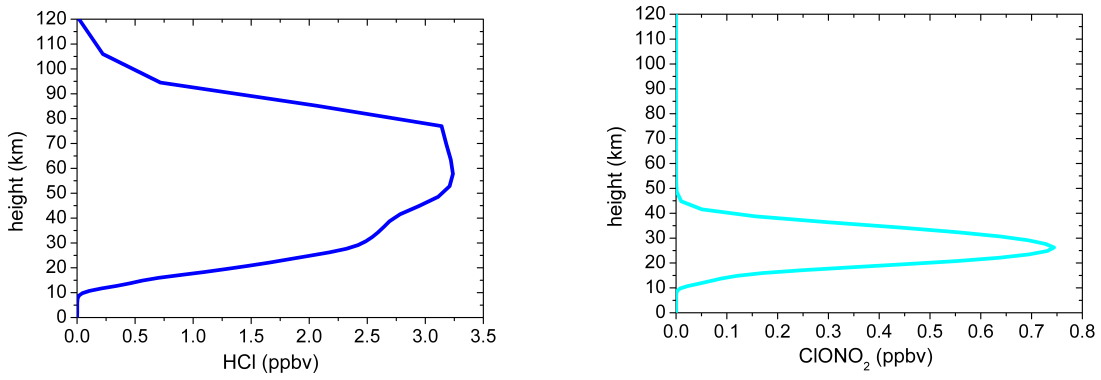

Figure 2.4: Examples for volume mixing ratio profiles of HCl (left) and $ClONO_2$ (right) between ground and 120 km height, above Kiruna. These profiles stem from a long-term model simulation by the Whole Atmosphere Community Climate Model (WACCM) and were provided by J. Hannigan (NCAR). They are used as a priori profiles for the inversion of the FTIR spectra (see Section 3.2).

The production of HCl can ultimately lead to the removal of the chlorine atom from the stratosphere because HCl is relatively stable there and can be transported back to the troposphere, where it is washed out by precipitation (Seinfeld and Pandis, 1998). The storage in the form of $ClONO_2$ is only temporary, it can be photolysed again:

$$ClONO_2 + h\nu \rightarrow ClO + NO_2 \quad [2.13]$$

$$\rightarrow Cl + NO_3 \quad [2.14]$$

Thereby, for wavelengths $\lambda < 308$ nm, the quantum yield is equal to about 0.4 for reaction [2.13] and 0.6 for reaction [2.14], while for $\lambda > 364$ nm, it is 1 for reaction [2.14] (Seinfeld and Pandis, 1998). However, $ClONO_2$ is especially important because it stores two ozone-destroying catalysts, ClO and NO_2 (Seinfeld and Pandis, 1998). Examples for the volume mixing ratio profiles of HCl and $ClONO_2$ are shown in Figure 2.4, for about 67.8°N and 20.4°E, corresponding to the geographical position of the Kiruna site. They represent mean profiles determined from a long-term simulation by the Whole Atmosphere Community Climate Model (WACCM) that were provided by J. Hannigan (NCAR) and are used as a priori profiles for the inversion of the FTIR spectra (see Section 3.2). Especially the $ClONO_2$ mixing ratio depends not only on height, but also on latitude. This results from the photolysis reactions [2.13] and [2.14] which are more efficient in the lower latitudes than closer to the poles because they depend on solar irradiation and thus lead to a relatively lower $ClONO_2$ mixing ratio above the tropical region.

However, species from the catalytic HO_x, NO_x, BrO_x, and ClO_x cycles described by reactions [2.5] and [2.6] can also react with each other, thereby coupling the cycles. For more information, please see for example Seinfeld and Pandis (1998) or von Hobe and Stroh (2012).

Apart from a more or less continuous decrease in stratospheric ozone especially above about 25 km (Graedel and Crutzen, 1994) as a result of the processes described above, another phenomenon can be attributed to the increased emissions of anthropogenic ozone-depleting substances. Since about the early 1980s, very low total column ozone abundances have been measured nearly every spring above the Antarctic region. This feature is commonly referred to as the Antarctic ozone hole. It results from heterogeneous processes on polar stratospheric clouds (PSCs) transforming the chlorine reservoir species into active chlorine, thereby leading to a much larger than usual mixing ratio of the latter. The two most important reactions involved in this so-called heterogeneous chlorine activation are (Müller, 2012)

$$\mathrm{HCl} + \mathrm{ClONO_2} \xrightarrow{het} \mathrm{Cl_2} + \mathrm{HNO_3} \qquad [2.15]$$

$$\mathrm{HCl} + \mathrm{HOCl} \xrightarrow{het} \mathrm{Cl_2} + \mathrm{H_2O} \qquad [2.16]$$

These reactions are quite slow in the gas phase, but substantially faster on the surface of liquid or solid particles. If stratospheric temperatures drop below about 190–195 K, PSCs consisting of NAT (nitric acid trihydrate) particles or STS (supercooled ternary solutions) can form (Seinfeld and Pandis, 1998). Ice particle PSCs exist at slightly lower temperatures only. The chlorine molecules (Cl_2) produced in reactions [2.15] and [2.16] on the surface of these PSCs and released into the gas phase are stable as long as it is dark during polar night, but as soon as enough sunlight is available in spring, they can be photolysed. Reaction [2.15] furthermore produces HNO_3 which remains on the PSC in the following, resulting in a removal of NO_x from the gas phase (Graedel and Crutzen, 1994). Thereby, it hinders chlorine deactivation because as long as HNO_3 is in the gas phase, it can be photolysed so that $ClONO_2$ could be produced (Seinfeld and Pandis, 1998). However, essentially no oxygen atoms are available in the polar winter stratosphere so that instead of the above-described ClO_x cycle, the so-called ClO dimer cycle is the most important process responsible for the ozone hole (Molina and Molina, 1987):

$$\mathrm{ClO} + \mathrm{ClO} + \mathrm{M} \leftrightarrow \mathrm{ClOOCl} + \mathrm{M} \qquad [2.17]$$

$$\mathrm{ClOOCl} + h\nu \rightarrow \mathrm{Cl} + \mathrm{ClOO} \qquad [2.18]$$

$$\mathrm{ClOO} + \mathrm{M} \rightarrow \mathrm{Cl} + \mathrm{O_2} + \mathrm{M} \qquad [2.19]$$

$$2\,[\mathrm{Cl} + \mathrm{O_3} \rightarrow \mathrm{ClO} + \mathrm{O_2}] \qquad [2.9]$$

$$\text{Net: } 2\,\mathrm{O_3} \rightarrow 3\,\mathrm{O_2}$$

Besides, there is one more major process involving ClO and BrO (please see for example Seinfeld and Pandis, 1998; von Hobe and Stroh, 2012).

A temporary ozone depletion in springtime has been measured in the Arctic, too, but due to different dynamical conditions there, it is overall usually much weaker than in the Antarctic. The Arctic stratospheric polar vortex is more variable, warmer, and weaker than the Antarctic one, resulting in a shorter PSC period, for example (please see also Section 2.1 for differences between the Arctic and Antarctic vortex). The polar ozone hole occurs between about 12 and 24 km height (in contrast to the region where

the ClO_x cycle is most effective, between 35 and 45 km), thereby corresponding very well to the altitude range of PSC occurrence (about 10–25 km) (Seinfeld and Pandis, 1998).

This extensive chlorine activation is stopped only by the break-up of the polar vortex and increasing stratospheric temperatures leading to the dissociation of the PSCs. As a result, NO_x becomes available again, and quickly, $ClONO_2$ is produced by reaction [2.12], which has a larger rate coefficient at stratospheric temperatures than reaction [2.11] producing HCl. However, the $ClONO_2$ molecules may be photolysed again (reactions [2.13] and [2.14]) so that the thereby again released chlorine atoms may react with CH_4 to form HCl, which is more stable than $ClONO_2$. This effect of a pronounced peak in the $ClONO_2$ time series followed by a broader, flatter maximum in the HCl abundance can often be observed very nicely in the Arctic. In contrast, in the Antarctic, the recovery of HCl and $ClONO_2$ at the end of the winter usually takes place at about the same time and same strength. One of the reasons for that is the usually stronger so-called denitrification in the Antarctic than in the Arctic stratosphere. This means that due to the long persistence of the PSCs, subsidence of the NAT particles may occur, thereby permanently removing NO_x from the respective heights. In addition, $ClONO_2$ production may be limited by O_3 availability (reaction [2.9]), which is also usually a larger problem in the Antarctic than in the Arctic at the end of the winter due to the stronger Antarctic ozone depletion.

Above, the connection of HCl and $ClONO_2$ with stratospheric ozone depletion was discussed extensively in order to point out the importance of observing the temporal evolution of their atmospheric abundance. The third species which the present thesis focuses on, HF, also contains a halogen atom that would in principle be able to deplete ozone, too. However, fluorine is not involved in stratospheric ozone depletion because the reaction of the freed fluorine atoms with CH_4, forming the reservoir species HF,

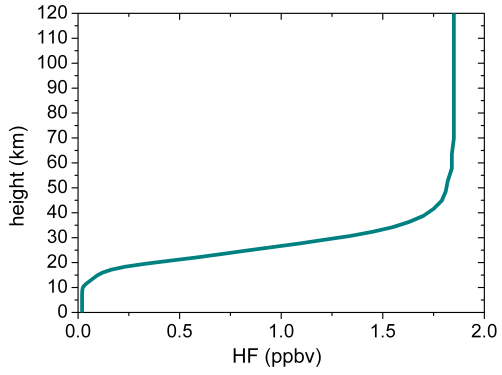

Figure 2.5: Exemplary volume mixing ratio profile of HF between ground and 120 km height, above Kiruna. This profile stems from a nudged model simulation called PEP8 by the KASIMA model (Karlsruhe Simulation Model of the Middle Atmosphere) and is used as a priori profile for the inversion of the FTIR spectra (see Section 3.2).

is very fast. HF in turn is very stable. As a result, only a minor part of fluorine will ever get the opportunity to react with O_3 to FO (von Hobe and Stroh, 2012). Due to its high stability, HF is often used as a dynamic tracer (see e.g., Chipperfield et al., 1997). As the most important source gases of HF are mainly anthropogenic CFCs, HCFCs, and halons, it is also an indicator of the anthropogenic influence on atmospheric composition and chemistry. A profile of HF from a nudged model run with KASIMA (Karlsruhe Simulation Model of the Middle Atmosphere) in the framework of a research contract (PEP virtual institute, Pole-Equator-Pole, run PEP8) is shown in Figure 2.5. It is the one used as a priori for the inversion of the FTIR spectra (see Section 3.2).

2.3 Absorption of radiation by atmospheric trace gases

The determination of total column abundances or profiles of atmospheric trace gases with an FTIR spectrometer is based on the fact that the gas molecules absorb infrared (IR) radiation from the sun (so-called solar absorption measurement) or that they emit IR radiation themselves (atmospheric emission measurement). In solar absorption geometry, which was used for the data analysed in the present thesis, the FTIR instrument basically measures the intensity of the direct solar irradiation reaching the ground (as a function of wavelength). In the following, some basic radiation laws are explained, and finally, a general expression for radiative transfer in the infrared spectral region when considering only absorption is discussed.

The temperature (T) dependency of the radiance B emitted by a black body at a certain wavelength λ is described by Planck's law (e.g., Tipler, 1994; Petty, 2004)

$$B_\lambda(T) = \frac{2hc^2\lambda^{-5}}{\exp(\frac{hc}{\lambda k_B T}) - 1} \qquad [2.20]$$

with

h	$= 6.626 \cdot 10^{-34}$ J s	Planck's constant
c	$= 2.998 \cdot 10^{8}$ m s^{-1}	speed of light
k_B	$= 1.381 \cdot 10^{-23}$ J K^{-1}	Boltzmann's constant

By substitution for $\lambda = c/\nu$ or $\lambda = 1/\bar{\nu}$, the Planck function may be expressed in terms of frequency ν in Hz or $\bar{\nu}$ in cm^{-1}, respectively. The wavelength at which this energy emission per unit time reaches its maximum can be calculated using Wien's displacement law (Tipler, 1994; Petty, 2004)

$$\lambda_{max} = \frac{C}{T} \qquad [2.21]$$

with the constant C amounting to 2898 μm K.

Integration of the Planck curve (Equation 2.20) over solid angle Ω and wavelength λ yields the total radiance emitted by a black body

$$E(T) = \int\int B_\lambda(T)\, d\Omega\, d\lambda \qquad [2.22]$$

If additionally the emissivity ε giving the fraction of energy emitted by a real (grey) body as compared to a black body with the same temperature is considered, the Stefan-Boltzmann law results (e.g., Ahrens, 1994; Tipler, 1994)

$$E(T) = \varepsilon \sigma T^4 \qquad [2.23]$$

with the Stefan-Boltzmann constant $\sigma = 5.6703 \cdot 10^{-8}$ W m^{-2} K^{-4}. According to Kirchhoff's law, the emissivity corresponds to the absorptivity.

The temperature of the sun's photosphere amounts to about 6000 K. Following Wien's displacement law (Equation 2.21), it therefore emits its maximum energy at a wavelength of about 0.48 μm (Petty, 2004). However, although the sun's photosphere can be regarded approximately as a black body, the radiation reaching the earth's surface is weaker than expected from the corresponding Planck curve, resulting from absorption by atmospheric trace gases at certain wavelengths, and from scattering (negligible in the IR spectral region). Examples for this so-called atmospheric transmission spectrum are shown in many textbooks, e.g. in Petty (2004, p.173), Liou (1980, p.39).

A general form of the differential equation of radiative transfer in the atmosphere for the long-wave spectral region is (Paltridge and Platt, 1976)

$$dN_\lambda = -\kappa_{a\lambda} \rho N_\lambda \, ds + \kappa_{a\lambda} \rho B_\lambda(T) \, ds \qquad [2.24]$$

with

N_λ	radiation with wavelength λ
s	distance
$\kappa_{a\lambda}$	mass absorption coefficient
ρ	density

The formal solution to this equation is (Paltridge and Platt, 1976)

$$N_{s,\lambda} = N_{0\lambda} \, \exp[-\tau_{a\lambda}(0,s)] + \int_0^s \kappa_{a\lambda} \rho B_\lambda(T(s')) \, \exp[-\tau_{a\lambda}(s',s)] \, ds' \qquad [2.25]$$

where the optical depth $\tau_{a\lambda}(s',s)$ is defined as the integral over the volume absorption coefficient $\kappa_{a\lambda}\rho$:

$$\tau_{a\lambda}(s',s) = \int_{s'}^{s} \kappa_{a\lambda} \rho \, ds'' \qquad [2.26]$$

When interpreting Equation 2.25 with respect to the atmosphere, we can see that the radiation N_λ at location s is described by the incoming solar radiation $N_{0\lambda}$ which is partly absorbed on its way through the atmosphere (first term), and the emission of all atmospheric layers in between, which is described by the Planck function corresponding to their temperature (second term). This atmospheric infrared radiation is of course also partly absorbed on its way to the location s. As mentioned above, the incoming solar

radiation at the top of the atmosphere ($N_{0\lambda}$) can be expressed by the Planck function of $T_{sun} \approx 6000$ K, $B_\lambda(T_{sun})$.

For this description of radiative transfer, some simplifications have been made. First of all, scattering can be neglected completely in the long-wave spectral region (Brasseur and Solomon, 1986). In addition, local thermodynamic equilibrium was assumed. For practical purposes, the dependency on solar zenith angle which is contained in ds' needs to be expressed explicitly.

The measurements analysed in the present thesis have been performed in solar absorption geometry, as already mentioned above. In this case, also the second term in Equation 2.25 can be neglected because the atmospheric infrared emission is quite weak compared to the intensity of the direct solar beam (Mikuteit, 2008; Kramer, 2007). So the remaining part of the equation describing the radiation intensity measured by solar IR absorption measurements at the ground is

$$N_\lambda = B_\lambda(T_{sun})\ \exp[-\tau_{a\lambda}(0,s)] = B_\lambda(T_{sun})\ \exp\left(-\int_0^s \kappa_{a\lambda}\rho\ ds''\right) \qquad [2.27]$$

The mass absorption coefficient $\kappa_{a\lambda}$ and as a result also the atmospheric optical depth $\tau_{a\lambda}$ is a very complex quantity to determine because it must describe the combined absorption of all atmospheric species at the wavelength of interest. Every species absorbs (and emits) radiation at certain discrete frequencies which are determined by the allowed energy levels of the molecules (von Clarmann, 2003). In the mid-infrared region, it is the transition between different rotational-vibrational states of the molecules that manifests itself in the absorption lines of the spectrum, in contrast to mostly pure rotational transitions in the microwave and sub-microwave spectral regions, and to electron transfer at shorter wavelengths (von Clarmann, 2003). However, it is not trivial to predict the spectral positions and strengths of absorption lines or bands to the required precision because molecules usually are neither rigid rotors nor harmonic oscillators. Therefore, laboratory measurements must be used in connection with theoretical calculations. It can be seen from Equation 2.27 if the exact positions and the strength of the absorption lines are known, the abundance of the molecules present between the observer at the ground and the top of the atmosphere along the line-of-sight can be calculated from the measured transmission spectrum. This retrieval procedure is described in more detail in Section 3.2.

3 FTIR measurements

This chapter intends to give an overview on the function principle and properties of a Fourier transform spectrometer (Section 3.1), and on the following analysis of the measured spectra (Section 3.2). Thereby, a special focus is on the setups and data analysis methods used at the Kiruna and Izaña sites in Northern Sweden and on Tenerife Island, respectively, which are operated by the Institute for Meteorology and Climate Research (IMK-ASF) at the Karlsruhe Institute of Technology (KIT). The spectrum analysis is presented in more detail only for the three species primarily investigated in this work, i.e., hydrogen chloride (HCl), chlorine nitrate ($ClONO_2$), and hydrogen fluoride (HF).

3.1 Spectrum acquisition

This section shortly and generally describes the acquisition of atmospheric spectra with a Fourier transform spectrometer (FTS). The instruments used for the present work all measure in the infrared (IR) spectral region so that in the following, the expression FTIR (Fourier transform infrared) spectrometer is used as an equivalent to FTS, although FTS is the more general expression. In the first part of this section, the basic principles of Fourier spectrometry are presented, i.e., the Michelson interferometer and the Fourier transformation (Section 3.1.1), while the second part (Section 3.1.2) describes properties of a real FTIR spectrometer.

3.1.1 Function principle of a Fourier transform spectrometer

The core of an FTS is its Michelson interferometer. It was initially designed for the exact measurement of absolute wavelengths (Beer, 1992). A Michelson interferometer is based on the principle of amplitude division. A schematic sketch of such an interferometer can be found in many physics textbooks, for example Griffiths and de Haseth (1986), Beer (1992), Tipler (1994), or Meschede (2002). Basically, the incoming light is separated by a beamsplitter into two beams. These are reflected each by a mirror or a retro-reflector and thereby redirected to the beamsplitter again, which then acts as a recombiner. Because the incoming light beam is never perfectly non-divergent, the detector sees interference fringes in the final beam. If the light source is monochromatic, its wavelength can be determined by moving one mirror and counting the number of modulation periods seen by the detector for a certain path difference between the two beams (Beer, 1992).

Figure 3.1 shows the principle setup of an FTS, including the Michelson interferometer. The moving retro-reflector in this system is also called the scanner. It moves at a constant (known) velocity or shortly stops at equally spaced points (Griffiths and de Haseth, 1986). The detector then records the intensity of

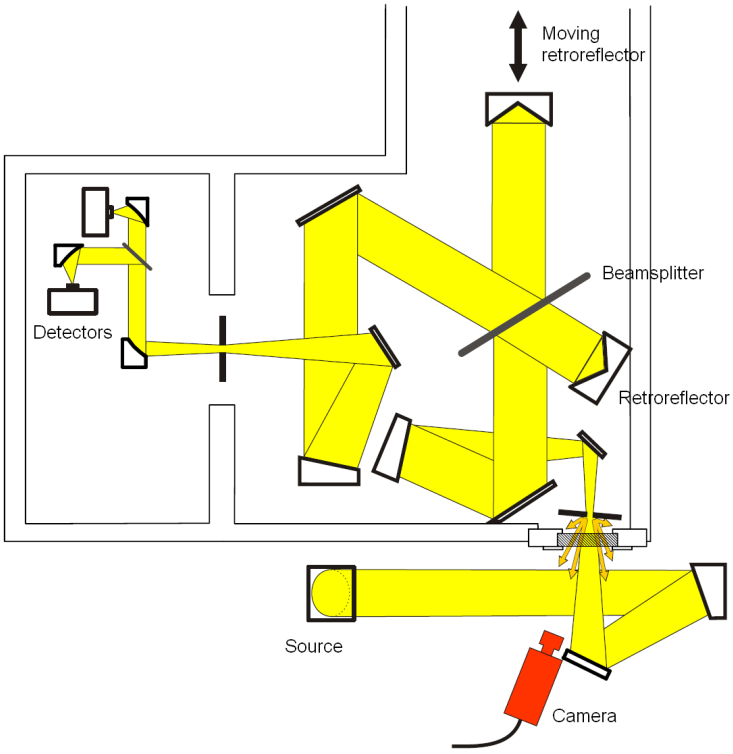

Figure 3.1: Principle setup of an FTIR spectrometer. Picture taken with permission from Gisi et al. (2011).

the recombined beam as a function of optical path difference. Thereby, the very high optical frequency $\bar{\nu} = 1/\lambda$ (in cm^{-1}) of the incoming light is converted down to an electrical frequency f in Hz that is measurable by a detector (Griffiths and de Haseth, 1986; Beer, 1992):

$$f = 2\bar{\nu}V \qquad [3.1]$$

with the velocity of the scanner V. It is very important to note that this frequency transformation is linear.

For a monochromatic source with incoming intensity $2F$, the intensity I reaching the detector for a certain path difference x between the two beams can be expressed as (Beer, 1992)

$$I(x) = F[1 + \cos(2\pi\bar{\nu}x)] \qquad [3.2]$$

However, the source we want to analyse (i.e., the sun) is not monochromatic, so we have to integrate over all wavelengths in order to describe the detected signal correctly (Beer, 1992)

$$I(x) = \int_0^\infty F(\bar{\nu})[1 + \cos(2\pi\bar{\nu}x)]d\bar{\nu} \qquad [3.3]$$

$$= \int_0^\infty F(\bar{\nu})d\bar{\nu} + \int_0^\infty F(\bar{\nu})\cos(2\pi\bar{\nu}x)d\bar{\nu} = I_{DC}(x) + I_{AC}(x) \qquad [3.4]$$

So $F(\bar{\nu})$ obviously describes the spectrum we are interested in. The first term in Equation 3.4, called $I_{DC}(x)$ here, is a constant, while the second one, $I_{AC}(x)$, is the part of the recorded intensity that is usually referred to as the interferogram (Griffiths and de Haseth, 1986). It will be discussed in the following. Because a physical frequency $\bar{\nu}$ must be larger than or equal to 0, we can change the lower limit of the integral to $-\infty$ without changing its value. Now it is obvious that the interferogram $I_{AC}(x)$ corresponds to the cosine Fourier transform of the incoming spectrum $F(\bar{\nu})$. This means the following is also true:

$$F(\bar{\nu}) = \int_{-\infty}^{\infty} I_{AC}(x)\cos(2\pi\bar{\nu}x)dx \qquad [3.5]$$

Obviously, this Fourier transformation which is necessary to determine the spectrum from the interferogram is responsible for the name of the measurement principle.

As described above, the Michelson interferometer is used to determine the wavelength(s) of the incoming radiation. On the other hand, if the wavelength of a monochromatic source is known very well, such a source can be used to determine the exact position of the moving retro-reflector as a function of time. To know this is of course essential for the frequency transformation (Equation 3.1), and therefore, a monochromatic laser beam (at Kiruna it is a HeNe laser with $\lambda = 632.8$ nm) is coupled into the spectrometer. From the interference in the recombined beam and its change with time, the velocity and precise position of the scanner can be calculated. The laser interferogram is recorded by separate detectors.

In the present work, ground-based solar absorption measurements with an FTIR spectrometer are presented. So the quantity of interest is the intensity of solar irradiation at the ground (as a function of wavelength) or rather its weakening due to absorption by different atmospheric species. That means the direct solar beam is used as the radiation source. In order to accomplish that, a so-called sun tracker is necessary with mirrors that move according to the calculated position of the sun. However, the position at which the sun is seen also depends on the actual refractive index (and thereby pressure) so that it can differ from the calculated one. In order to adapt the sun tracker to this, a camera is used to correct the position of the tracking mirrors so that always the radiation from the centre of the solar disc is directed into the spectrometer (see also Figure 3.1). This is a new and improved concept introduced by Gisi et al. (2011) and used at the Kiruna site since September 2010. Before, a quadrant diode regulated the mirror position, as is still done at many other ground-based FTIR sites.

3.1.2 Properties and error sources of a real FTIR spectrometer

In the previous section, it was explained that a Fourier transformation is needed to convert the detected intensity as a function of path difference into the desired spectrum of the radiation source. However, a real FTS of course cannot determine $I(x)$ continuously, only for a limited number of discrete x values with equal distance δx, because the sampling frequency is limited. In order to know this δx very precisely, it is essential to determine the exact velocity and position of the moving mirror or retro-reflector (the scanner). This can be achieved with an additional monochromatic laser beam coupled into the system, as described in Section 3.1.1. Because the interferogram is not infinitely long, the spectrum can only be

determined for discrete and equally-spaced values of the frequency in cm^{-1}, $\delta\bar{\nu}$. In complex notation, the discretised Fourier transformation pair can be written as (Beer, 1992)

$$I_{AC}(m\delta x) = \sum_{k=0}^{N} F(k\delta\bar{\nu}) \exp(2\pi ik\delta\bar{\nu}m\delta x) \quad [3.6]$$

$$F(n\delta\bar{\nu}) = \frac{1}{N} \sum_{j=0}^{N} I_{AC}(j\delta x) \exp(-2\pi in\delta\bar{\nu}j\delta x) \quad [3.7]$$

Due to the discrete sampling of the interferogram, the spectrum must not contain frequencies larger than the so-called Nyquist frequency which is defined as

$$\bar{\nu}_{ny} = \frac{1}{2\delta x} \quad [3.8]$$

So obviously, the smaller the spacing δx of the interferogram, the larger is the detectable spectral interval. Frequencies beyond $\bar{\nu}_{ny}$ are folded back onto other frequencies in the resulting spectrum. To avoid this unwanted effect called aliasing, optical and electronic filters are needed in the system (Beer, 1992).

As mentioned above, the finite spectral resolution of an FTS basically results from the finite maximum optical path difference (L). The measured interferogram $I_{AC}(x)$ can be regarded as part of an infinite interferogram $I_{\infty}(x)$ that was multiplied by a boxcar function $B(x)$ which is equal to 1 between $x = 0$ and L, and 0 everywhere else. For the Fourier transform $F(\bar{\nu})$ of the interferogram, this multiplication of $I_{\infty}(x)$ and $B(x)$ corresponds to a convolution of their Fourier transforms. The Fourier transform $J(\bar{\nu})$ of $B(x)$ is a sinc function (Beer, 1992):

$$J(\bar{\nu}) = \frac{\sin(2\pi\bar{\nu}L)}{2\pi\bar{\nu}L} = sinc(2\pi\bar{\nu}L) \quad [3.9]$$

The effect of this sinc function is to smear out the fine structure in the spectrum. The spectral resolution of the FTS is therefore often defined as the full width at half maximum (FWHM) of the sinc function, corresponding to about $0.6034/L$ (Beer, 1992). So obviously, the resolution is inversely proportional to the maximum optical path difference of the spectrometer. The sinc function in Equation 3.9 is also called the instrumental line shape (ILS). As a result of misalignment of the spectrometer, phase-shifts, or a strong modulation of the signal (see below), for example, the real ILS may be asymmetric or exhibit a reduced amplitude compared to the ideal ILS. This must be considered in the analysis of the spectrum. Therefore, the ILS must be regularly monitored. Within the Network for the Detection of Atmospheric Composition Change (NDACC), from which data were used in the present thesis, this is done by analysing measurements with similar gas cells filled with HBr, for example with the software LINEFIT (Hase et al., 1999). In order to dampen the side oscillations of the ILS and thereby their influence on the spectrum, a so-called numerical apodisation can be applied. This means the interferogram is multiplied with a triangular or trigonometric function (Mikuteit, 2008), corresponding to a convolution of the Fourier transforms, as already mentioned above. Thereby, the side lobes of the ILS can be

suppressed. Such an apodisation always leads to a widening of the ILS and thereby to a reduction of the spectral resolution (Beer, 1992). No apodisation is necessary for the high-resolution spectra used in this work because the atmospheric lines are wider or of about the same width as the resolution of the spectrometer so that the side lobes of the ILS are smeared out.

One of the most important parts of the spectrometer is the beamsplitter. The measured spectrum is very sensitive to its properties. It consists of a substrate with the beam splitting layer on top, where the substrate of course must not be absorbing in the wavelength region to be detected. For the mid-infrared (MIR) spectral region, potassium bromide (KBr) may be used as substrate, while for obtaining near-infrared (NIR) spectra, calcium fluoride (CaF_2) is useful. An ideal beamsplitter separates the incoming beam into two beams of equal intensity and does not absorb any of the radiation to be measured.

By optical dispersion, a wavelength-dependent phase shift can be introduced in the resulting spectrum. It can already be seen in the interferogram which is not symmetric around ZPD (zero path difference) in this case. The phase shift generally results from a difference in optical thickness between the two beams. Due to the dependency of the refractive index on wavelength, also the induced phase shift varies with wavelength (Beer, 1992). Phase dispersion may also result from frequency-dependent electrical phase shifts occurring in the detector signal chain (Beer, 1992).

In addition to the phase shift, the modulation efficiency which describes the fraction of the incoming radiation that reaches the detector is another measure for the quality of the spectrometer system (Hase et al., 1999; Hase, 2000). A reduction in modulation efficiency also results from optical dispersion, or from absorption by the beamsplitter material.

Optical interference between the surfaces of transmissive elements results in a sinusoidal modulation of the spectral continuum (Beer, 1992). In order to minimise this effect called channeling, wedged optical elements are used.

The instrument itself emits infrared radiation according to its temperature, following Planck's law (see Section 2.3). It is obvious that this self-emission background might be a problem for spectroscopic work in the infrared spectral region. However, in the case of solar absorption measurements, the radiation emitted by the spectrometer is negligible compared to the incoming solar intensity (Hase, 2000; Mikuteit, 2008).

In order to measure a spectrum in the infrared region, a cooled detector is advantageous (Griffiths and de Haseth, 1986; Beer, 1992). For the MIR spectral region, an MCT (mercury-cadmium-telluride, HgCdTe) detector is used to cover the long wavelength range (about 500 to 1380 cm^{-1}) and an InSb (indium-antimonide) detector for the shorter wavelengths (about 1800 to 4300 cm^{-1}) at the sites Kiruna and Izaña. They are cooled down by liquid nitrogen to about -196°C (77 K). The MCT detector exhibits a nonlinear behaviour with respect to its response to different wavelengths, leading to a wavelength-dependent baseline of the spectrum. This effect must be corrected for, which is done by using saturated lines to manually determine the respective wavelength-dependent offset in each spectrum, and then subtracting it. The signal-to-noise ratio can be improved by using optical bandpass filters. Similar sets of

filters are used at all 17 NDACC sites taking part in the comparison study of FTIR and model time series presented in Chapter 5.

For the analyses reported in this thesis, measurements of different FTIR instruments were used. They were basically built by two companies, Bruker and Bomem. The Bruker 120HR and 125HR instruments only differ with respect to data acquisition electronics, leading to a higher and thus better signal-to-noise ratio in the 125HR spectrometer (see, e.g., Kohlhepp et al., 2012). The Bruker 120M instrument is the mobile and therefore smaller version which is more difficult to align and less stable than the other two Bruker instruments mentioned above. This may lead to a slightly worse performance of the 120M. However, this would affect mostly the retrieved profiles and not the total column abundances used in the present work. So overall, the results from the different Bruker instruments are expected to agree very well. A comparison between total column abundances retrieved from spectra of a Bruker 125HR and a Bomem DA8 was conducted for example by Batchelor et al. (2010) at the Eureka site (in Canada; please see Section 5.1.1). It revealed a maximum difference of 3.5% between the two instruments for the three species investigated in the present work, i.e., HCl, $ClONO_2$, and HF. A table listing which site uses which instrument can be found in the appendix to this thesis.

3.2 Retrieval of the gases

From the solar absorption spectra obtained with an FTIR instrument as described in Section 3.1, total column abundances or even vertical profiles of various atmospheric species can be determined as long as the atmospheric absorption properties in the analysed wavelength interval are known. The very basic physical principles were discussed in Section 2.3. For most of the absorption lines and their properties necessary for the present work, the information from the HITRAN (high-resolution transmission) spectral database was used which is updated every few years (e.g., Rothman et al., 1992, 1998, 2003, 2005).

For the determination of the species abundances from the measured solar spectra, a radiative transfer model in connection with an iterative retrieval procedure is applied. Thereby, a-priori profiles of the species and measured (or modelled) temperature and pressure profiles are used to calculate a first-guess spectrum (forward calculation). The calculated spectrum is then compared with the measured one. According to the differences between the measured and simulated spectrum, the respective gas concentrations from the a-priori profiles are changed, and a new spectrum is calculated. In the end, this iterative inversion procedure results in a best guess for the profile of the species. However, it is not straightforward to obtain information on the profile shape from the spectrum as it requires interpreting the pressure broadening of the individual lines. For some gases, for example chlorine nitrate, this is nearly impossible due to the weakness and complexity of its absorption features. Not all retrieval codes used for the interpretation of FTIR spectra are able to extract this profile information anyway. For the FTIR measurements at the 17 NDACC sites described and discussed mainly in Chapter 5, the codes applied are SFIT1 and SFIT2 (e.g., Rinsland et al., 1998), GFIT (e.g., Washenfelder et al., 2006), and PROFFIT (Hase, 2000). Amongst them, only SFIT2 and PROFFIT perform a profile fit, while SFIT1 and GFIT only scale the a-priori profiles. Intercomparisons between SFIT2 and PROFFIT were reported by Hase et al. (2004) and Duchatelet et al. (2010). In the analyses performed in the present thesis, however, no profiles of the species are used at all, only the total column abundances. The retrieval of the species abundances is usually only performed in small spectral intervals, the so-called microwindows. The major advantage of this is that only a few other interfering species have to be considered, which results in fewer possible error sources.

Because the present thesis was produced at the Institute for Meteorology and Climate Research (IMK-ASF) at the Karlsruhe Institute of Technology which runs two of the 17 sites taking part in the comparison study described in Chapter 5 (i.e., Kiruna and Izaña), the retrieval method for these sites and the species hydrogen chloride (HCl), chlorine nitrate ($ClONO_2$), and hydrogen fluoride (HF) is described in more detail. For more information on the measurements and retrieval parameters at the other sites, please refer to Tables A.1 to A.2 in the appendix of this thesis or to Kohlhepp et al. (2012, and references therein). The retrieval code used at Kiruna and Izaña for the mid-infrared measurements is PROFFIT (for PROFile FIT) which includes the radiative transfer algorithm PROFFWD. The temperature and pressure profiles PROFFIT needs for the inversion of the spectra are taken from the National Center for Environmental

Prediction (NCEP) (Lait et al., 2005). The standard procedure followed with PROFFIT is to first retrieve the main absorbers H_2O, N_2O, CH_4, O_3, and HNO_3 from the spectra. If some of these act as interfering species in microwindows used for the retrieval of less strongly absorbing species, the information on their actual concentration is used for these retrievals, making the fitting procedure quicker and more reliable.

Errors induced in the interferograms and spectra by instrumental properties or problems discussed in Section 3.1.2 may of course affect the results for the retrieved species. In addition, uncertainties are introduced for example by the used spectral line parameters and the temperature and pressure profiles. Another error source is for example the solar zenith angle which needs to be known very accurately in order to correctly determine the air mass passed by the solar beam on its way through the atmosphere (Hase, 2000; Gisi et al., 2011). This implies exact knowledge of the measurement time. More detailed and quantitative discussions of the error sources in FTIR measurements are given especially in Hase (2000), and specifically for the species dealt with in the present thesis also in Mikuteit (2008).

Figure 3.2 shows the height dependency of the sensitivity of the retrieval for the three species at Kiruna, describing the change in the total column abundance resulting from a partial column change. It can be seen from this figure that the sensitivity of the FTIR instrument for all species is not very strong in the troposphere, while it is nearly ideal (equal to 1) in the stratosphere where the volume mixing ratios peak (please see Section 2.2 for exemplary profiles of HCl, $ClONO_2$, and HF).

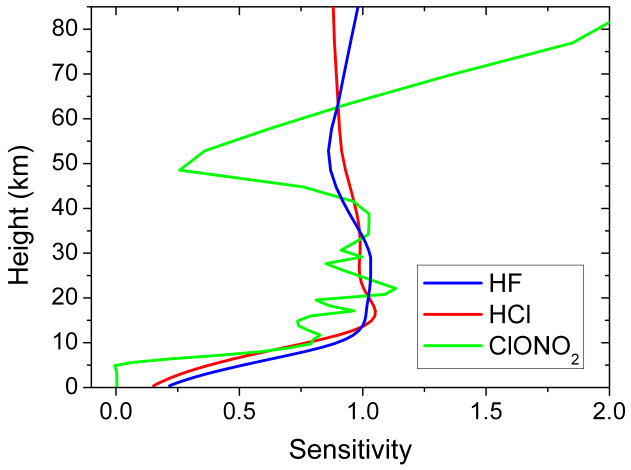

Figure 3.2: Height dependency of the sensitivity of the retrieval as defined by Vigouroux et al. (2008) for HF (blue line), HCl (red line), and $ClONO_2$ (green line). This total column sensitivity describes the change in the retrieved total column, Δcol_{retr}, which results from a partial column change $\Delta col_{inp}(h)$ applied at altitude h. The resulting sensitivity is given by $sens(h) = \Delta col_{retr}/\Delta col_{inp}(h)$. The curves shown represent mean values each calculated from six arbitrary spectra with different solar elevation angles ranging from about 2 to 38°. The figure was taken from Kohlhepp et al. (2011).

In the following, a short overview is given on the microwindows used for the retrieval of HCl, $ClONO_2$, and HF, and their properties and errors, at Izaña and Kiruna, with a focus on the latter site.

3.2.1 Hydrogen chloride (HCl)

For the retrieval of the HCl time series at Kiruna and Izaña presented in this thesis, the following 12 microwindows were used:

2727.73–2727.82 cm^{-1}, 2775.73–2775.79 cm^{-1}, 2819.52–2819.61 cm^{-1},
2821.52–2821.62 cm^{-1}, 2843.60–2843.65 cm^{-1}, 2904.09–2904.14 cm^{-1},
2923.65–2923.78 cm^{-1}, 2925.80–2926.00 cm^{-1}, 2942.70–2942.75 cm^{-1},
2961.04–2961.09 cm^{-1}, 2963.25–2963.32 cm^{-1}, 2995.76–2995.79 cm^{-1}

Compared to the use of less microwindows, the vertical resolution is thereby improved (Mikuteit, 2008). The main other absorbers in these microwindows that therefore need to be considered in the retrieval are H_2O, O_3, and CH_4. In addition, also N_2O, NO_2, and OCS are included. The two HCl isotopologues $H^{35}Cl$ and $H^{37}Cl$ are retrieved separately, by applying a so-called inter-species constraint. Their relative atmospheric abundances are approximately 76 and 24%, respectively (Meier et al., 2004). Figure 3.3 shows the atmospheric transmission in the spectral region around the most important HCl microwindow and the signatures of HCl and the interfering species CH_4 in this case, as calculated by PROFFWD for 23 March 2003.

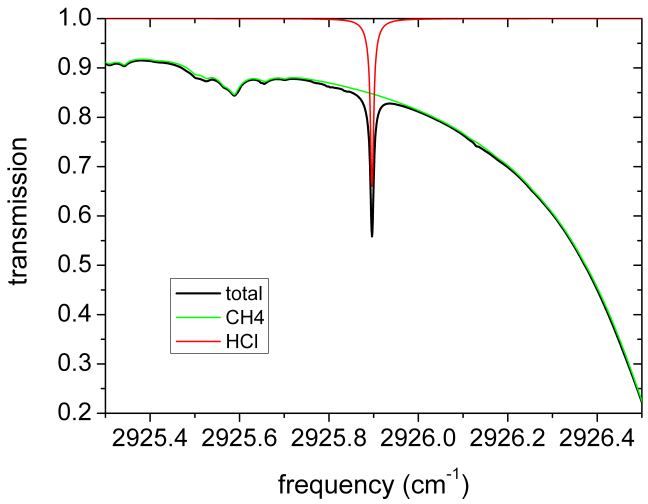

Figure 3.3: Atmospheric transmission around one of the HCl microwindows which contains a signature of CH_4 as interfering species, calculated by PROFFWD for 23 March 2003.

The overall statistical measurement uncertainty for HCl in the FTIR measurements at Kiruna (calculated after Rodgers, 2000) amounts to about 1.2% (Kohlhepp et al., 2011).

3.2.2 Chlorine nitrate ($ClONO_2$)

$ClONO_2$ is not easy to measure with an FTIR spectrometer due to its weak absorption lines. The retrieval is even more difficult at lower latitudes (e.g., at Izaña), where the total column abundances are relatively small, than at higher latitudes (e.g., at Kiruna), where they are slightly larger. The microwindows used at Kiruna and Izaña for the presented results are:

779.000–779.800 cm^{-1}, 780.000–780.300 cm^{-1}, 780.300–781.300 cm^{-1}

The interfering species that need to be considered in this case are H_2O, CO_2, O_3, HNO_3, and C_2H_2. The targeted $ClONO_2$ absorption line is at about $\bar{\nu} = 780.22$ cm^{-1}, i.e., in the middle one of the three microwindows. The first and the last microwindow are included in the retrieval in order to improve the results for the interfering species. The atmospheric transmission in the spectral region around the targeted $ClONO_2$ line is shown in Figure 3.4, calculated by PROFFWD for 23 March 2003.

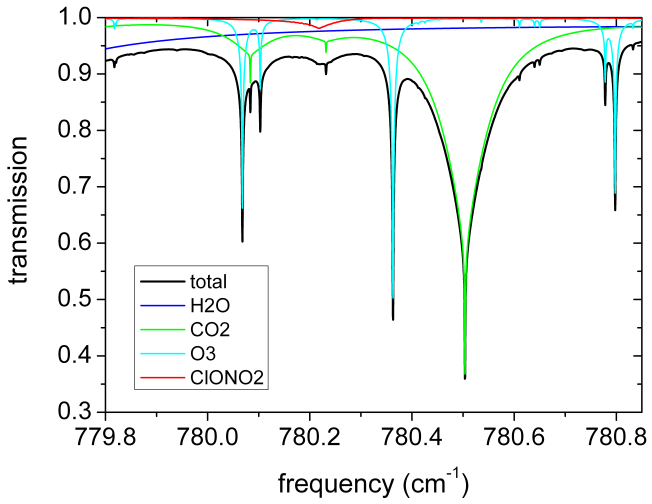

Figure 3.4: Atmospheric transmission in the spectral region around the main $ClONO_2$ microwindow which contains signatures of H_2O, CO_2, and O_3 as interfering species, calculated by PROFFWD for 23 March 2003.

At some of the other sites taking part in the study reported in Chapter 5, the method of Reisinger et al. (1995) is applied for the $ClONO_2$ retrieval, which is qualitatively similar to the approach for Kiruna and Izaña described above. Reisinger et al. (1995) suggested to at first fit the strongest absorbers in a

relatively large microwindow around the $ClONO_2$ absorption line and then retrieve $ClONO_2$ in a more narrow window by considering the just obtained information concerning the actual abundances of the interfering species (see also Mikuteit, 2008).

An average estimate of the error (calculated after Rodgers, 2000) for the measurements of $ClONO_2$ total column abundances at Kiruna is 29% (Kohlhepp et al., 2011), with a smaller value in winter and spring, when the total column abundance is larger, and a larger one in summer, when strong photolysis leads to a low total column abundance of $ClONO_2$.

3.2.3 Hydrogen fluoride (HF)

The microwindows used for the retrieval of HF at Kiruna and Izaña are:

$$4000.900\text{–}4001.050\ \mathrm{cm}^{-1}, \quad 4038.850\text{–}4039.080\ \mathrm{cm}^{-1}$$

As interfering species, H_2O, O_3, and CH_4 need to be considered in the analysis with PROFFIT. As an example, the atmospheric transmission in the spectral region around the second microwindow is shown in Figure 3.5, as calculated by PROFFWD for 23 March 2003. The statistical measurement error calculated after Rodgers (2000) for HF at Kiruna amounts to approximately 1.5% (Kohlhepp et al., 2011).

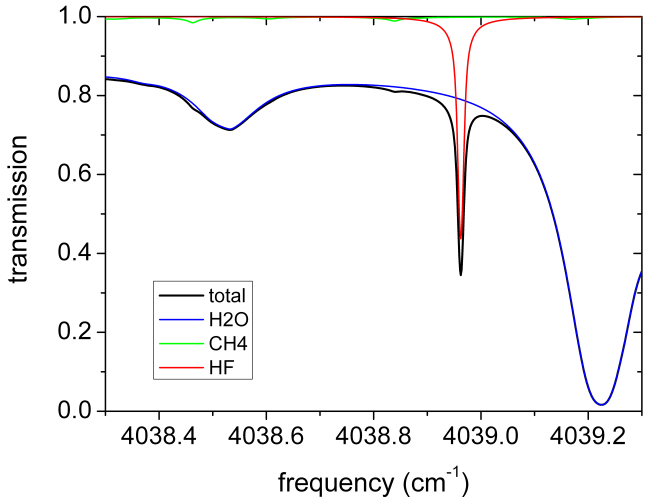

Figure 3.5: Atmospheric transmission in the spectral region around one of the HF microwindows which contains signatures of H_2O and CH_4 as interfering species, calculated by PROFFWD for 23 March 2003.

4 Trend analysis method and sensitivity studies

A major part of the work presented in this PhD thesis consists in the determination of trends from time series of atmospheric species originating either from measurements or from model calculations. In this context, the term "trend determination" means that a function is fitted to the data which consists at least of a linear part. In addition, it may contain periodic terms (see below). The trend found in the time series is then basically represented by the slope of the linear part. Of course, this implies the assumption that the investigated quantity exhibits an approximately linear behaviour during the considered time period.

The total column abundances of the three atmospheric species primarily investigated here exhibit a non-negligible seasonal cycle, with increasing amplitude towards the poles. A Fourier series was therefore included in the fitting function in order to account for this seasonal variation. In an analysis of time series of total and partial column abundances of atmospheric gases, Gardiner et al. (2008) found that a third-order Fourier series marks the best balance between representing the time series and avoiding to over-fit the data. The function that was fitted to the data using a least squares method thus reads

$$f(t) = p_1 (1 + p_2 t) \left\{ 1 + \sum_{i=1}^{3} [q_i \cos(2i\pi t) + r_i \sin(2i\pi t)] \right\} \qquad [4.1]$$

where t is the time in years relative to 1st January 2000. The fitting parameters in the linear part of the function are called p_1 and p_2, where the latter corresponds to the trend. The parameters scaling the Fourier terms are q_i and r_i, with $i = 1, ..., 3$ in this case. However, for some of the measurement time series analysed in Sections 4.2.1 and 5.3, only a first-order Fourier series was used because the third-order results are not reliable. Specifically, this concerns time series with large regular gaps due to polar night or because the data are based on campaign instead of continuous measurements. Including a third-order Fourier series in the fitting function of those time series may lead to large unphysical oscillations so that the trend result cannot be trusted then either. A first-order series is not able to represent the seasonal cycle as well as a third-order series, for example if the minimum is broader than the maximum, and/or both are not exactly half a year apart, or something similar. This results in larger root mean square differences between data and fit in the first-order case, and finally in a larger uncertainty for the trend. The trend results in this work are reported as percentage of the value of the linear fit on 1st January 2000.

In Section 4.1, a description of the error estimation method is given, followed by an extensive discussion on factors influencing the trend results obtained in this work (Section 4.2).

4.1 Error estimation with a bootstrap resampling method

The approach employed in this work to determine the confidence intervals for the obtained trend results is a so-called bootstrap method. According to Efron and Tibshirani (1991), this name refers to the use of the original data set (the one being analysed) to generate new data sets. These numerical statistical methods were first introduced by Efron (1979), at a time when increasing computer power enabled the design of alternatives to classical statistical methods.

In general, a typical application of the bootstrap method can be described as follows (Efron, 2003): A data set representing a sample of an underlying unknown probability model is given. We are interested in some statistic of the unknown probability model and try to estimate it from the data set we have. But of course this estimate has an uncertainty, which can be assessed with the bootstrap method. This requires the (parametric) model (if any) applied to the data set to be correct (Davison and Kuonen, 2002). In addition, it is usually assumed that the residuals are independent and identically distributed (i.i.d.) (e.g., Efron and Tibshirani, 1986; Gatz and Smith, 1995). If this assumption is not valid, modifications of the bootstrap method can be used, for example the block bootstrap or the sieve bootstrap (e.g., Bühlmann, 2002; Goncalves and White, 2005). In general, an important reason why the bootstrap method is widely used is because it does not need any assumption on the underlying distribution to be made, which is often not known. For more detailed descriptions of the bootstrap method and its different types please see for example also Efron (1979), Efron and Tibshirani (1986), Efron and Tibshirani (1991), Davison and Hinkley (1997), Davison and Kuonen (2002), or Efron (2003).

The bootstrap resampling scheme applied in the present work was for example described by Davison and Kuonen (2002) who called it “resampling residuals”. E.g., Gardiner et al. (2008) applied it to time series of total and partial column abundances of atmospheric gases, very similar to the analyses presented here. The algorithm starts by determining the residuals of the least squares fit of function (4.1) to the data. A so-called bootstrap sample that has the same size as the original data set is drawn randomly (with replacement) from these residuals and added to the fit function values. To this new artificial time series, the same function as before is fitted. These procedures of resampling the residuals between the “real” data and the initial fit, creating a new data set, and fitting function (4.1) to it, are repeated many times, at least about 1000 times (Efron and Tibshirani, 1986). In the present work, the number of these bootstrap loops was actually 5000, thereby following Gardiner et al. (2008). So the algorithm produces 5001 different sets of the fitting parameters in function (4.1) which are used then to evaluate the uncertainty of the parameters of the initial fit, one of which is the trend estimate. This can for example be done by calculating the standard deviation. In this work, the 97.5 and 2.5 percentiles of the 5001 trend values are determined in order to estimate the 95% confidence interval. From this interval, a mean deviation is calculated.

Apart from Gardiner et al. (2008) who validated this particular bootstrap method for measurements of atmospheric species by FTIR spectrometers, it was also already used for such data by e.g. Mikuteit (2008), Vigouroux et al. (2008), Duchatelet et al. (2010), Kohlhepp et al. (2011), and Kohlhepp et al.

(2012). Overall, bootstrap methods are widely used to determine uncertainties, also for many other types of measurements and model results.

4.2 Limitations of the trend determination

The trend results and their uncertainties determined by fitting function (4.1) and by the above-described bootstrap method (Section 4.1), respectively, are sensitive to a variety of factors. The influence of some of them is evaluated in this section. Among the investigated factors are the sensitivity with respect to the architecture of the fitting function, to the time of year chosen for the analysis, time series length, and sampling (Section 4.2.1). For this investigation, FTIR measurement time series of HCl, $ClONO_2$, and HF from 17 sites belonging to the Network for the Detection of Atmospheric Composition Change (NDACC) are used, and additionally the corresponding results from the two chemistry-transport models (CTMs) KASIMA and SLIMCAT. These data sets are described in Section 5.1. The dependency of the trend results on including time series of the quasi-biennial oscillation (QBO) and the 11-year solar cycle in the fitting function is investigated in Section 4.2.2. This analysis is conducted only for measurements from the three sites Jungfraujoch, Kiruna, and Izaña.

4.2.1 Dependency on time series length, the fitting function, and sampling

The length of a time series necessary to significantly determine a certain trend depends on the size of this trend and on the standard deviation and the autocorrelation of the data (Weatherhead et al., 1998). The measurement time series analysed in the present work are about 16 years long, or shorter, and the expected trends amount to about $\pm 1\%$/yr. The autocorrelation is difficult to determine because the time series are irregularly sampled, and some of them contain gaps of several months. This is why we determine the influence of different factors on the resulting trend directly. The data used in this section are the FTIR daily mean time series which are described and further analysed in Chapter 5. The analyses reported in this section (4.2.1) have been published already by Kohlhepp et al. (2012).

Dependency on the time period and time series length

The three different time periods chosen for the investigation of the trend dependency on the time period and time series length are 1996–2009, 2000–2009, and 2004–2009. It would not be possible to determine a reliable linear trend for the two chlorine species if data recorded before 1996 were included because the stratospheric inorganic chlorine loading reached its maximum around this time (e.g., Rinsland et al., 2003; Newchurch et al., 2003; Froidevaux et al., 2006; Lary et al., 2007). Anyway, not many of the sites included in the study of Kohlhepp et al. (2012) began measuring before 1996. More than half of the sites measured from 1996 on. The longer the time series, the smaller the trend uncertainty is expected to be. Most of the measurement sites started operation between 1996 and 2000 (see also Table 5.1) so that for the time range 2000–2009, a very good comparison and overview on the latitudinal dependency

of the trends is possible, including results from up to 16 sites. A scientific discussion on these trends can be found in Section 5.3. The period 2004–2009 was included in the sensitivity study of the present section in order to find out how strongly the trend for this 6-year period differs from the one for a longer time series. In addition, it is scientifically interesting to find out whether there is a consistent signal of a change in the rate of increase (of HF) or decrease (of HCl and $ClONO_2$) during the last few years. For this first sensitivity study, the selected fitting function was a linear trend combined with a third-order Fourier series accounting for the seasonal cycle (see function 4.1). As already mentioned above, for the time series from some of the sites, using the third-order Fourier series did not produce reliable trend results because the time series contain too large gaps. Those are the sites poleward of 70°N and S, due to polar night, and La Réunion, where the earliest measurements were performed on a campaign basis only. For these sites, a first-order Fourier series was used instead.

Figure 4.1 shows the trends of HCl, $ClONO_2$, and HF for the three time ranges discussed above. At most of the sites, the trends for the different time ranges agree within their errors. The uncertainty

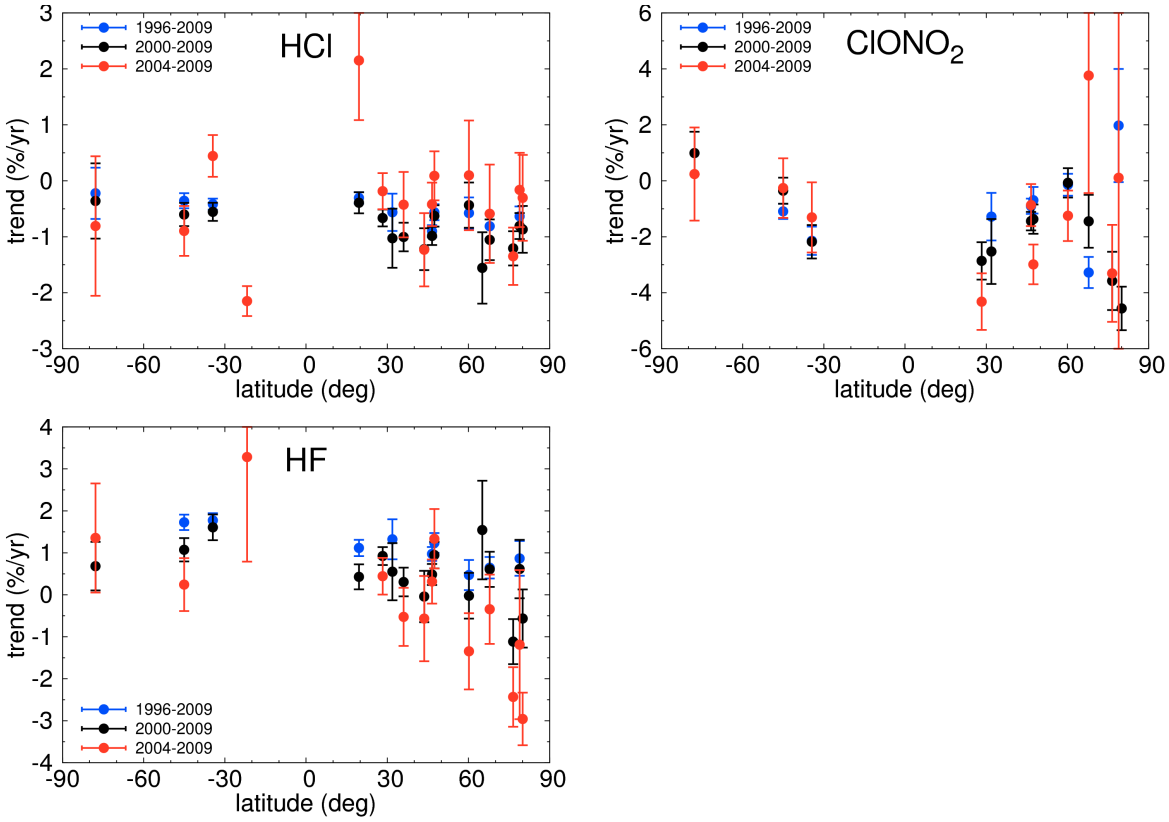

Figure 4.1: Dependence of the resulting trend (in % per year) on the time period, determined for the FTIR measurements of HCl (top left), $ClONO_2$ (top right), and HF (bottom). Please note the different y-scales. The fitting function is the linear one with seasonal cycle. The results for 1996–2009 are shown in blue, those for 2000–2009 in black (at Toronto, this is 2002–2009, and at Poker Flat it is 2000–2004) and for the 2004–2009 period in red. The error bars were determined with the bootstrap method.

calculated with the bootstrap method (Section 4.1) is larger, the shorter the time series. This is expected, mainly due to the smaller number of data points. In addition, the start and end time of the year is assumed to have a stronger influence on a short time series than on a long one. Not all results from all sites are displayed in Figure 4.1. Reasons for this are that they are unreliable due to large gaps in the time series, or that they lie outside of the displayed range. For more detailed information on which site is missing for what reason please see Kohlhepp et al. (2012). At most sites, the 1996–2009 and 2000–2009 trends lie close together, while the 2004–2009 trend differs from them.

For HCl, the northern hemisphere 2004–2009 decreasing trends seem to be weaker than those for the other two time ranges. Because this picture is so consistent, there might indeed be a slight weakening in the decrease of HCl in the last few years. However, for $ClONO_2$, no clear signal can be detected. This is probably due to the larger amplitude of the seasonal cycle in $ClONO_2$ than in HCl, especially in polar regions, combined with the large gaps due to polar night. At the other sites, $ClONO_2$ is difficult to measure due to the low total column abundance in lower latitudes, leading to a very small spectral signature only. This also results in larger error bars. So overall, we can conclude that the $ClONO_2$ trends for 2004–2009 are not very reliable, while the HCl trends for the same time range might show a real tendency, although their values should not be trusted exactly either. For most HCl and also some $ClONO_2$ time series from the northern hemisphere, the trends for 2000–2009 are slightly stronger than those for 1996–2009. This also may be a real signal, resulting from the fact that the stratospheric inorganic chlorine loading reached a plateau around 1996 and then only slowly started to decrease.

In the HF results, it is also not easy to decide which signals in the differences between the time periods are real and which result from the trends for 2004–2009 being less reliable than those for the other two time ranges. But it seems to be likely that on the northern hemisphere, there is a tendency towards weaker HF increases in the later time periods. At most of the sites, the 2000–2009 trend is weaker than the 1996–2009 result, while the weakest increase or even a decrease is mostly found for 2004–2009. This finding agrees with the results of Zander et al. (2008) who reported a stabilisation of the HF total column abundance around 2003–2004.

Concluding from this sensitivity study on the influence of time series length and the time period chosen, we can state that overall, there is good agreement between the trends calculated for the different time ranges, especially for the 1996–2009 and 2000–2009 results. The 2004–2009 trends have the largest uncertainties and are not very reliable, which is what is expected from a time series that is only 6 years long and exhibits a strong seasonal variation. However, some signals are quite consistent at a few sites and therefore should be considered to possibly be real.

Dependency on the trend calculation approach

An important characteristic of the time series analysed here is the non-negligible seasonal cycle, which is most pronounced in $ClONO_2$ at the polar sites. Concerning the reasons for these variations please see for example Section 5.2.2. Because the expected trends are relatively small (around $\pm 1\%$/yr), the

fitting function needs to represent the time series very well in order to give a reliable and significant trend estimate. In the following, we investigate on how strongly the FTIR trends of HCl, $ClONO_2$, and HF at the different sites depend on whether a Fourier series is included in the fitting function (called the "standard" approach) or not (the "linear" approach). In addition, a linear function is fitted to the data recorded between June and November on the northern hemisphere and between December and May in the Southern Hemisphere. This approach is called "summer/autumn" or "s/a" from now on. The variability is assumed to be less strong during these months. Especially at the high latitude sites, the total column abundances of the chlorine species are strongly influenced by the polar vortex during the winter and early spring months which are excluded in the summer/autumn approach.

A comparison between the three mentioned trend determination approaches is shown in Figure 4.2 for HCl, $ClONO_2$, and HF measured by the FTIR instruments between 2000 and 2009. The best agreement

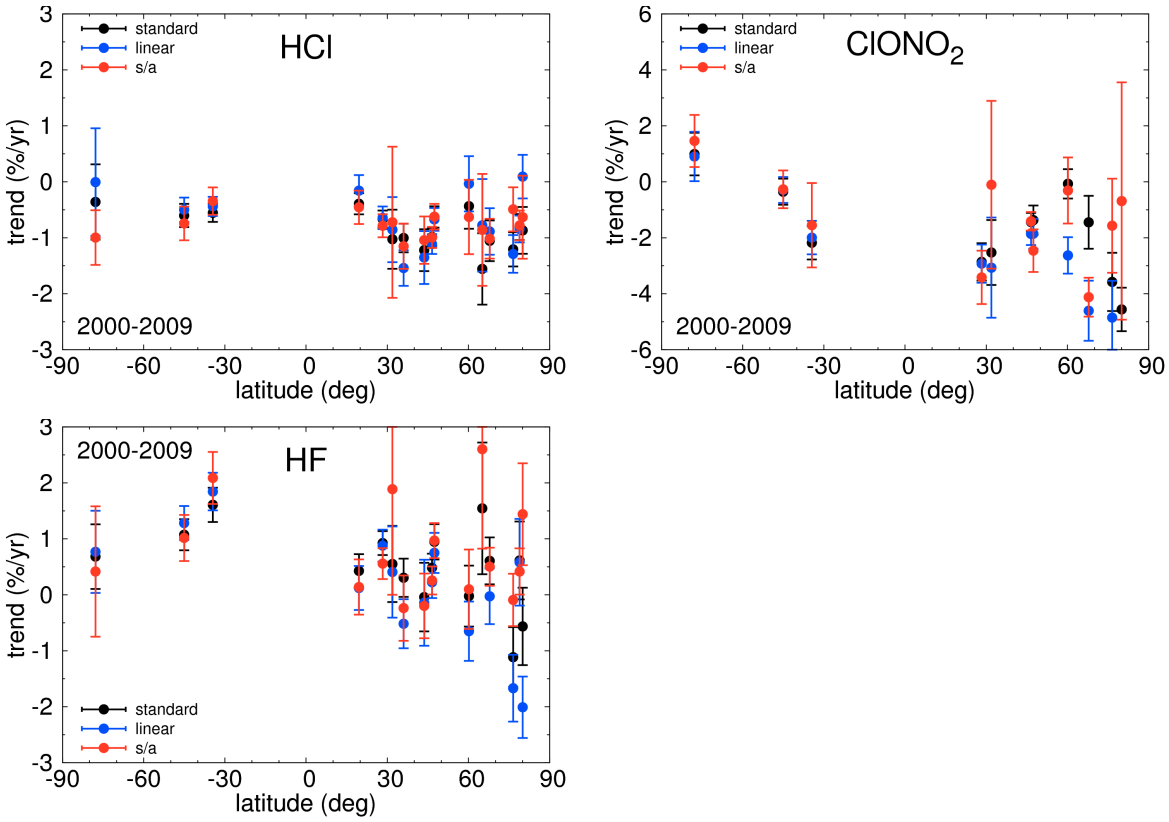

Figure 4.2: Dependence of the resulting trend (in % per year) on the type of fitting function, determined from the FTIR measurements of HCl (top left), $ClONO_2$ (top right), and HF (bottom) for the time range 2000–2009 (except at Toronto where it is 2002–2009, and at Poker Flat it is 2000–2004). Please note the different y-scales. The results of the "standard" procedure using a linear function with a third or first order Fourier series are shown in black, those of the "linear" trend calculation in blue and of the linear calculation with summer/autumn data only ("s/a") in red. The error bars were determined with the bootstrap method. Concerning the reasons for missing trend values please see Kohlhepp et al. (2012).

between the different approaches can be found for HCl, where at all sites the error bars overlap for all methods. Additionally, overall, the error bars for HCl are smaller than those for $ClONO_2$ and HF. For all three species, the confidence interval is larger for the summer/autumn and the linear method than for the standard one at most sites. This difference in uncertainty between the standard and the linear approach agrees with the assumption that including the Fourier series leads to a better representation of the time series by the fitting function, and thereby to a smaller root mean square difference between data and fit. One reason why the confidence interval for the summer/autumn approach is quite large at some of the sites is probably that the assumption of no variability during the summer months does not hold there. Moreover, the summer/autumn time series of course contain less data than the complete ones. This effect may be even stronger than expected, for example at sites where the measurements were performed on a campaign basis, or where the weather conditions are usually worse during summer and autumn than during winter and spring (see also Kohlhepp et al., 2012). The less data points, the larger the error bars. Furthermore, as has been shown by Kohlhepp et al. (2011) for FTIR measurements at Kiruna, even the trend result obtained by the standard approach is sensitive to the start and end time of the year. This effect is assumed to be even stronger if only a linear function is fitted so that part of the difference between the approaches may be due to this.

We can conclude from this investigation that the "standard" approach to fit a linear function and a Fourier series leads to the smallest error bars among the three methods tested here. It is therefore assumed to give the most reliable trend results. For HCl, there is no significant difference to the other methods. However, when looking at the fits to the data (not shown here), it is obvious that also the Fourier series is not able to completely represent the sometimes very large and sudden peaks occurring at high-latitude sites in $ClONO_2$ at the end of the winter, for example. These peaks usually result from the movement or break-up of the polar vortex. Especially the Arctic vortex exhibits a large intra-annual and inter-annual variability so that the peaks usually do not occur at exactly the same time, which would be necessary for the periodic Fourier series to be able to capture this feature.

Influence of sampling

Another general characteristic of time series from solar FTIR absorption measurements is their irregular sampling, especially when considered on a daily basis. It results from the dependency on direct sunlight. No measurements are possible during nighttime and when the sky is cloudy. As a result, large gaps may occur in the time series, especially at the high latitude sites where polar night lasts a few months. In the following, we try to investigate the influence of these larger and smaller regular and irregular gaps on the resulting trend. For this purpose, we use simulations by chemistry-transport models (CTMs). A trend is determined from the complete time series which consists of one value per day, and another one when using only the values of the days at which FTIR measurements are available, from that same model time series. This was done for simulations by two different CTMs, KASIMA and SLIMCAT, which are described in Section 5.1. These CTM results are well suited for this purpose because SLIMCAT

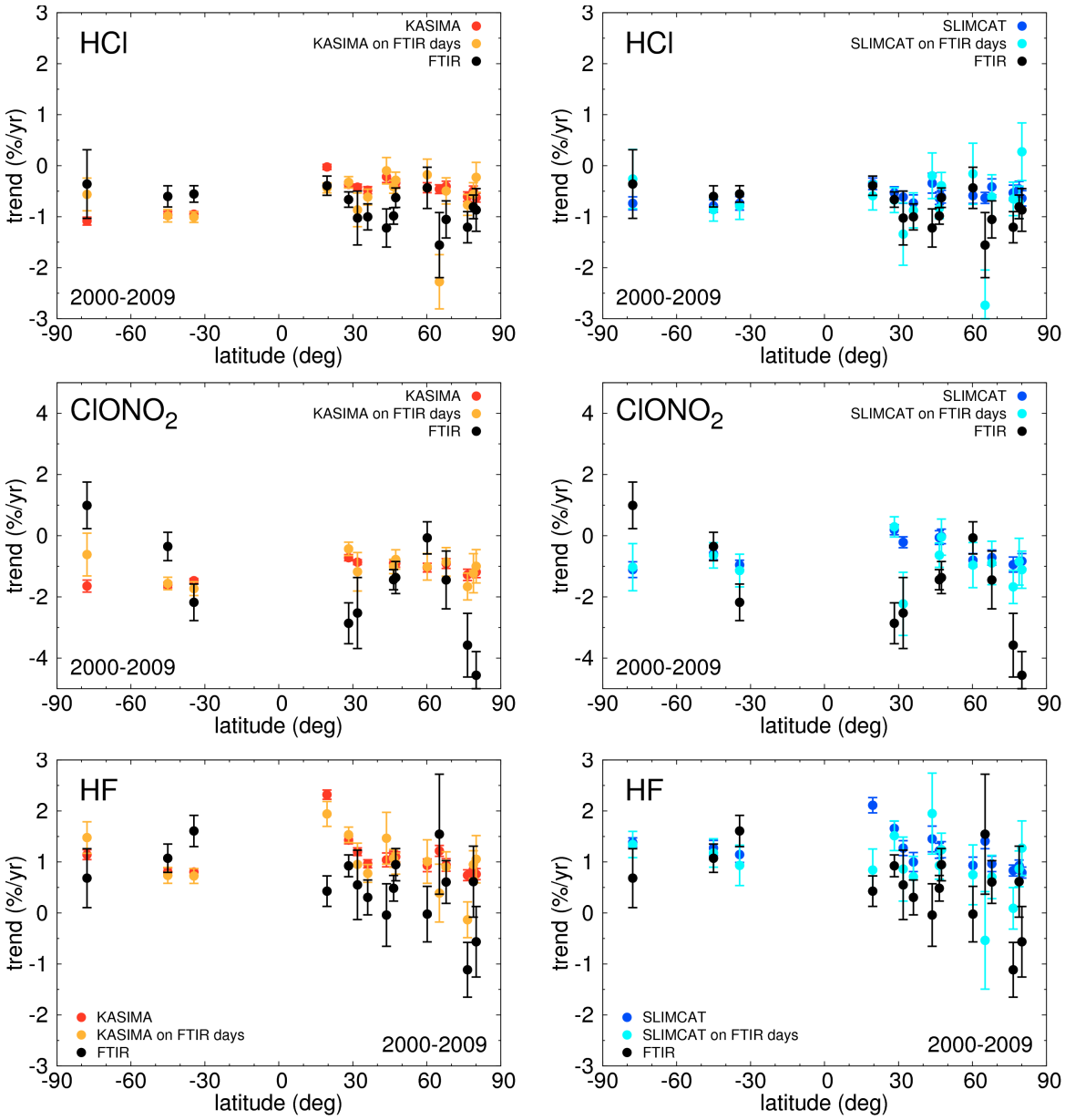

Figure 4.3: The dependence of the resulting trend (in % per year) on sampling is investigated by comparing trends from the KASIMA data on all days (left column; red) with those calculated from the model time series on days with FTIR measurements only (orange) and with the FTIR trends themselves (black). The same comparison is shown for SLIMCAT (right column; blue) and SLIMCAT only on FTIR days (cyan). Please note the different y-scales. The error bars were determined with the bootstrap method.

used re-analysis data and KASIMA was nudged to re-analysis and analysis fields so that on every single day, the meteorological fields simulated by the models are expected to correspond to the real state of the atmosphere. The influence of sampling on the trend should therefore be even more realistically reproduced than it would be by using the chemistry-climate model (CCM) simulations described in Section 5.1 that created their own independent meteorology and dynamics of the atmosphere. The fitting

function used was the linear one, combined with a third- or first-order Fourier series accounting for the seasonal cycle, and the error bars were determined with the bootstrap method. The time range considered is 2000–2009 because most sites measured during this period.

Figure 4.3 shows a comparison of the FTIR results with the two different model trends, for KASIMA (left column) and SLIMCAT (right column). There is no clear signal as to whether the trend from the daily model series or from the one with FTIR sampling agrees better with the FTIR trends. At most sites, the two model trends agree within their bootstrap errors. The sites where this is not the case are mostly located at high latitudes where we expect the influence of sampling to be largest, as a result of the gaps due to polar night, combined with the relatively large amplitude of the seasonal cycle. In addition, the variability of the considered species at these high latitude sites is especially strong in winter and spring when the sites are sometimes located underneath the polar vortex, sometimes outside of it, or underneath its edge. We can conclude from this investigation that although we cannot quantify it, we must keep in mind that especially at the high-latitude sites, the influence of sampling on the trend may not be negligible.

4.2.2 Influence of multi-annual variations

Apart from a linear decrease or increase and the seasonal cycle which is accounted for in this work by a Fourier series, the time series of an atmospheric species may contain signatures of dynamical or chemical variations on longer timescales, e.g., a few years or decades. They might considerably or even significantly influence the trend result or at least its error bars, thereby depending on the time series length and the strength of the influence. These longer-scale variations include for example the 11-year solar cycle and the quasi-biennial oscillation.

The 11-year solar cycle is a variation in the solar irradiation reaching earth, with an amplitude of about 0.17 W/m^2, or 0.07%, peak-to-peak (Gray et al., 2010). Due to the dependency of the irradiation change on wavelength, and through dynamical feedbacks, the resulting impact on the atmosphere can be much larger than what would be expected from this small relative change in total irradiation. The 11-year solar cycle is associated with the sunspot number on the Sun's photosphere. When this number reaches its maximum, also the solar irradiation peaks. This is not obviously expected because the sunspots are darker and therewith colder parts of the photosphere, but their existence is compensated by a likewise larger than usual number of faculae during solar maximum. Faculae are hotter spots that are not visible as well as the larger dark sunspots (Gray et al., 2010). In many studies, this change in solar irradiation has been shown to modify stratospheric meteorological variables like temperature and zonal wind (e.g. Labitzke and van Loon, 1988; Lu et al., 2009; Gray et al., 2010). The correlation of the stratospheric ozone concentration and the atmospheric ozone total column abundance with the 11-year solar cycle has been intensely investigated and described by e.g. Steinbrecht et al. (2003), Sinnhuber et al. (2006), WMO (2007), Gray et al. (2010), Muncaster et al. (2011), and Efstathiou and Varotsos (2012). Similarly to the stratospheric NO_y budget (Legrand et al., 1989) (NO_y = NO + NO_2 + NO_3 + 2 N_2O_5 + $BrONO_2$

+ $ClONO_2$ + HNO_3 + HNO_4), O_3 in the upper and middle stratosphere is influenced by solar variability especially directly through the dependency on photochemical processes, while the influence on the lower stratosphere occurs mostly indirectly through dynamical changes (Efstathiou and Varotsos, 2012).

In addition, these stratospheric 11-year solar signals are modulated by the quasi-biennial oscillation (QBO) (Labitzke and van Loon, 1988; WMO, 2007; Lu et al., 2009; Efstathiou and Varotsos, 2012). The name QBO refers to a variation of the equatorial stratospheric zonal wind between easterly and westerly direction, with a period of roughly 28 months, on average (e.g., Baldwin et al., 2001). This oscillation is probably driven primarily by gravity waves that were generated by deep convection in the tropics. Despite being a tropical phenomenon, the QBO affects the whole stratosphere by modulating the effects of extratropical waves and may even influence the troposphere and mesosphere (Baldwin et al., 2001).

The number density of the gases primarily investigated here (HCl, $ClONO_2$, and HF) peaks in the stratosphere (see profiles in Section 2.2).They might therefore be influenced by the changes occurring there in chemistry and dynamics associated with the 11-year solar cycle and the QBO. As the time series considered here are only about 13–16 years long, the trends determined from them could be affected in this case.

In order to investigate a possible signature of the solar cycle and the QBO in the trace gas time series, a multiple linear regression was performed. For this purpose, the fitting function described in Section 4.1 was extended by the possibility to scale and include one or more normalized time series of any desired predictor. In this work, the solar 10.7 cm flux and/or the equatorial zonal wind at 10 and 30 hPa above Singapore representing the QBO were used. These two heights bearing QBO signals that are out of phase by nearly $\pi/2$ were chosen in order to get the phasing correctly, thereby following Steinbrecht et al. (2003). The normalized time series are shown in Figure 4.4.

The fitting function used here then reads

$$f(t) = p_1 (1 + p_2 t) \left\{ 1 + \sum_{i=1}^{3} [q_i \cos(2i\pi t) + r_i \sin(2i\pi t)] + \sum_{j=1}^{3} [s_j d_j(t)] \right\} \qquad [4.2]$$

where $d_j(t)$ represents the normalized predictor time series, and s_j are the parameters scaling these datasets to give the best linear least squares fit to the trace gas data. In this work, not more than three predictors were used at the same time (the solar flux and two QBO series), but of course, technically, more would be possible. Except for the last term, function 4.2 corresponds to function 4.1.

To estimate the error bars of the fitting parameters, again the bootstrap method was applied (see Section 4.1). From 5000 additional fits to different artificial datasets, the 97.5 and 2.5 percentiles for each parameter could be determined, from which a mean precision was calculated.

This procedure was applied to the time series of the HCl, $ClONO_2$, and HF total column abundances for the time periods 1996–2011 (at Jungfraujoch and Kiruna) and 1999–2011 (at Jungfraujoch, Kiruna and Izaña). The influence of the solar cycle is expected to be stronger on the chlorine gases than on HF due to the dependency of especially $ClONO_2$ formation on the availability of NO_2. NO_y again is directly

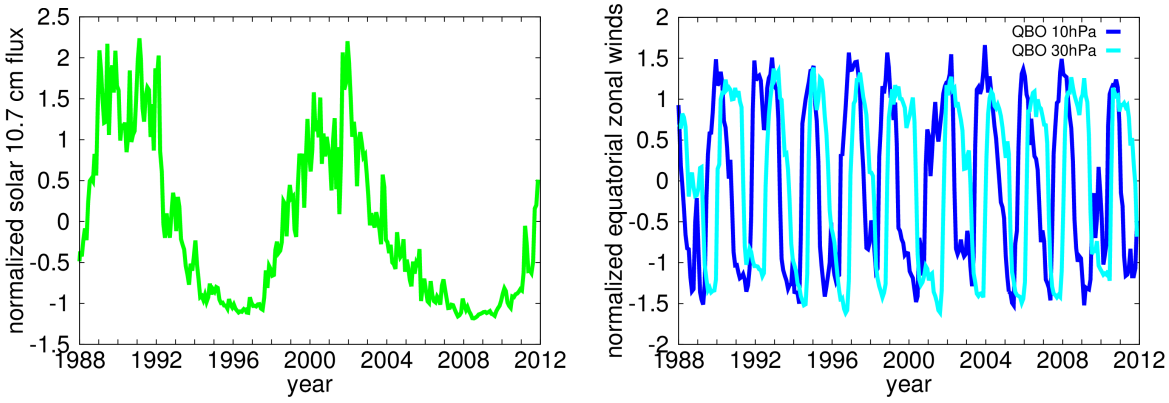

Figure 4.4: Time series of the solar 10.7 cm flux (left), and of the equatorial zonal winds on the 10 and 30 hPa pressure levels above Singapore (right), showing the quasi-biennial oscillation. All three time series were normalised to mean zero and standard deviation 1. The data sources are ftp://ftp.geolab.nrcan.gc.ca/data/solar_flux/monthly_averages/solflux_monthly_average.txt for the solar 10.7 cm flux, and http://www.geo.fu-berlin.de/met/ag/strat/produkte/qbo/singapore.dat for the QBO.

influenced by photolysis rate changes occurring in the course of the solar cycle, in particular in the upper and middle stratosphere (Legrand et al., 1989).

The dependency of the scaling factor value on the fitting function was tested, for the function containing a linear trend or not, the solar flux predictor or the QBO predictors only, and both the solar flux and the QBO. Results were compared when using the monthly means, the deseasonalised monthly means, and the annual means of the respective gases. Only in case of the monthly mean time series, the third order Fourier series was included in the fitting function. The deseasonalisation was performed by dividing the monthly means by the normalised mean monthly means determined for the complete time series (referring to the corresponding annual means).

In Figures 4.5 and 4.6, the results for the fits of the above described different regression functions to the deseasonalised mean monthly mean data sets of HCl and $ClONO_2$ above Kiruna are presented, respectively. From a first glance, one gets the impression that, at least for the examples shown here, the fit is much worse without incorporating the linear trend. For HCl, the influence of the solar cycle on the total column abundance is not easily visible, but a QBO signal seems to be detectable, corresponding very well to the phase of the QBO seen in the 10 hPa equatorial zonal winds. The dominating QBO signal in $ClONO_2$ at Kiruna corresponds well to the phase at the 30 hPa level above Singapore, but peaks slightly earlier. This shifted peak can be represented by the smaller but non-negligible contribution from 10 hPa to the fit. The solar flux influence on $ClONO_2$ at Kiruna is not very well visible in this presentation, either.

As the original predictor time series were all normalised by their standard deviation, and the mean value was subtracted, the scaling factors determined in the linear regression can be directly intercompared

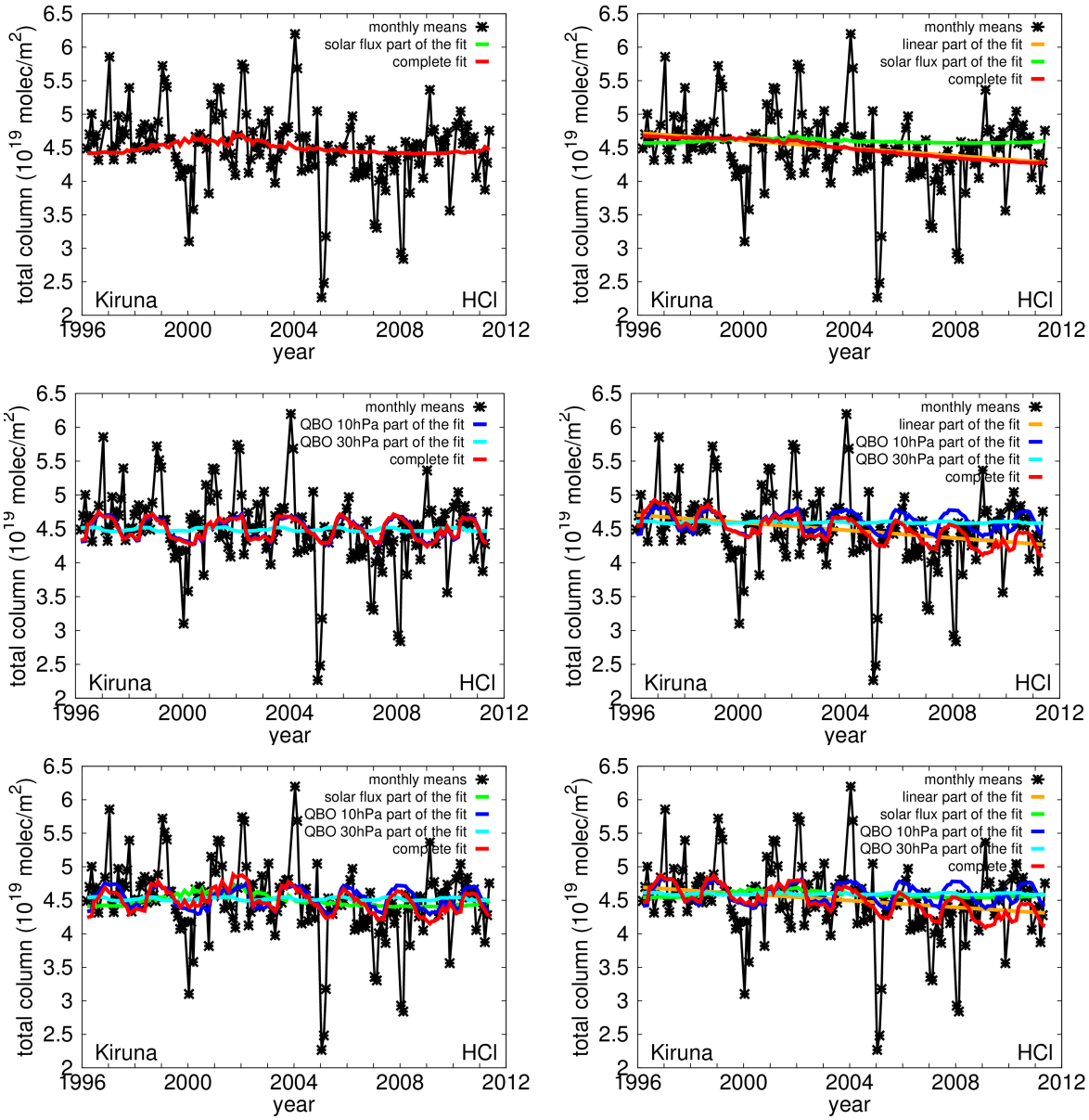

Figure 4.5: Fit results from the multiple linear regression performed for the deseasonalised time series of the total column abundances of HCl measured by the FTIR in Kiruna. The left column shows all fits without a linear trend included, in the results shown in the right column, a linear function was included. For the top line fits, the only predictor time series was the solar 10.7 cm flux, for the middle line, it was only the QBO at 10 and 30 hPa, and for the last line, both solar flux and QBO were included in the fitting function.

to quantitatively determine the relative influence of the respective predictors for every gas. There is no strong difference as to whether the deseasonalised monthly mean time series, the annual mean time series or the monthly mean time series are used (in the latter case with a third order Fourier series included in the fitting function). Neither does the value of the scaling factors depend significantly on the other predictors

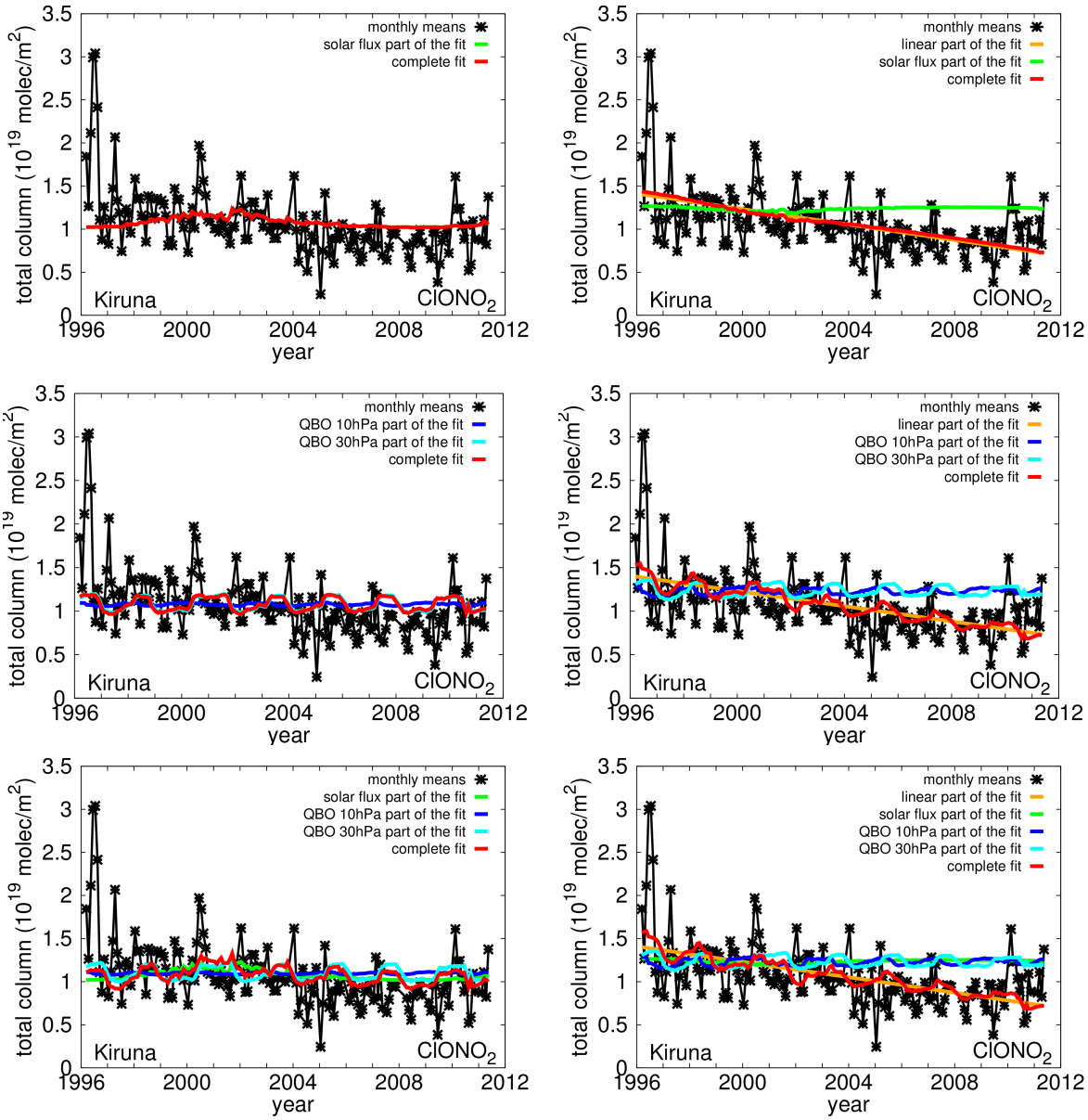

Figure 4.6: Like Figure 4.5, but for $ClONO_2$.

used in the regression function. For this reason, only the results for the deseasonalised monthly mean time series and the fitting function including both the solar flux and the QBO are shown in Figure 4.7. The largest scaling factors resulted for the solar flux influence on $ClONO_2$ in most cases, followed by the 10 hPa QBO influence on HCl. Especially at Kiruna, the difference between the two time ranges in the solar flux scaling factor is considerably large. This can be expected because the time range 1999–2011 covers only about one cycle of the solar flux variation. The correlation between the QBO at 10 hPa and the HCl time series at Kiruna is significantly positive.

As mentioned above, it is already known that the solar flux signal in the stratosphere may be modulated by the QBO. Analogously to e.g. Labitzke and van Loon (1988) and Lu et al. (2009), the deseasonalised

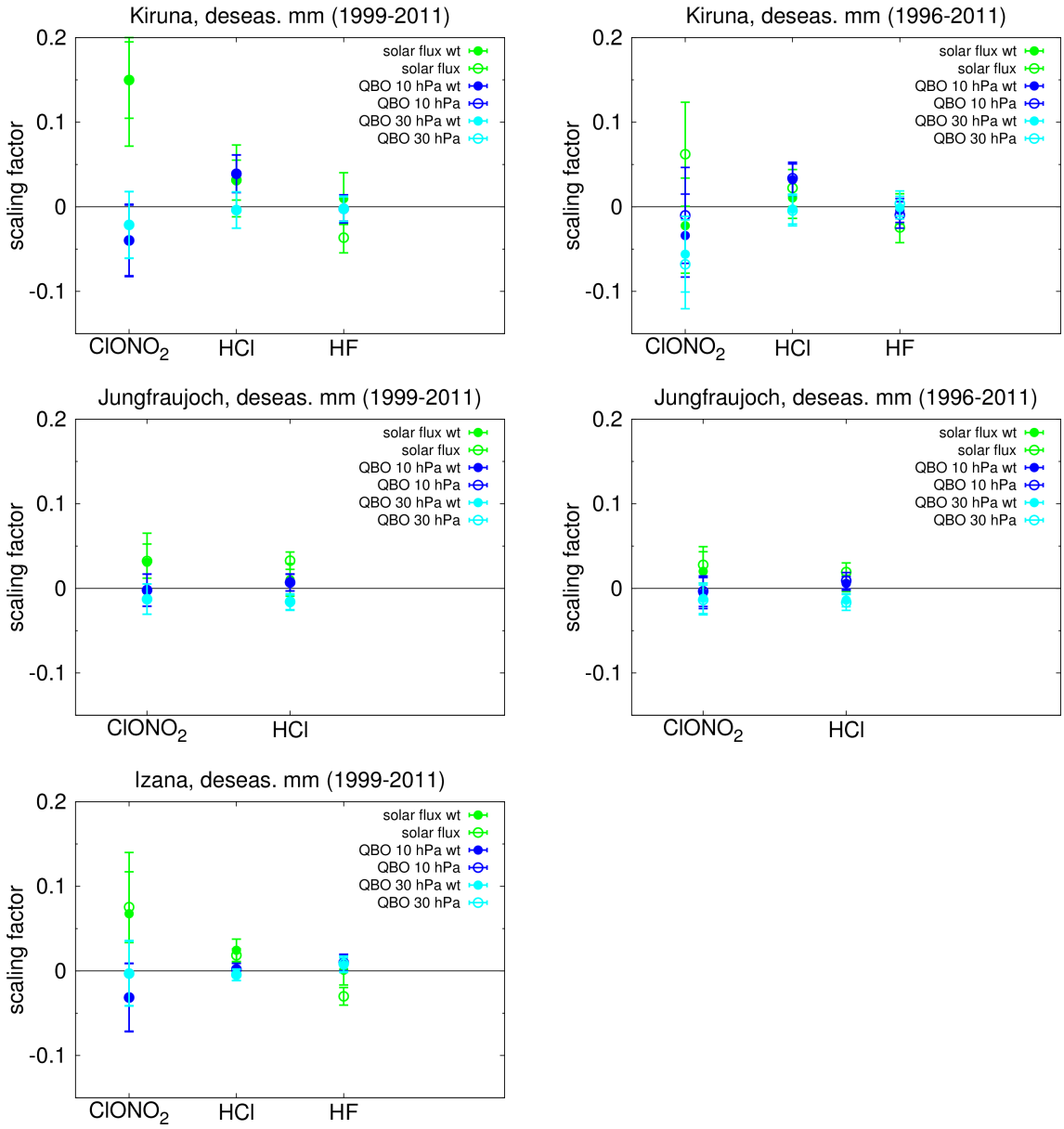

Figure 4.7: Scaling factors for the multiple linear regression to the deseasonalised monthly mean time series of HCl, $ClONO_2$, and HF above Kiruna, Jungfraujoch, and Izaña, for the time ranges 1996–2011 (right) and 1999–2011 (left), where available. The fitting function included both the solar 10.7 cm flux and the QBO on the 10 and 30 hPa levels. In each picture, two values are shown for each parameter, one from the fit with a linear trend included in the fitting function (wt) and one from the fit without. The fitted predictor time series were normalised to mean 0 and standard deviation 1 so that the factors indicate the relative strength of the influence of the corresponding predictor.

monthly mean time series of $ClONO_2$, HCl, and HF were separated into QBO east and west phase according to the equatorial stratospheric zonal winds at the 10 and 30 hPa pressure levels. Months with mean absolute wind values less than 2 m/s were excluded from the analysis, following Lu et al. (2009).

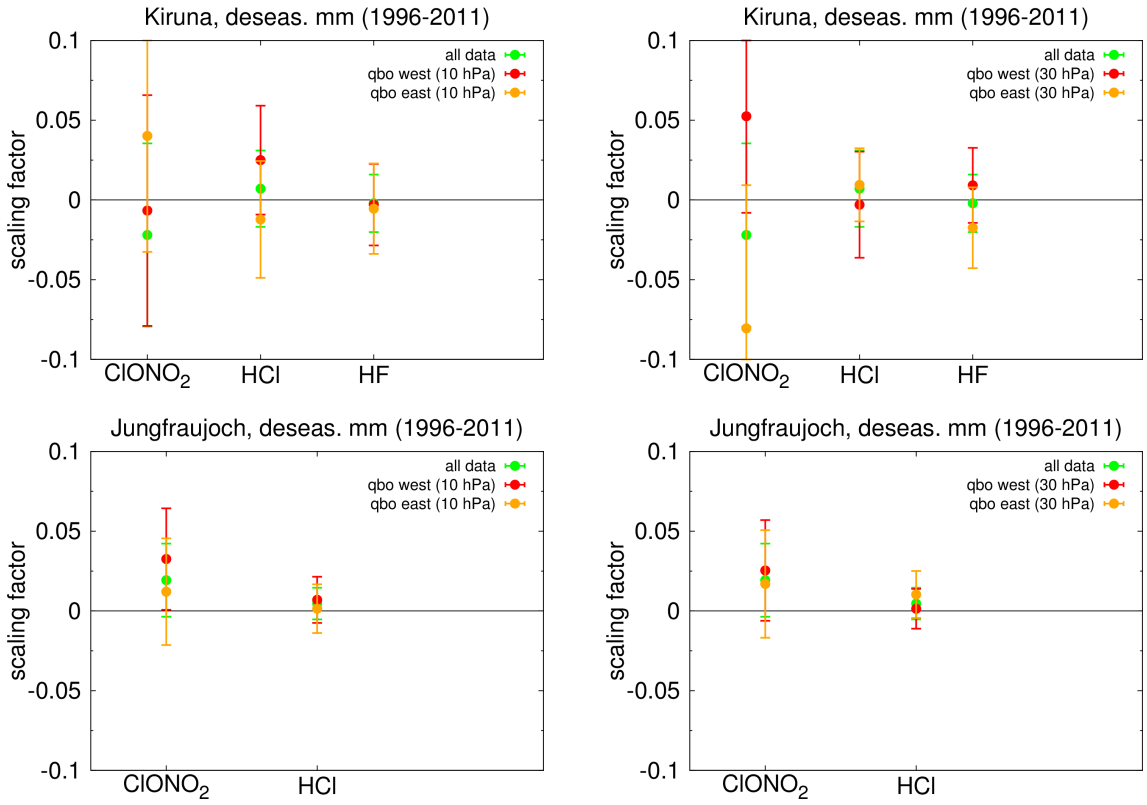

Figure 4.8: Scaling factors for the multiple linear regression fits of the solar 10.7 cm flux to the FTIR time series of $ClONO_2$, HCl, and HF, at Kiruna (top line) and Jungfraujoch (bottom line). A linear trend was included in the fitting function. The time range shown is 1996 to 2011. The factors were determined for the whole data set of deseasonalised monthly means, and also for this time series split up into months with QBO east and west phase. This separation according to QBO east and west phase was done once from the equatorial zonal winds at the 10 hPa pressure level above Singapore (left), and once for the winds at the 30 hPa level (right).

Then, a multiple linear regression with the solar flux as only predictor was performed on the QBO east and west parts of the data sets separately. The resulting scaling factors for the Kiruna and Jungfraujoch time series are displayed in Figure 4.8, where the data have once been separated using the QBO on the 10 hPa pressure level as separation criterion, and once using the 30 hPa QBO data. Firstly, it can be stated that obviously none of the differences between the scaling factors calculated for the QBO east and west phases are significant. But especially when applying the QBO at 30 hPa as separation criterion, the $ClONO_2$ time series at Kiruna shows a dependency even of the sign of the solar flux scaling factor on the QBO phase. More precisely, the correlation between the solar flux and the total column abundance of $ClONO_2$ is positive during the QBO west phase and negative during the QBO east phase, with a very similar absolute value of the scaling factor. Using the QBO phase at 10 hPa as separation criterion reveals qualitatively the opposite result for $ClONO_2$, with slightly weaker absolute scaling factors. The

influence on HCl and HF again does not seem to be as strong. There is a slightly positive correlation between HCl and the solar flux while the QBO at the 10 hPa level is in its west phase, and a slightly negative correlation during the QBO east phase at the 10 hPa level. For HF, there is no dependency neither on the solar flux nor on the QBO phase if separated according to the 10 hPa pressure level QBO, but a slightly positive correlation with the solar flux during the QBO west phase at 30 hPa, and a slightly negative correlation during the corresponding QBO east phase. Of course, the results from the different separation criteria are expected to differ because the QBO phases are shifted by about $\pi/2$, but there is no way to decide which QBO level may be more suitable for which gas at which location. Above Kiruna, the 30 hPa QBO may have a stronger influence on the correlation of $ClONO_2$ with the solar flux than the 10 hPa QBO. In contrast, the 10 hPa QBO seems to influence the correlation between HCl and the solar flux more strongly than the 30 hPa QBO does. This may be connected with the $ClONO_2$ mixing ratio reaching its maximum slightly lower in the stratosphere than HCl (please compare the profiles in Figure 2.4).

Overall, the signals for the Jungfraujoch data are very similar to those for Kiruna, but weaker in amplitude. The only discrepancy occurs for the $ClONO_2$ time series separated according to the QBO 10 hPa criterion, where the results correspond better to those at the Jungfraujoch when the separation is done with the 30 hPa QBO than to the Kiruna results when applying the same criterion. At the Jungfraujoch, the signals are much too weak for a statement on whether the QBO at the 10 hPa level or the QBO at the 30 hPa level may have a stronger influence on the correlation between the solar flux and the different species.

Concluding on the analysis and comparison of the scaling factors, it can be stated that especially for $ClONO_2$ at Kiruna, the influence of the solar flux is non-negligible and in general the larger, the shorter the time series. Also the influence of the QBO on HCl and HF can be detected by this method. The dependency of the correlation with the solar 10.7 cm flux on the QBO phase is very interesting although not significant.

The essential question of this section for the trend analyses performed in Chapters 5 and 6 of this work is whether or how strongly the trends of the considered gases depend on the inclusion of one or more predictors in the fitting function. This question is addressed in Figure 4.9, where the trend results for the deseasonalised monthly mean time series at Kiruna, Jungfraujoch, and Izaña are presented for the periods 1999 to 2011 and 1996 to 2011, where available. There is no big difference in the general features if the monthly mean time series (with a third order Fourier series included in the fitting function) or the annual mean series are used instead of the deseasonalised one.

It is obvious that there is no significant, distinguishable influence on the 1996–2011 trends at Kiruna and Jungfraujoch (Figure 4.9, right column). The trend of $ClONO_2$ at the Jungfraujoch is slightly weaker when the fitting function contains the solar flux time series. In contrary to the 1996–2011 trends, those for 1999–2011 of some of the gases are quite strongly, but (due to their large error bars) also not significantly influenced by including the solar flux in the regression function. With the solar flux, the $ClONO_2$ and HCl

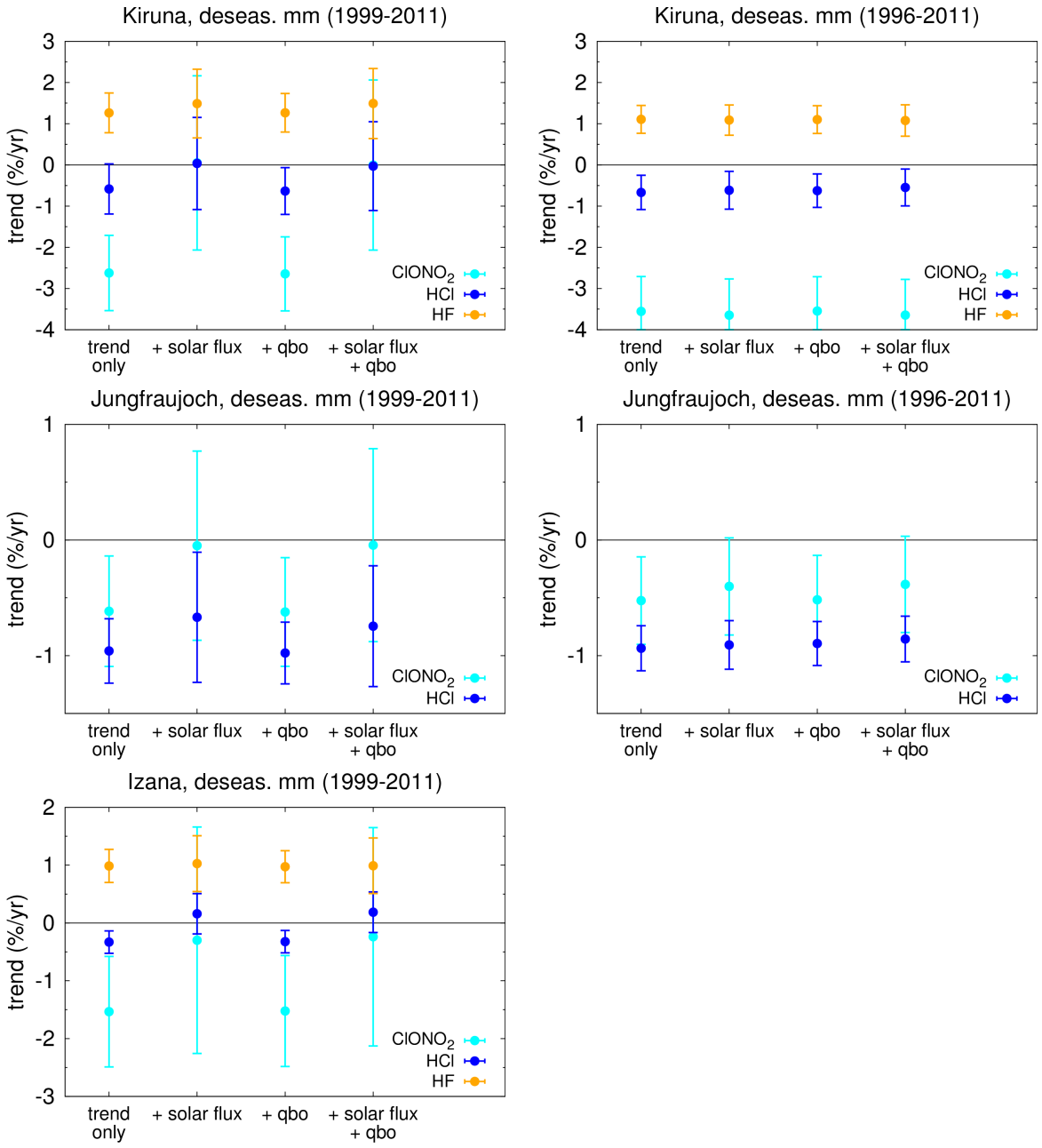

Figure 4.9: Trend results for different multiple linear regression functions for the time ranges 1999 to 2011 (left column) and 1996 to 2011 (right column), for the deseasonalised mean monthly mean time series of $ClONO_2$, HCl, and HF above Kiruna (top row), the Jungfraujoch (middle row), and Izaña (bottom row). The trends were determined when the solar 10.7 cm flux, the quasi-biennial oscillation (QBO) in 10 and 30 hPa, or both the solar flux and the QBO were included in the fitting function, and are compared here with the trend results from a simple linear regression.

trends at all three sites Kiruna, Izaña, and Jungfraujoch between 1999 and 2011 are weaker than without the solar flux. The reason for this is probably that part of the decrease is attributed to the decrease in

the solar 10.7 cm flux at that time, following the maximum around the year 2001 (see also Figure 4.4). However, the trends calculated for 1999–2011 without solar flux correspond very well to those for 1996–2011 (which are similar whether or not the solar flux is included), for both sites Jungfraujoch and Kiruna. Only the trends for 1999–2011 with the solar flux included are different. As discussed for example in Section 5.3, no significant change in the rate of increase or decrease is expected between 1996 and 1999 for all of these gases. For these reasons, we assume that the difference in the trend results for 1999–2011 between including or not including the solar flux in the fitting function is only an artificial effect that occurs because the time series consist of only about 13 years, not much more than one cycle of the solar flux variation. This assumption is supported by the fact that the effect on the 1996–2011 trends, in contrary, is negligible.

The positive HF trend at Kiruna for 1999–2011 increases slightly with the solar flux included in the fitting function because a very small but not significant positive correlation is found in the regression (see also Figure 4.7). The trends for 1996–2011 are undisturbed, so that qualitatively the same argumentation as for the $ClONO_2$ and HCl trends holds for HF, too.

In this section, the influence of some multi-annual variations on the trend determination with the method described in Section 4.1 was investigated. No considerable change in the trends was found when including the QBO in 10 and 30 hPa in the multiple linear regression function. Concerning the 11-year solar cycle, a not significant but non-negligible impact on the trends of HCl, $ClONO_2$, and HF was found for the shorter time range 1999–2011, but not for 1996–2011. But as the 1999–2011 trends without solar flux agree better with the 1996–2011 trends than those for 1999–2011 with the solar flux included do, it is concluded that the change occurring in the 1999–2011 trends is an artificial effect and that the solar cycle does not significantly influence the trend results calculated with the method described in Section 4.1.

Some side aspects dealt with here like the dependency of the solar flux influence on the QBO phase are also very interesting and would be worth to be investigated further.

4.2.3 Conclusions

From the results in Section 4.2.1, it is obvious that the error bars for the trend are smaller, the longer the analysed time series, as expected. However, many more NDACC sites performed FTIR measurements during the period 2000–2009 than during 1996–2009, so that for the more detailed investigation and comparison with the model results in Chapter 5, the shorter time period was chosen. Among the three different trend determination approaches tested in Section 4.2.1, the “standard” one, fitting a linear trend and a first- or third-order Fourier series to the data, results in the smallest error bars. This is why it is chosen for the trend investigations in the present work. It should be kept in mind that the irregular sampling of the FTIR measurements may influence the resulting trend. This effect may be important, especially for the comparison of the FTIR measurements with the model calculations (Chapter 5), but it is not quantitatively considered because it cannot be quantified precisely. Applying the same sampling to

the model results would induce other errors in the simulations by the EMAC and SOCOL models which do not use meteorological analyses (please see Section 5.1.2 for more detailed information).

Furthermore, the influence of including the 11-year solar flux and two QBO time series in the fitting function was explored in this chapter using a multiple linear regression approach. From this analysis, no significant change of the resulting trend could be determined so that it is assumed that both longer-scale variations do not need to be considered in the extended trend analyses in Chapters 5 and 6.

5 Comparison of measurement and model data of HCl, $ClONO_2$, and HF

As already described in the introduction to this thesis, HCl and $ClONO_2$ are stratospheric chlorine reservoir species and thereby an indicator of the overall stratospheric inorganic chlorine burden. In activated form, chlorine can catalytically destroy ozone, which is why monitoring the fraction of chlorine that is present in form of the reservoir species can also indicate the strength of chlorine activation and thereby possible ozone depletion. In this thesis, the primary focus is on the temporal evolution of HCl, $ClONO_2$, and HF, and on whether the influence of the Montreal Protocol regulations concerning the so-called ozone-depleting substances can be confirmed with ground-based FTIR measurements and model results.

The results presented in this chapter were already published by Kohlhepp et al. (2012). In this study, the investigations of Rinsland et al. (2003) were continued and extended. Rinsland et al. (2003) analysed measurements of HCl and $ClONO_2$ by Fourier transform infrared (FTIR) spectrometers at 9 sites belonging to the infrared working group (IRWG) of the Network for the Detection of Atmospheric Composition Change (NDACC), until the year 2001. These ground-based data were compared to satellite measurements by HALOE at 55 km height, and to the output of a 2-dimensional atmospheric chemistry model. From these data sets, the stabilisation of the stratospheric chlorine content and thereby the effectiveness of the Montreal Protocol could be confirmed. During the last few years, the NDACC IRWG grew so that in the consecutive study by Kohlhepp et al. (2012), already 17 sites took part, which were compared with five different atmospheric chemistry models. The main purpose thereby was to investigate on whether the expected decrease of stratospheric chlorine could be confirmed with the ground-based FTIR measurements, and to test the overall ability of atmospheric chemistry models of different architecture to reproduce the measured trends. In addition to HCl and $ClONO_2$, HF was included in the study because it is expected to be influenced by the Montreal Protocol regulations, too, although it is not explicitly restricted as it is not involved in stratospheric ozone depletion. Fluorine is contained in many of the prohibited source gases, but also in some of their substitutes. This is why HF is expected to be still increasing, and why an investigation of its time development is also very interesting.

In the following, at first, the measurement and model database for this comparison is described (Section 5.1). The next section (5.2) shows a comparison of the time series of measurements and models, while Section 5.3 presents the results of a trend analysis performed on these time series, using the method described and discussed in Chapter 4. In Section 5.4, these trend results are discussed in more detail, also in the context of other studies.

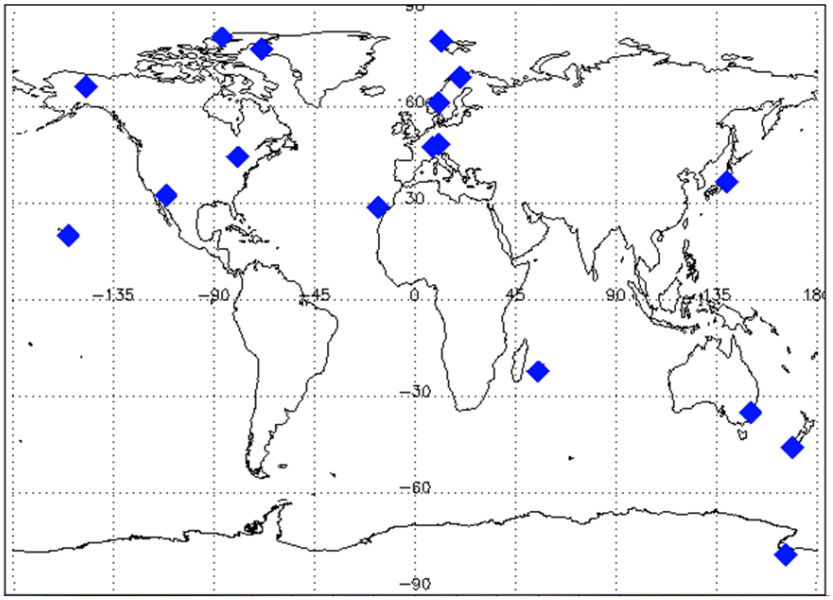

Figure 5.1: Geographical distribution of the 17 NDACC measurement sites.

5.1 Data base description

This section gives a short overview on the measurements (Section 5.1.1) and on the model data (Section 5.1.2) used in this chapter. The measurement part concentrates on describing some sites and general characteristics because a detailed description of the measurement principle, the retrieval and their error sources can be found in Chapter 3.

5.1.1 FTIR measurements at 17 NDACC sites

The measurements of HCl, $ClONO_2$, and HF analysed in this chapter stem from 17 ground-based FTIR spectrometers belonging to the NDACC. The sites are located between 77.8°S and 80.1°N, so the data presented here are able to provide a near-global overview on the total column abundances of these gases as measured from the ground (see Figure 5.1 and Table 5.1). As mentioned already in Section 4.2, a general feature that is characteristic for this type of measurements is their dependency on direct sunlight. It leads to irregular and regular gaps in the time series due to unsuitable (e.g., cloudy) weather conditions and polar night, respectively. Of course, longer gaps may also occur as a result of an instrumental breakdown. The different groups operating the instruments taking part in this study use different retrieval codes for the inversion of their spectra, namely SFIT1, SFIT2, GFIT, and PROFFIT. The latter was developed at the Institute for Meteorology and Climate Research (IMK-ASF) of the Karlsruhe Institute of Technology by Hase (2000). It is also shortly described in Section 3.2 of the present work. For more information on SFIT1 and SFIT2, please refer to Rinsland et al. (1998). The GFIT code is for example

Table 5.1: Overview of the geographical coordinates of the 17 sites and the time ranges covered by the HCl, $ClONO_2$, and HF measurements.

Measurement site	Latitude	Longitude	Altitude a.s.l. (m)	HCl meas. since	$ClONO_2$ meas. since	HF meas. since	Meas. used until
Eureka, Canada	80.1° N	86.4° W	610	1997	1997	1997	2009
Ny Ålesund, Svalbard, Norway	78.9° N	11.9° E	15	1992	1992	1992	2009
Thule, Greenland, Denmark	76.5° N	68.7° W	225	1999	1999	1999	2009
Kiruna, Sweden	67.8° N	20.4° E	419	1996	1996	1996	2009
Poker Flat, Alaska, USA	65.1° N	147.4° W	610	1999		1999	2004
Harestua, Norway	60.2° N	10.8° E	596	1994	1994	1994	2009
Zugspitze, Germany	47.4° N	11.0° E	2964	1995	1996	1995	2009
Jungfraujoch, Switzerland	46.6° N	8.0° E	3580	1984	1986	1984	2009
Toronto, Canada	43.6° N	79.4° W	174	2002		2002	2009
Tsukuba, Japan	36.1° N	140.1° E	31	1998		1998	2009
Kitt Peak, Arizona, USA	31.9° N	111.6° W	2090	1981	1980	1980	2009
Izaña, Tenerife, Spain	28.3° N	16.5° W	2367	1999	1999	1999	2009
Mauna Loa, Hawaii, USA	19.5° N	155.6° W	3397	1991		1995	2009
Réunion Island, France	21.8° S	55.5° E	50	2004		2004	2009
Wollongong, Australia	34.5° S	150.9° E	30	1996	1996	1996	2009
Lauder, New Zealand	45.0° S	169.7° E	370	1990	1990	1992	2009
Arrival Heights, Antarctica	77.8° S	166.7° E	250	1992	1997	1997	2009

described by Washenfelder et al. (2006). SFIT1 and GFIT only scale the a priori profile, so they do not retrieve any vertical information. In contrast, both SFIT2 and PROFFIT perform a profile fit, and their results were proven to agree with each other for example by Hase et al. (2004) and Duchatelet et al. (2010). Specific information on which group uses which code, on the retrieval settings, and a reference for each site can be found in the appendix of this thesis. More information on the instruments and on some special measurement conditions at each site is given by Kohlhepp et al. (2012). In the framework of this thesis, measurements with the Kiruna instrument were performed. In the following, only the sites Kiruna and Izaña are described in detail because these two are operated by the FTIR group of the Institute for Meteorology and Climate Research (IMK-ASF) at the Karlsruhe Institute of Technology, where the present thesis was produced.

The FTIR measurements in the Kiruna area were started by the above-mentioned FTIR group in the winter of 1989/90, when a home-made spectrometer called MIPAS-LM (Michelson interferometer for passive atmospheric sounding – lab model) was brought to the Esrange rocket range facility close to Kiruna in a container. Since then, campaigns aiming at measuring the Arctic stratospheric polar vortex conditions were performed every winter. From 1993/94 on, a Bruker 120 M spectrometer was used. In 1996, in a cooperation between the IMK-ASF, the University of Nagoya (Japan), and the Swedish Institute of Space Physics (Institutet för Rymdfysik, IRF), a Bruker 120HR spectrometer was set up in a laboratory in the IRF building at Kiruna (67.84° N, 20.41° E, 419 m a.s.l.). Since this time, measurements are performed on about 80 days per year, depending on the weather conditions, and with a regular gap

Table 5.2: Overview of the models. Please note that the vertical domains are pressure altitudes as most models operate on a pressure grid.

Model	Model type	Horizontal resolution	Vertical domain (approx.)	Strat. vertical resolution	Init. year	Bound. cond. (GHG / CFC scenario)	Chemical kinetics
Bremen 2-D model	2-D model	9.5°	0–100 km	∼ 3.5 km	1958	IPCC (2001) A1B / WMO (2002) Ab	Sander et al. (2006)
KASIMA	CTM	5.6°×5.6° (T21)	7–120 km	∼ 0.75–3 km	1972	IPCC (2001) A1B / WMO (2002) Ab	Sander et al. (2002)
SLIMCAT	CTM	5.6°×5.6°	0–60 km	∼ 2 km	1977	IPCC (2001) A1B / WMO (2006) A1	Sander et al. (2002)
EMAC	CCM	2.8°×2.8° (T42)	0–80 km	∼ 2 km	1958	IPCC (2001) A1B / WMO (2006) A1	Sander et al. (2002)
SOCOL	CCM	3.6°×3.6° (T30)	0–80 km	∼ 1–5 km	1960	IPCC (2001) A1B / WMO (2002) Ab	Sander et al. (2002, 2006), Atkinson et al. (2004, 2006)

between end of November and end of January due to polar night. Since July 2004, the instrument is controlled remotely. In July 2007, it was upgraded to an 125HR. This upgrade consisted mainly in a change of the electronics that helps to reduce the noise in the spectra. The Kiruna site is very well suited to investigate processes specific to the polar atmosphere with an FTIR spectrometer. In winter, it is frequently influenced by the polar vortex. At the same time, polar night does not last long because Kiruna is not very far north of the Arctic polar circle. As mentioned before, this is an essential factor for solar absorption measurements because they depend on direct sunlight. More details on the measurements at Kiruna can be found for example in Blumenstock et al. (2006).

The Izaña Atmospheric Research Center is located on Tenerife Island, at 28.30° N, 16.48° W, and 2367 m a.s.l. The observatory is run by the Spanish Weather Service (AEMET). A Bruker 120M spectrometer was operated by IMK-ASF in a container at this site between 1999 and 2005. It was replaced then by a Bruker 125HR instrument, after both were run side-by-side in April and May 2005. For O_3 and CH_4, comparisons between the different instruments were for example performed by García et al. (2012) and Sepúlveda et al. (2012), respectively. The site is very well suited for observations of stratospheric trace gases because due to the position in the subtropical Atlantic ocean at a relatively high elevation, the air is very clean (Schneider et al., 2005).

5.1.2 Five different atmospheric chemistry models

In addition to the FTIR measurements, five atmospheric chemistry models of different architecture have been used in the study by Kohlhepp et al. (2012). These are the 2-dimensional Bremen model, the 3-D chemistry-transport models (CTMs) KASIMA and SLIMCAT, and the 3-D chemistry-climate models (CCMs) EMAC and SOCOL. An overview on the models and their simulations is presented in Table 5.2, while a more detailed description can be found in Kohlhepp et al. (2012). The Bremen 2-D model is

an altitude-latitude model, so one horizontal dimension is missing. As a result, for example horizontal transport has to be parameterised. The main difference between a CCM and a CTM is that the latter makes so-called "off-line" chemistry simulations, while a CCM is an "on-line coupled" model. In a CCM, feedbacks between the chemical and dynamical field distributions are possible because they are calculated simultaneously. An example therefor would be the coupling of stratospheric ozone and temperature. In contrast, a CTM uses meteorological fields calculated by another model. These fields may be so-called analyses or reanalyses, where all available measurement data are assimilated into the model in order to create a best guess for the real state of the atmosphere. From these given meteorological fields, the CTM calculates the distribution and transport of the chemical species, but no feedbacks on atmospheric dynamics are possible. The main reason for involving the models in this study was to get an overview on how well they are able to reproduce the absolute values, the seasonal cycle, and the trends of the HCl, $ClONO_2$, and HF total column abundances, as measured by the FTIR instruments. Thereby, the influence of the differing model architecture is an interesting aspect. Furthermore, the two CTMs were used to investigate the influence of sampling on the trend result (see Section 4.2.1). With respect to Chapter 6 where a difference between the $ClONO_2$ and HCl trends is investigated, it is also very interesting to find out whether the models reproduce this feature that was seen before already in the FTIR data above Kiruna by, e.g., Mikuteit (2008) and Kohlhepp et al. (2011).

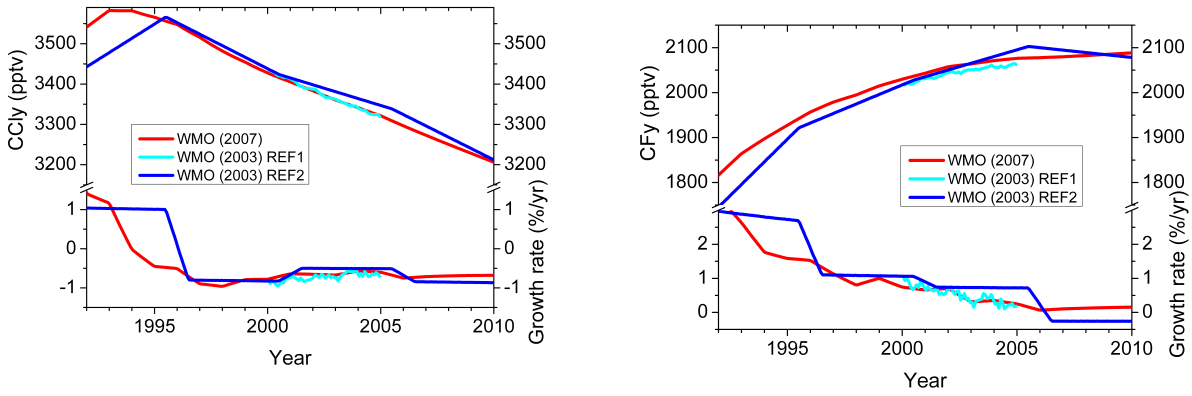

Figure 5.2: Time series of monthly mean CCl_y (left) and CF_y (right) surface volume mixing ratios (in pptv) and growth rates (in % per year) from different halocarbon scenarios, between 1992 and 2010. The one called "WMO (2003) REF2" corresponds to the scenario Ab in WMO (2003) and was used by KASIMA and the 2-D model. The "WMO (2003) REF1" time series of CCl_y and CF_y are based on that same scenario until the year 2000, but were corrected by additional measurements between 2000 and 2004. It was used by SOCOL. The "WMO (2007)" scenario is the one called A1 in WMO (2007) and was used by SLIMCAT and EMAC in this study. For the definition of CCl_y and CF_y, please see text.

All five models used the same lower boundary conditions for the emission of the most important anthropogenic greenhouse gases, i.e., CO_2, CH_4, and N_2O, corresponding to the A1B scenario of the IPCC (2001). This scenario assumes very rapid economic growth, low population growth, and the rapid introduction of new and more efficient technologies (Nakicenovic et al., 2000). In contrast, the assumptions for the emission of the source gases to ozone-depleting substances (ODS) differ slightly within the model simulations. These different scenarios can be compared in Figure 5.2, where the surface volume mixing ratios for CCl_y (3 CFC-11 + 2 CFC-12 + 3 CFC-113 + 2 CFC-114 + CFC-115 + 4 CCl_4 + 3 CH_3CCl_3 + HCFC-22 + 2 HCFC-141b + HCFC-142b + Halon-1211 + CH_3Cl) and CF_y (CFC-11 + 2 CFC-12 + 3 CFC-113 + 4 CFC-114 + 5 CFC-115 + 2 HCFC-22 + HCFC-141b + 2 HCFC-142b + 2 Halon-1211 + 3 Halon-1301 + 2 Halon-1202 + 4 Halon-2402) are shown. They originate from two consecutive WMO (World Meteorological Organization) reports on ozone depletion, and each one corresponded to the best-guess scenario at the time of its publication. KASIMA and the 2-D model used the scenario Ab of WMO (2003), while SOCOL applied a modification of this scenario with corrections from newer measurements between 2000 and 2004. The ODS boundary conditions in EMAC and SLIMCAT follow the A1 scenario of WMO (2007). All these ODS data were provided in the framework of SPARC–CCMVal (Stratospheric Processes and their Role in Climate Change – Chemistry Climate Model Validation).

For the present comparison with trends from the FTIR measurements, primarily the time range 2000–2009 was used. However, from SOCOL, data were only available until the end of 2004, and from the 2-D model until the end of 2008. The KASIMA, SLIMCAT, and EMAC output consisted of one value per day, while for the 2-D model, one value every fifth day was available, and for SOCOL, it was only the monthly means.

5.2 Time series comparison

In this section, the time series of HCl, $ClONO_2$, and HF from models and measurements are compared with respect to the agreement of the absolute total column abundances (Section 5.2.1) and of the mean seasonal cycle (Section 5.2.2).

5.2.1 Absolute total column abundances

For an overview, the time series of models and measurements of HCl, $ClONO_2$, and HF are shown in Figures 5.3 to 5.5, respectively. A more quantitative comparison is performed in Table 5.3, where the mean differences between the models and measurements are presented, averaged over all sites where FTIR results were available. The differences for KASIMA and SLIMCAT were calculated from the daily values, while for EMAC, SOCOL, and the 2-D model, the monthly means were used. The reason for this is that the latter three did not use meteorological analyses or reanalyses as boundary conditions. EMAC and SOCOL created their own independent meteorology, while the 2-D model used the daily Montgomery potential from meteorological analyses of one single year and repeated this cycle over and over. So these three model simulations cannot be compared to the measurements on a daily basis, but

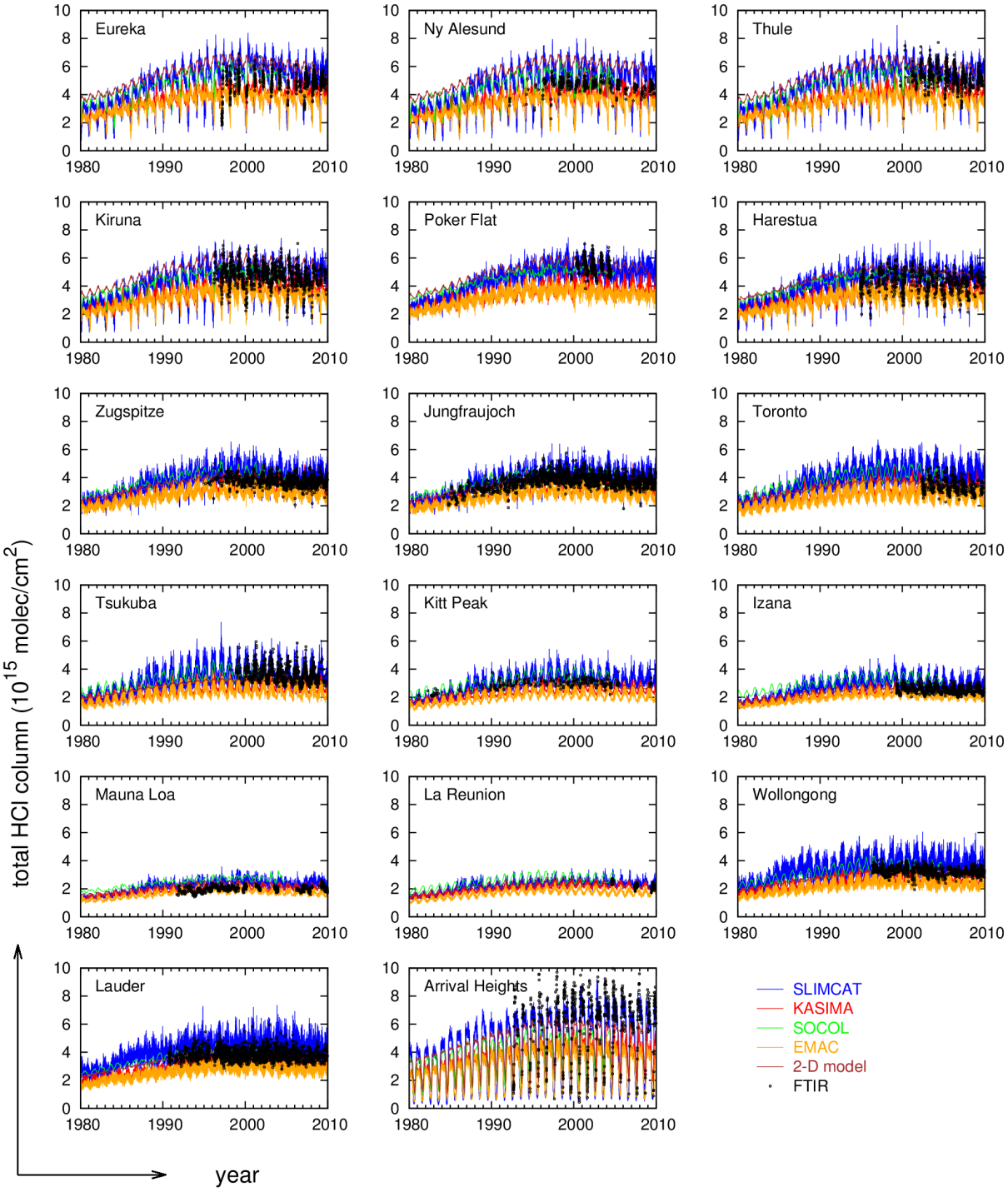

Figure 5.3: Time series of HCl total column abundances in molecules per cm^2 at the different sites as measured by FTIR (black dots) and simulated by SLIMCAT (blue line), KASIMA (red line), SOCOL (green line), EMAC (orange line), and Bremen 2-D model (brown line).

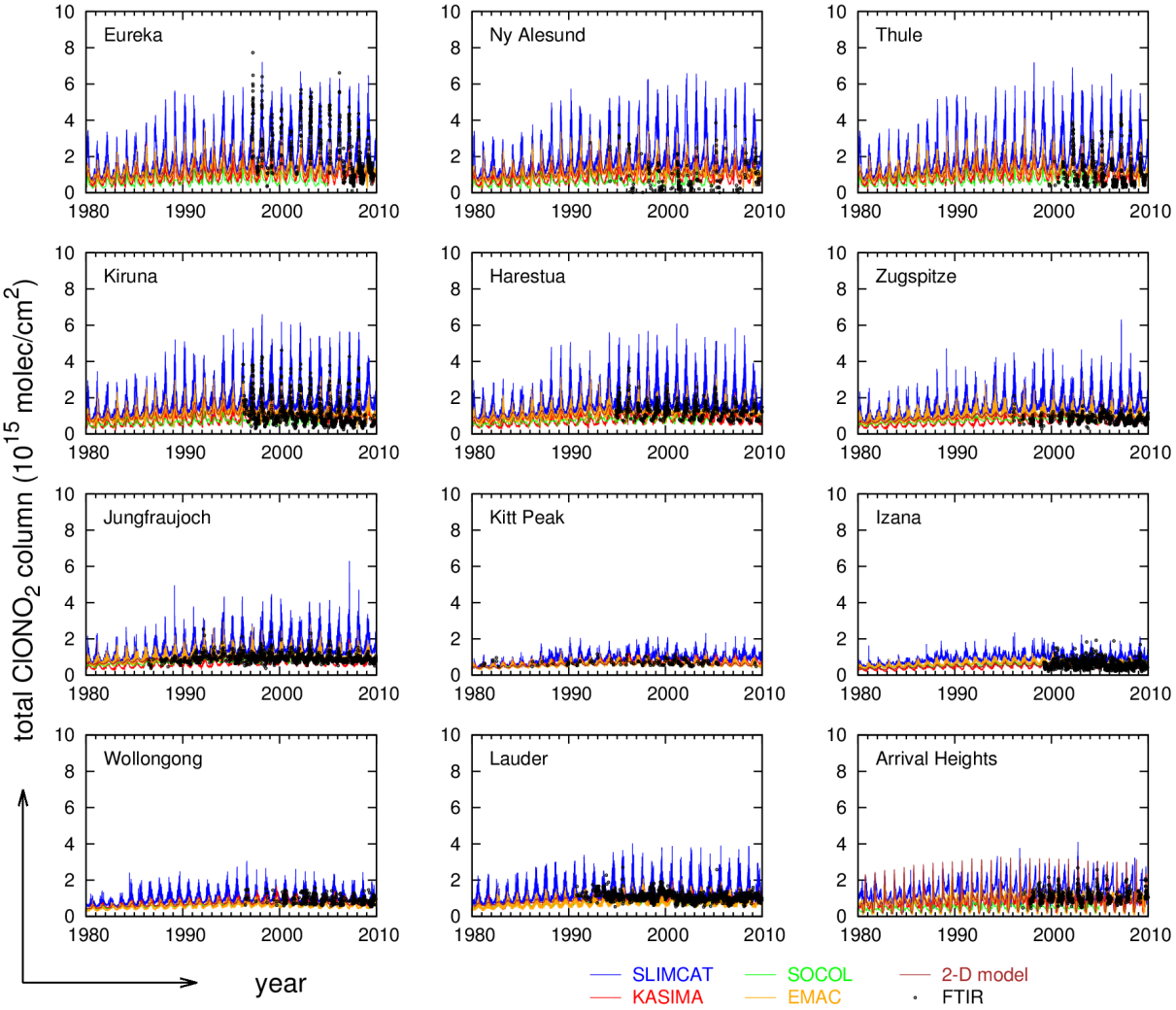

Figure 5.4: Time series of $ClONO_2$ total column abundances in molecules per cm^2 at the different sites as measured by FTIR (black dots) and simulated by SLIMCAT (blue line), KASIMA (red line), SOCOL (green line), EMAC (orange line), and Bremen 2-D model (brown line).

Table 5.3: Mean differences between models and FTIR measurements in % (calculated as (model-meas)/meas) averaged over all sites, and their standard deviations (σ), for HCl, $ClONO_2$, and HF. The differences for KASIMA and SLIMCAT were calculated from the daily values, while for EMAC, SOCOL, and the 2-D model, the monthly means were used. Significant differences (2 σ level) are printed in bold.

species	KASIMA	SLIMCAT	2-D model	EMAC	SOCOL
HCl	$\mathbf{-11.9 \pm 2.1}$	$\mathbf{+10.5 \pm 1.9}$	$\mathbf{+8.3 \pm 3.9}$	$\mathbf{-24.8 \pm 2.0}$	$\mathbf{+9.5 \pm 3.5}$
$ClONO_2$	$+11.6 \pm 14.1$	$\mathbf{+90.0 \pm 35.6}$	$+15.4 \pm 10.0$	$+30.1 \pm 22.0$	$\mathbf{-17.3 \pm 5.6}$
HF	$+1.8 \pm 2.5$	$\mathbf{+36.3 \pm 3.1}$	$\mathbf{-14.3 \pm 3.1}$		

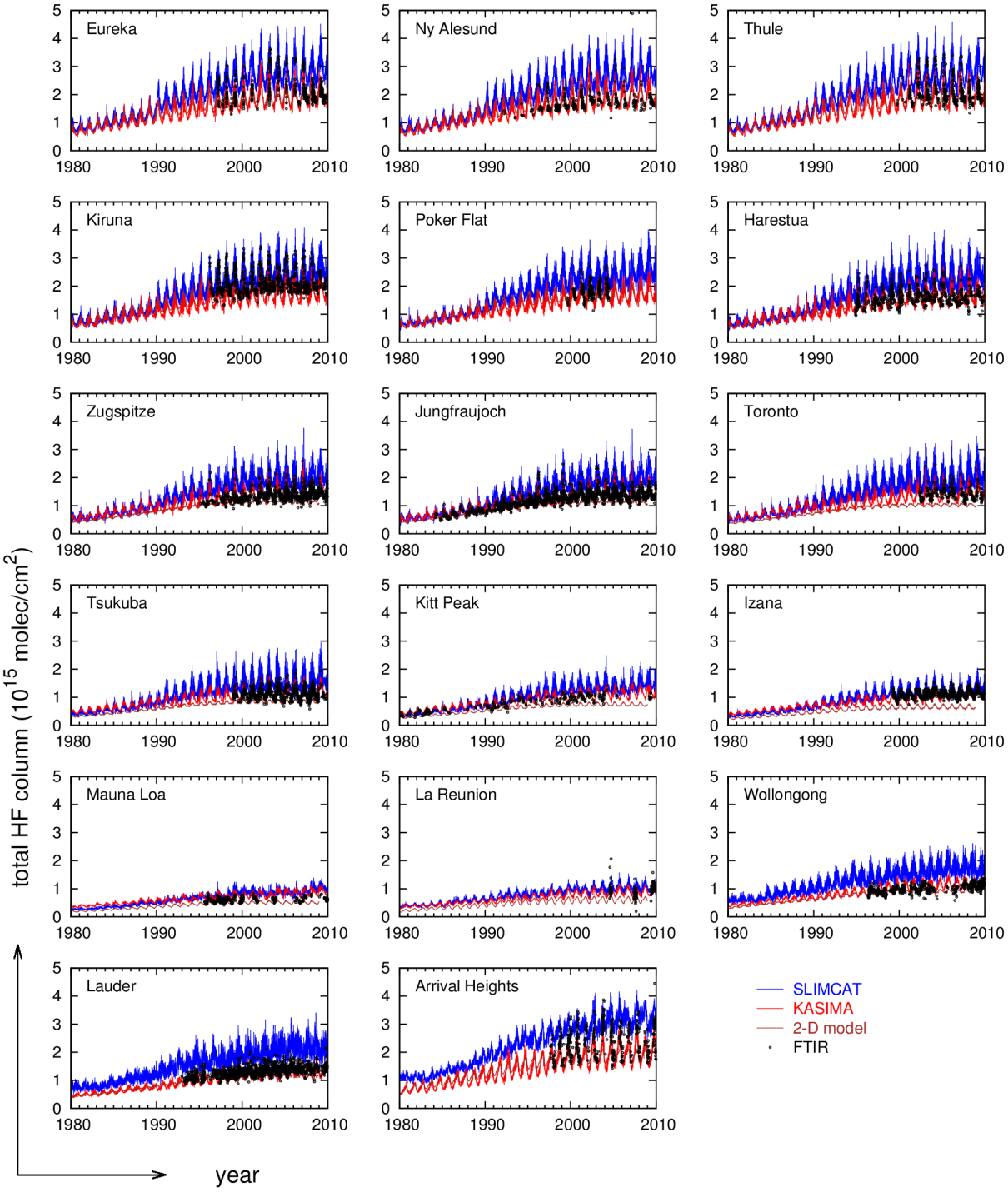

Figure 5.5: Time series of HF total column abundances in molecules per cm^2 at the different sites as measured by FTIR (black dots) and simulated by SLIMCAT (blue line), KASIMA (red line), and Bremen 2-D model (brown line).

when averaging over a longer time range and with respect to the mean seasonal cycle, they are expected to agree with them.

In the HCl time series, the models and measurements all show a steady increase until about the mid-1990s, followed by a stabilisation, and a decrease since then (Figure 5.3). The southern hemisphere is delayed by a few years with respect to the northern hemisphere. According to Table 5.3, overall, SLIMCAT, SOCOL, and the 2-D model tend to slightly overestimate the total HCl column abundances as measured by the FTIR spectrometers. EMAC and KASIMA significantly underestimate the FTIR values. Reasons for the relatively low KASIMA values have been discussed by e.g. Hamann (2007), Mikuteit (2008), and Kohlhepp et al. (2011). One of them is that KASIMA does not include the part of the troposphere below 7 km. In addition, some of the tropospheric processes must be parameterised, for example wash-out, because the model does not simulate cloud or rain droplets. Furthermore, it has been shown by Hamann (2007) that the HCl column abundances at polar latitudes become more realistic in KASIMA when increasing the resolution, for example from T21, which was used for the present simulation, to T42. This is due to a better representation of the polar vortex and especially also the processes at its edge if the resolution is higher.

As can already be seen in Table 5.1, measurements of $ClONO_2$ are only available at 12 of the 17 sites. The main reason for this is that $ClONO_2$ is not easy to measure with an FTIR spectrometer, especially at lower latitude sites, due to its weak spectral signature and the relatively low total column abundances at lower latitudes. The sites Tsukuba, Mauna Loa, Poker Flat, Toronto, and La Réunion are therefore not included in Figure 5.4. Analogously to HCl, the $ClONO_2$ time series show an increase until the end of the 1990s, and a decrease since then. Especially at the polar sites Ny Ålesund, Thule, and Kiruna, the models seem to overestimate the total column abundances, especially the annual minima. On average, SLIMCAT shows the largest positive deviation from the measurements (see Table 5.3), but also EMAC overestimates the FTIR measurements considerably.

The two CCMs EMAC and SOCOL do not simulate the atmospheric HF content, therefore only results of KASIMA, SLIMCAT, and the 2-D model can be compared with the FTIR measurements at the 17 sites (Figure 5.5). SLIMCAT tends to overestimate the HF total column abundance, while the KASIMA results on average agree very well with the FTIR measurements (see also Table 5.3). The 2-D model output is very similar to the KASIMA one, except for some low and midlatitude sites (e.g., Toronto, Kitt Peak, Izaña, and La Réunion), where it seems to underestimate the increase especially in the 1990s. This leads to a mean underestimation of the HF abundance by the 2-D model (Table 5.3).

Concluding from the comparison of the time series from models and measurements, we can state that the overall agreement on the temporal development is good. This is expected because the models use similar boundary conditions which include actual measurements. The results also agree with earlier studies from measurements mentioned above, e.g. those by Considine et al. (1999), Rinsland et al. (2003), Newchurch et al. (2003), Lary et al. (2007), and Zander et al. (2008). An absolute constant offset in the total column abundances as seen for example in the EMAC and KASIMA HCl or the SLIMCAT

HF results is not expected to have a significant influence on the trend calculations and comparisons performed in Section 5.3.

5.2.2 Seasonal cycle

From the model and measurement time series of the total column abundances, normalised mean monthly means have been calculated. This was done by first normalising the monthly means with the corresponding annual means, and then averaging over the time range 2000–2009, where available. The resulting seasonal cycles for HCl, $ClONO_2$, and HF are compared in Figures 5.6 to 5.8, respectively. A seasonal variation is expected for all three gases considered here, mainly due to the varying height of the tropopause. The stratospheric general circulation transports air from the summer to the winter hemisphere. This goes along with upwelling above the summer pole, and subsidence above the winter pole. That also means that the tropopause is higher in the summer hemisphere than in the winter hemisphere (see also Section 2.1). Because HCl, $ClONO_2$, and HF are produced mainly in the stratosphere, the largest contribution to the total column abundances stems from there. The lower the tropopause, the larger is the stratospheric fraction of a vertical column, and the smaller the tropospheric one. This leads to relatively high total column abundances of the three investigated gases at the end of winter. The HCl and $ClONO_2$ abundances above the winter pole also depend strongly on the location of the polar vortex, and on the degree of chlorine activation therein. In case of strong chlorine activation, the proportion of Cl, ClO, and Cl_2O_2 in Cl_y is much larger than usual, resulting in lower column abundances of the reservoir species HCl and $ClONO_2$ (see also Section 2.2). At the end of polar night, in the beginning of spring, when the polar vortex breaks up, most of the active chlorine is converted to the reservoir species HCl and $ClONO_2$ again. This results in strong peaks of the total column abundances of these gases. In the Arctic, normally, at first $ClONO_2$ is formed because the reaction producing it is faster than the one forming HCl (see Section 2.2), and a few weeks later, a slightly broader peak of HCl follows. In the Antarctic, this sequence is not very pronounced, but instead, both HCl and $ClONO_2$ recover at about the same time in spring. This is due to a usually stronger denitrification in the Antarctic than in the Arctic where the stratospheric polar vortex is more variable and not as stable, long-lasting and cold as the Antarctic polar vortex. Furthermore, this strong Antarctic vortex also leads to stronger ozone depletion at the end of the winter above the Antarctic than above the Arctic so that the production of ClO from Cl and O_3 is limited (reaction [2.9]), resulting in less production of $ClONO_2$ (reaction [2.12]).

According to the measurements, the annual maximum in HCl occurs in April and May in the Northern Hemisphere, and in October and November in the Southern Hemisphere (Figure 5.6). When compared to the FTIR results, the seasonal cycle simulated by the 2-D model is too weak at most sites. Both SLIMCAT and EMAC capture the time of maximum and minimum of the seasonal cycle very well at most sites. But the amplitude SLIMCAT calculates is slightly too large, especially at the polar sites. KASIMA and SOCOL simulate the maximum about one month too late at some of the sites.

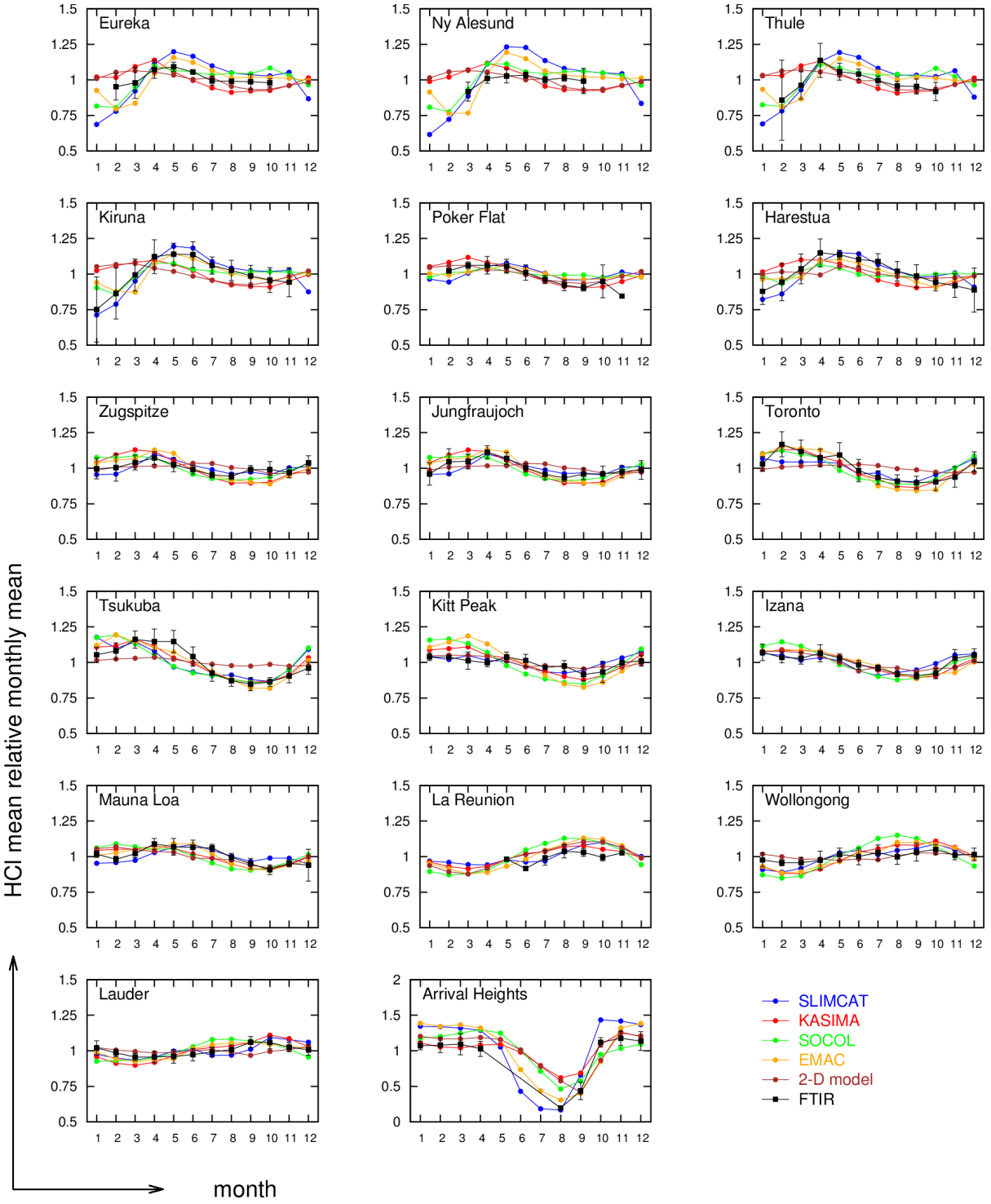

Figure 5.6: Annual cycle of HCl at the different sites as determined from the FTIR instruments (black) and simulated by SLIMCAT (blue), KASIMA (red), SOCOL (green), EMAC (orange), and the Bremen 2-D model (brown). The mean relative monthly means were calculated by normalising the monthly means with the respective annual mean and then averaging over the period 2000–2009. The error bars of the FTIR measurements represent the standard deviation of the distribution of the monthly means.

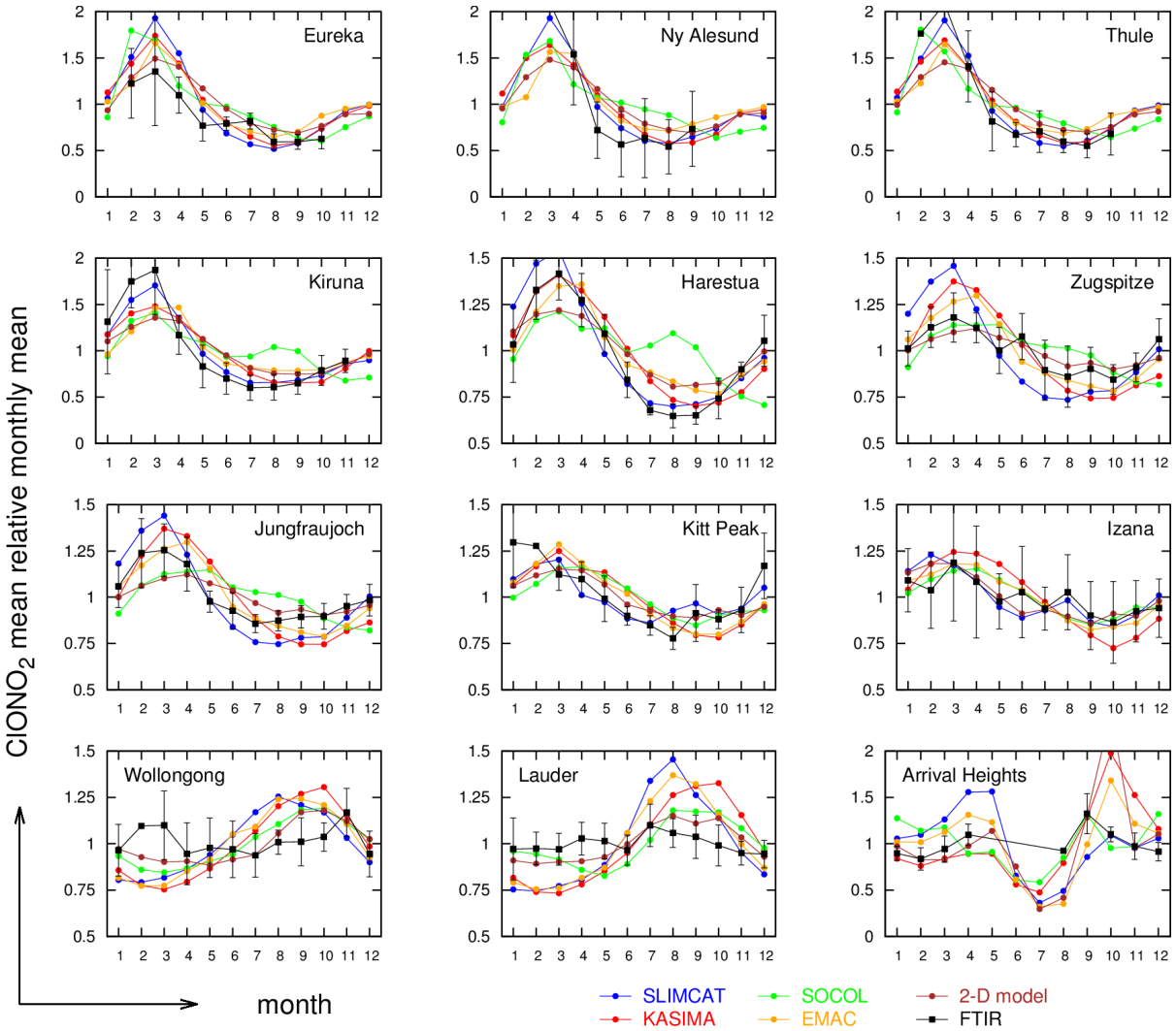

Figure 5.7: Annual cycle of $ClONO_2$ at the different sites as determined from the FTIR instruments (black) and simulated by SLIMCAT (blue), KASIMA (red), SOCOL (green), EMAC (orange), and the Bremen 2-D model (brown). The mean relative monthly means were calculated by normalising the monthly means with the respective annual mean and then averaging over the period 2000–2009. The error bars of the FTIR measurements represent the standard deviation of the distribution of the monthly means.

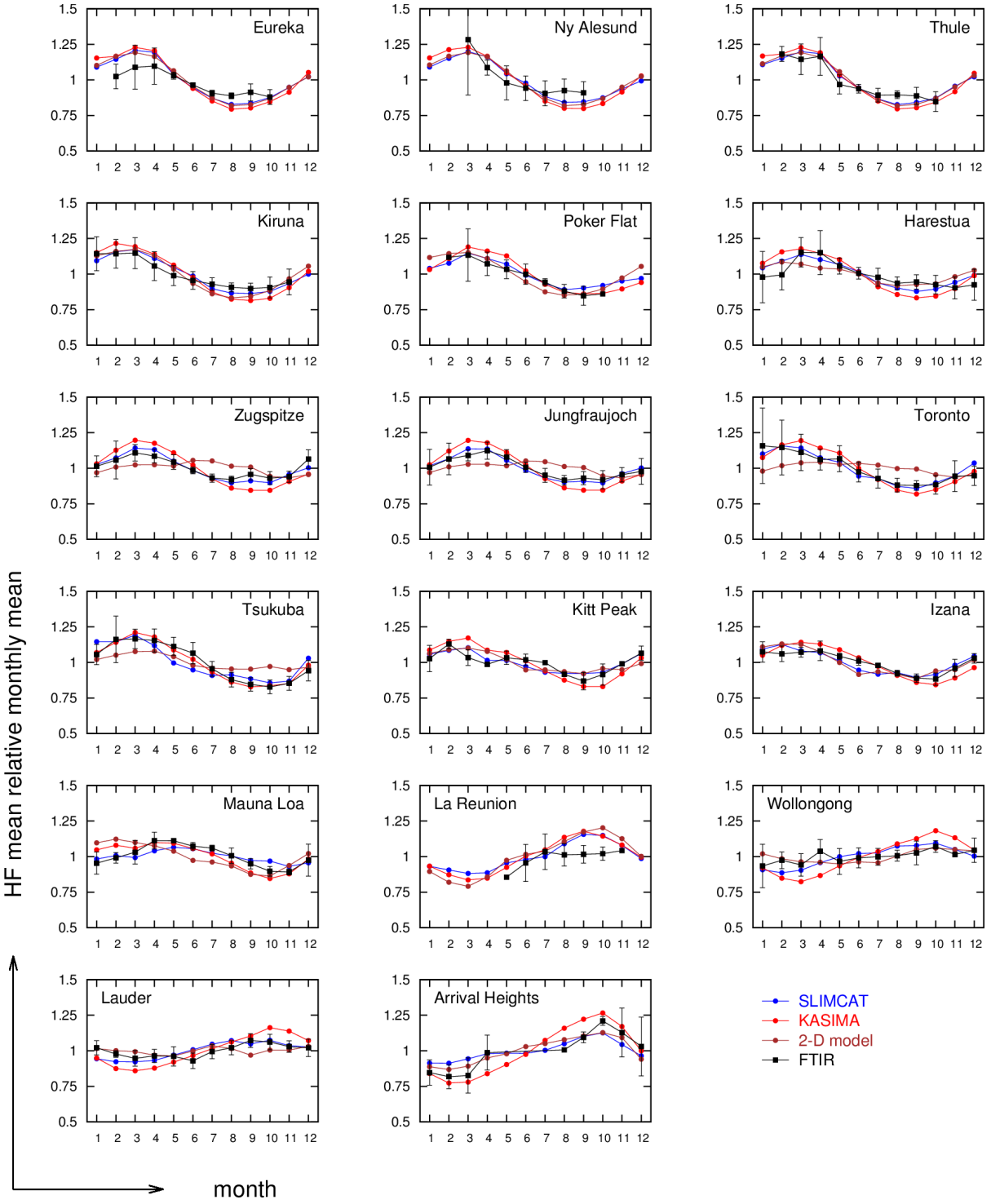

Figure 5.8: Annual cycle of HF at the different sites as determined from the FTIR instruments (black) and simulated by SLIMCAT (blue), KASIMA (red), and the Bremen 2-D model (brown). The mean relative monthly means were calculated by normalising the monthly means with the respective annual mean and then averaging over the period 2000–2009. The error bars of the FTIR measurements represent the standard deviation of the distribution of the monthly means.

Most models agree with the measurements on the $ClONO_2$ maximum in March in the Northern Hemisphere (Figure 5.7). Only EMAC tends to simulate it about one month too late. Among the models, SLIMCAT shows the largest amplitude of the seasonal cycle. It thereby overestimates the FTIR amplitude in the Northern Hemisphere midlatitudes, while in the higher latitudes, SLIMCAT tends to agree best with the measurements. In contrast, the other models underestimate the high latitude seasonal amplitude, but at midlatitudes agree better with the FTIR results than SLIMCAT does. In the Southern Hemisphere, the seasonal cycle expected by the models with a maximum between August and October is not very pronounced in the measurements.

The seasonal cycle of HF as measured by the FTIR instruments is captured very well by the two CTMs KASIMA and SLIMCAT. The annual maximum occurs around March in the Northern Hemisphere and in October in the Southern Hemisphere. The 2-D model underestimates the amplitude of the seasonal cycle at the mid and low latitude sites on both hemispheres.

As a conclusion from this analysis and comparison of the mean seasonal cycles from measurements and models, we can state that the overall agreement is good. At the Arctic sites, the time shift of the maximum in $ClONO_2$ and HCl described above is very nicely visible.

5.3 Trend results

In this section, the trends determined from the modelled and measured time series of HCl, $ClONO_2$, and HF described and discussed in the previous sections are presented. In addition to the linear trend, the fitting function (4.1) included a first- (for FTIR series from sites poleward of 70°) or third-order Fourier series in order to account for the seasonal cycle, as described in Section 4. This function is expected to yield the smallest root mean square differences and thus the smallest 95% confidence intervals within the methods discussed in Section 4.2.1. The time range considered for the comparison is 2000–2009 because all FTIR sites except Toronto and La Réunion performed measurements during this period (see Table 5.1). Furthermore, an approximately linear decrease between 2000 and 2009 is expected for the two chlorine species, while for HF, it is interesting to determine whether the more or less linear increase assumed by the model scenarios (see Figure 5.2) can be seen in the measurements, too.

For the trend determination, all model data that were available were used, i.e., from EMAC, KASIMA, and SLIMCAT one value per day, from the 2-D model one every fifth day and from SOCOL the monthly means. When comparing these model trends to those from the measurements, the irregular sampling and the gaps in some of the FTIR time series must be kept in mind. In addition to sampling, also the type of fitting function, the time of year chosen, time series length, and longer-scale variations with time may affect the trends and/or their confidence intervals, as discussed in Section 4.2. As already mentioned, the SOCOL time series end in 2004 so that the SOCOL trend results should not be compared quantitatively to those from the other data sets, although they may qualitatively agree with them.

The measurements and models agree on a decrease of HCl by about 1%/yr (Figure 5.9 and Table 5.4). On average, the FTIR measurements seem to indicate a slightly stronger decrease of HCl in the northern

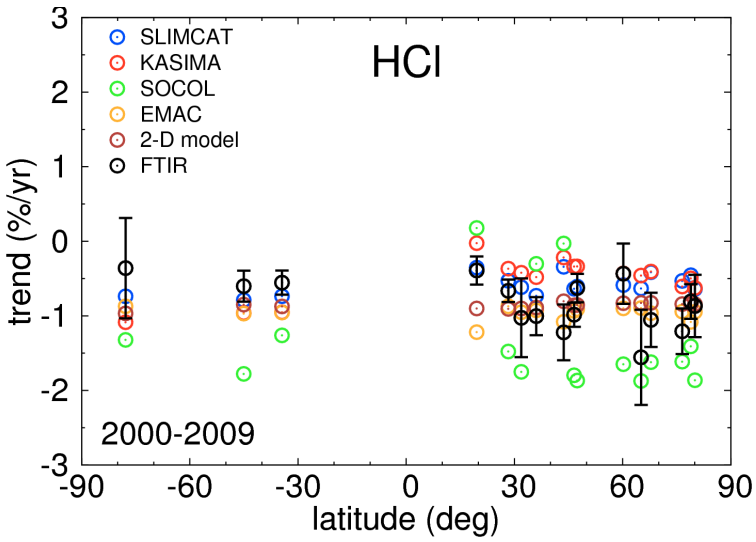

Figure 5.9: Comparison of the HCl trends from the FTIR measurements (black) between 2000 and 2009 (in % per year) with those modelled by SLIMCAT (blue), KASIMA (red), SOCOL (green), EMAC (orange), and the Bremen 2-D model (brown). In order not to overload the picture, the bootstrap error bars for the modelled trends are not shown, only those for the measurements.

hemisphere than in the southern hemisphere. In contrast, most of the models do not simulate a distinguishable difference between the hemispheres, except for KASIMA, but its signal is opposite to the FTIR one, with slightly stronger decreases in the southern hemisphere. This disagreement on the hemispheric difference results in an underestimation of the FTIR trends by all models except SOCOL at nearly all sites in the northern hemisphere, and an overestimation in the southern hemisphere. The FTIR trend at the southernmost Northern Hemispheric site, Mauna Loa, is weaker than at most sites in the northern hemisphere mid and high latitudes. This tendency towards weaker decreases in the northern hemisphere low latitudes is also simulated by KASIMA and SLIMCAT, and possibly also by SOCOL, but its results are difficult to interpret. EMAC shows the opposite signal, and the 2-D model none.

The $ClONO_2$ trends from models and measurements show a larger spread than those of HCl, but overall, they agree on a decrease of roughly around 1.5 to 2%/yr (Figure 5.10 and Table 5.5). So $ClONO_2$ at most sites decreases faster than HCl. More discussion on this topic can be found in Chapter 6. The FTIR trends of $ClONO_2$ show a strong dependency on latitude, especially in the northern hemisphere, with stronger trends in the low and high latitudes than in midlatitudes. When interpreting this, the large error bar must be kept in mind. In addition, the $ClONO_2$ trend at Eureka may be significantly biased by the use of different spectroscopic data. More information on this effect can be found in Fast et al. (2011), Lindenmaier et al. (2012), or in the Eureka site description by Kohlhepp et al. (2012). However, the signal of a stronger decrease when approaching the north pole can also be found in all the models except the 2-D one. In the southern hemisphere, the decrease seen in the FTIR measurements becomes weaker towards the pole, and the Arrival Heights measurements even show an increase of $ClONO_2$. However, this site

Table 5.4: HCl trend in % per year between 2000 and 2009, calculated by fitting a linear function combined with a first (sites poleward of 70°) or third order Fourier series to the data. The error bars were determined with the bootstrap method. Significant trends are printed in bold.

Measurement site	FTIR	KASIMA	SLIMCAT	2-D model	EMAC	SOCOL
Eureka	**−0.87 ± 0.42**	**−0.63 ± 0.09**	**−0.64 ± 0.15**	**−0.84 ± 0.03**	**−0.95 ± 0.12**	**−1.86 ± 0.82**
Ny Ålesund	**−0.81 ± 0.23**	**−0.50 ± 0.10**	**−0.46 ± 0.15**	**−0.84 ± 0.03**	**−1.08 ± 0.12**	**−1.41 ± 0.96**
Thule	**−1.21 ± 0.31**	**−0.61 ± 0.09**	**−0.53 ± 0.15**	**−0.84 ± 0.03**	**−0.94 ± 0.12**	**−1.61 ± 0.85**
Kiruna	**−1.05 ± 0.36**	**−0.41 ± 0.10**	**−0.42 ± 0.16**	**−0.83 ± 0.02**	**−0.96 ± 0.12**	**−1.62 ± 0.86**
Poker Flat	**−1.56 ± 0.64**	**−0.46 ± 0.09**	**−0.63 ± 0.11**	**−0.83 ± 0.02**	**−0.90 ± 0.09**	**−1.87 ± 0.60**
Harestua	**−0.44 ± 0.40**	**−0.43 ± 0.10**	**−0.59 ± 0.15**	**−0.83 ± 0.03**	**−0.90 ± 0.10**	**−1.65 ± 0.73**
Zugspitze	**−0.63 ± 0.19**	**−0.34 ± 0.08**	**−0.61 ± 0.13**	**−0.85 ± 0.02**	**−0.91 ± 0.09**	**−1.87 ± 0.56**
Jungfraujoch	**−0.98 ± 0.16**	**−0.34 ± 0.07**	**−0.64 ± 0.12**	**−0.86 ± 0.02**	**−0.93 ± 0.09**	**−1.80 ± 0.56**
Toronto	**−1.22 ± 0.37**	**−0.22 ± 0.11**	**−0.34 ± 0.19**	**−0.80 ± 0.02**	**−1.08 ± 0.15**	−0.03 ± 1.44
Tsukuba	**−1.00 ± 0.25**	**−0.48 ± 0.07**	**−0.73 ± 0.16**	**−0.89 ± 0.02**	**−0.93 ± 0.10**	−0.30 ± 0.56
Kitt Peak	**−1.03 ± 0.53**	**−0.42 ± 0.06**	**−0.62 ± 0.12**	**−0.90 ± 0.03**	**−0.95 ± 0.09**	**−1.75 ± 0.38**
Izaña	**−0.66 ± 0.15**	**−0.37 ± 0.06**	**−0.53 ± 0.12**	**−0.91 ± 0.04**	**−0.87 ± 0.08**	**−1.48 ± 0.39**
Mauna Loa	**−0.39 ± 0.19**	−0.03 ± 0.05	**−0.35 ± 0.11**	**−0.90 ± 0.03**	**−1.22 ± 0.06**	0.18 ± 0.72
Wollongong	**−0.55 ± 0.16**	**−0.95 ± 0.05**	**−0.74 ± 0.13**	**−0.87 ± 0.02**	**−0.96 ± 0.09**	**−1.26 ± 0.50**
Lauder	**−0.60 ± 0.21**	**−0.96 ± 0.07**	**−0.79 ± 0.12**	**−0.85 ± 0.02**	**−0.97 ± 0.09**	**−1.78 ± 0.67**
Arrival Heights	−0.36 ± 0.67	**−1.09 ± 0.08**	**−0.74 ± 0.13**	**−0.97 ± 0.15**	**−0.87 ± 0.09**	**−1.32 ± 1.26**

Table 5.5: $ClONO_2$ trend in % per year between 2000 and 2009, calculated by fitting a linear function combined with a first (sites poleward of 70°) or third order Fourier series to the data. The error bars were determined with the bootstrap method. Significant trends are printed in bold.

Measurement site	FTIR	KASIMA	SLIMCAT	2-D model	EMAC	SOCOL
Eureka	**−4.56 ± 0.78**	**−1.18 ± 0.19**	**−0.83 ± 0.25**	**−1.21 ± 0.10**	**−1.75 ± 0.16**	**−3.37 ± 2.87**
Ny Ålesund	**6.79 ± 5.01**	**−1.03 ± 0.20**	**−0.62 ± 0.26**	**−1.20 ± 0.08**	**−1.59 ± 0.17**	−1.84 ± 3.07
Thule	**−3.58 ± 1.04**	**−1.28 ± 0.18**	**−0.94 ± 0.25**	**−1.20 ± 0.07**	**−1.77 ± 0.16**	**−3.37 ± 2.46**
Kiruna	**−1.45 ± 0.95**	**−0.91 ± 0.16**	**−0.71 ± 0.24**	**−1.19 ± 0.04**	**−1.05 ± 0.17**	−1.62 ± 2.36
Harestua	−0.07 ± 0.52	**−1.05 ± 0.14**	**−0.80 ± 0.21**	**−1.21 ± 0.03**	**−1.01 ± 0.16**	**−2.73 ± 1.58**
Zugspitze	**−1.37 ± 0.52**	**−0.90 ± 0.12**	−0.02 ± 0.24	**−1.24 ± 0.05**	**−1.16 ± 0.15**	**−3.42 ± 0.62**
Jungfraujoch	**−1.44 ± 0.33**	**−0.90 ± 0.12**	−0.06 ± 0.22	**−1.25 ± 0.05**	**−1.16 ± 0.15**	**−3.30 ± 0.61**
Kitt Peak	**−2.53 ± 1.16**	**−0.86 ± 0.08**	**−0.21 ± 0.18**	**−1.31 ± 0.05**	**−1.14 ± 0.12**	**−2.89 ± 0.67**
Izaña	**−2.86 ± 0.67**	**−0.72 ± 0.10**	**0.19 ± 0.16**	**−1.33 ± 0.08**	**−1.14 ± 0.10**	**−2.14 ± 0.66**
Wollongong	**−2.18 ± 0.60**	**−1.47 ± 0.07**	**−0.96 ± 0.16**	**−1.25 ± 0.04**	**−1.54 ± 0.11**	**−1.46 ± 0.92**
Lauder	−0.35 ± 0.46	**−1.61 ± 0.09**	**−0.59 ± 0.20**	**−1.22 ± 0.05**	**−1.18 ± 0.16**	**−2.21 ± 0.74**
Arrival Heights	**0.99 ± 0.76**	**−1.65 ± 0.20**	**−1.11 ± 0.26**	**−0.84 ± 0.82**	**−0.52 ± 0.23**	−1.54 ± 3.71

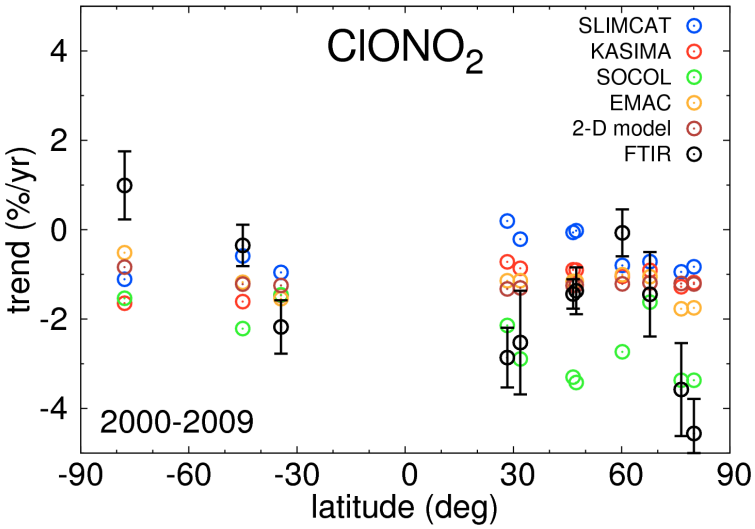

Figure 5.10: Like Figure 5.9, but for $ClONO_2$.

may also suffer from biases, in this case because of sampling, in combination with the large seasonal cycle. In contrast, most models do not show a clear signal, which leads to a mean underestimation of the decrease at Wollongong and an overestimation at the two other sites. Only EMAC shows a behaviour similar to that of the measurements, with the smallest decrease at Arrival Heights.

At most sites, the CTMs KASIMA and SLIMCAT agree with the measurements on an increase of HF during the time range 2000–2009 with around 1%/yr, while the 2-D model only shows a very weak increase (Figure 5.11 and Table 5.6). In the northern hemisphere, both models and measurements show

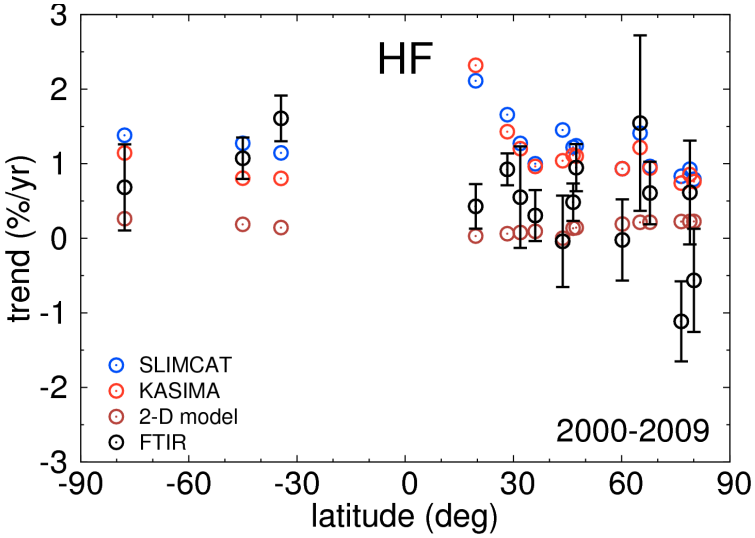

Figure 5.11: Like Figure 5.9, but for HF.

Table 5.6: HF trend in % per year between 2000 and 2009, calculated by fitting a linear function combined with a first (sites poleward of 70°) or third order Fourier series to the data. The error bars were determined with the bootstrap method. Significant trends are printed in bold.

Measurement site	FTIR	KASIMA	SLIMCAT	2-D model
Eureka	-0.56 ± 0.69	$\mathbf{0.76 \pm 0.11}$	$\mathbf{0.79 \pm 0.11}$	$\mathbf{0.23 \pm 0.03}$
Ny Ålesund	0.61 ± 0.70	$\mathbf{0.85 \pm 0.10}$	$\mathbf{0.93 \pm 0.11}$	$\mathbf{0.23 \pm 0.03}$
Thule	$\mathbf{-1.11 \pm 0.54}$	$\mathbf{0.74 \pm 0.11}$	$\mathbf{0.83 \pm 0.11}$	$\mathbf{0.22 \pm 0.03}$
Kiruna	$\mathbf{0.61 \pm 0.42}$	$\mathbf{0.94 \pm 0.12}$	$\mathbf{0.96 \pm 0.15}$	$\mathbf{0.22 \pm 0.04}$
Poker Flat	$\mathbf{1.54 \pm 1.18}$	$\mathbf{1.22 \pm 0.11}$	$\mathbf{1.41 \pm 0.15}$	$\mathbf{0.21 \pm 0.04}$
Harestua	-0.02 ± 0.54	$\mathbf{0.93 \pm 0.12}$	$\mathbf{0.93 \pm 0.16}$	$\mathbf{0.19 \pm 0.03}$
Zugspitze	$\mathbf{0.95 \pm 0.32}$	$\mathbf{1.10 \pm 0.10}$	$\mathbf{1.24 \pm 0.16}$	$\mathbf{0.14 \pm 0.05}$
Jungfraujoch	$\mathbf{0.48 \pm 0.25}$	$\mathbf{1.11 \pm 0.10}$	$\mathbf{1.22 \pm 0.15}$	$\mathbf{0.14 \pm 0.05}$
Toronto	-0.04 ± 0.61	1.04 ± 0.14	1.45 ± 0.25	0.00 ± 0.05
Tsukuba	0.31 ± 0.34	$\mathbf{0.96 \pm 0.08}$	$\mathbf{1.00 \pm 0.19}$	$\mathbf{0.09 \pm 0.04}$
Kitt Peak	0.55 ± 0.68	$\mathbf{1.20 \pm 0.07}$	$\mathbf{1.27 \pm 0.15}$	$\mathbf{0.08 \pm 0.04}$
Izaña	$\mathbf{0.92 \pm 0.21}$	$\mathbf{1.43 \pm 0.07}$	$\mathbf{1.66 \pm 0.15}$	0.06 ± 0.06
Mauna Loa	$\mathbf{0.43 \pm 0.30}$	$\mathbf{2.32 \pm 0.09}$	$\mathbf{2.11 \pm 0.15}$	0.03 ± 0.05
Wollongong	$\mathbf{1.61 \pm 0.31}$	$\mathbf{0.80 \pm 0.07}$	$\mathbf{1.15 \pm 0.15}$	$\mathbf{0.14 \pm 0.04}$
Lauder	$\mathbf{1.07 \pm 0.28}$	$\mathbf{0.81 \pm 0.08}$	$\mathbf{1.27 \pm 0.15}$	$\mathbf{0.19 \pm 0.04}$
Arrival Heights	$\mathbf{0.68 \pm 0.58}$	$\mathbf{1.14 \pm 0.10}$	$\mathbf{1.38 \pm 0.09}$	$\mathbf{0.26 \pm 0.04}$

the tendency of weaker increases when approaching the pole. Some FTIR trends are even negative, but most of them not significantly, except for Thule.

In the following Section (5.4), the trend results from models and measurements presented here are discussed in more detail.

5.4 Discussion and conclusions

In the following discussion on the trend results, the findings of Section 4.2 should be kept in mind, where the influence of the choice of fitting function, time of year, time series length, the time period, and of sampling is investigated. In addition, multi-annual variations with time may be present in the time series and affect the calculated trend. Besides, it must be remembered that not all trends are exactly comparable with each other. As mentioned before, the time series of SOCOL end in 2004 and those of the 2-D model in 2008, and measurements at Poker Flat are also only available until 2004. The Toronto FTIR series were included in the 2000–2009 trend calculations although measurements at this site started in 2002 only.

Overall, there is good agreement of the results shown in Section 5.3 (and published by Kohlhepp et al., 2012) with earlier investigations of HCl, $ClONO_2$, and HF. The measured and modelled trends obtained in this work amount to around -1 and -2%/yr for HCl and $ClONO_2$, respectively, and to around +1%/yr for HF. This corresponds well to the trend of (-0.78±0.08)%/yr for HCl between 50 and 65 km height and 60°S and 60°N calculated by Froidevaux et al. (2006) from measurements by the MLS (Microwave Limb Sounder) instrument on the Aura satellite between August 2004 and January 2006. A significantly

negative trend of about -5.1%/decade to -5.8%/decade for 1997–2008 was found by Jones et al. (2011) from a HCl time series created by combining HALOE (Halogen Occultation Experiment) data with ACE-FTS (Atmospheric Chemistry Experiment Fourier Transform Spectrometer) results between 35 and 45 km. Measurements with the McMath-Pierce solar telescope on Kitt Peak (Arizona, U.S.) suggest a slightly larger decrease of the HCl total column abundance of (-1.8±0.4)%/yr between 1997 and 2007 (Wallace and Livingston, 2007).

From tropospheric measurements of ozone-depleting substances, the EESC (Equivalent Effective Stratospheric Chlorine) abundance can be assessed (Newman et al., 2007). Thereby, the time necessary to transport the chlorine- and bromine-containing source gases from the troposphere to the stratosphere is accounted for, as well as the dependency of the fractional release rates on the mean age-of-air. The midlatitude EESC abundance was estimated by the WMO (2011) to have decreased by 11% between the peak in 1997 and 2008, corresponding to a trend of about -1%/yr. Above Antarctica, the peak of EESC occurred later, around 2002. Until 2008, the EESC abundance decreased by about 5% there (WMO, 2011) which corresponds to a trend of -0.8%/yr (WMO, 2011). This later EESC peak agrees very well with the FTIR trend results presented here that show a slightly weaker decrease of HCl in the southern than in the northern hemisphere. The models do not reproduce this hemispheric dependency. However, the EMAC results indicate weaker decreases especially for $ClONO_2$, but also slightly for HCl, when approaching the south pole.

Part of the difference between the modelled trends can be explained by the different halocarbon scenarios used (see Section 5.1.2 and Figure 5.2). Considering a time shift due to transport from the troposphere to the stratosphere, the weakest stratospheric inorganic chlorine decrease is expected to result from the WMO (2007) Ref 2 scenario used by KASIMA and the 2-D model. Indeed, KASIMA shows the smallest trend values, along with SLIMCAT (Figs. 5.9 and 5.10 and Tabs. 5.4 and 5.5). But, interestingly, the 2-D model simulates a stronger decrease of HCl and $ClONO_2$ than would be expected from the WMO (2007) Ref 2 scenario. Also EMAC and SOCOL show stronger decreases than their surface scenario suggests. The difference in the HF trends of the CTMs and the 2-D model cannot be explained by different scenarios because as already mentioned, KASIMA and the 2-D model used the same one. A reason for part of the discrepancy is very likely the fact that the 2-D model does not treat all halogen-containing species explicitly. Specifically, HCFC-141b is not treated explicitly, but proportionately added to CH_3CCl_3, and the CFC-114, CFC-115, and HCFC-142b surface mixing ratios are considered in the HCFC-22 value. However, this is done proportionately to the number of chlorine atoms, and consequently the number of fluorine atoms is not exactly correct. At the beginning of the considered time range, the fluorine surface mixing ratio in the 2-D model is very roughly about 50 pptv too small. This missing fluorine abundance increases with time, which leads to a slightly too small HF increase in the 2-D model simulation.

For all three investigated gases, the measurements show different temporal evolutions in the two hemispheres that are not reproduced by the models. According to the FTIR results, the two chlorine species decrease stronger in the northern than in the southern hemisphere. The only model with a weak hemi-

spheric dependency of these trends is KASIMA, but the signal is opposite to the FTIR one. In the HF measurements, the increase is stronger in the southern than in the northern hemisphere. A possible reason for these hemispheric differences is that the major fraction of the chlorine and fluorine source gases was and is emitted in the northern hemisphere. Consequently, as already described above for EESC, there is a slight time shift of a few years in the temporal evolution of HCl, $ClONO_2$, and HF between the two hemispheres, resulting from the time needed for the transport from the northern to the southern hemisphere. In the southern hemisphere time series for 2000–2009, part of the chlorine plateau is therefore included. This leads to a weaker overall trend result than in the northern hemisphere, where the peak occurred before the year 2000. Concerning HF, a leveling-off in the total column abundances above Jungfraujoch around 2003–2004 has been reported already by Zander et al. (2008). In the present work, this finding can be confirmed with the FTIR trend results between 2000 and 2009 which do not significantly differ from zero at some other northern hemisphere sites, for example Ny Ålesund, Toronto (where the time range is 2002–2009), Tsukuba, and Kitt Peak (Figure 5.11). In addition, the 2004–2009 trends from the FTIR measurements at even more northern hemisphere sites are zero or even negative (Figure 4.1). However, as already mentioned, a 6-year period is certainly too short to determine reliable trends in this context. In contrast to the northern hemisphere results, the 2000–2009 and 2004–2009 trends of HF in the southern hemisphere all show relatively stronger increases. Analogously to the argumentation for chlorine, this may be due to a slight time shift between northern and southern hemisphere also in the stabilisation of the fluorine abundance, resulting from the transport from the northern to the southern hemisphere.

Another very interesting phenomenon found in the measurement and model data analysed here is a difference between the trends of HCl and $ClONO_2$. It has been described before e.g. by Mikuteit (2008) and Kohlhepp et al. (2011) for FTIR total column abundances above Kiruna or in the SPARC-CCMVal (2010) report for the Jungfraujoch. The normalised decrease of HCl appears to be weaker than that of $ClONO_2$ at most of the sites. In the FTIR trends, a latitudinal dependency of this discrepancy can be found in the northern hemisphere, with a larger difference in the high and low latitudes, and only slightly stronger decreases of $ClONO_2$ than of HCl in the midlatitudes (Figs. 5.9 and 5.10). The two CCMs EMAC and SOCOL also show larger differences in the high than in midlatitudes, and to a certain degree also SLIMCAT does. In the other two models, the difference does not exhibit a latitudinal dependency, but the decrease of $ClONO_2$ is slightly stronger than the HCl one at all sites. In the southern hemisphere, the Arrival Heights FTIR time series of $ClONO_2$ may have a sampling problem and is therefore not interpreted here. But the measurements at the two remaining sites show a similar signal as those in the northern hemisphere do, with a larger difference at the lower latitude site Wollongong than in the midlatitudes, at Lauder, where there is actually no difference within the error bars. In the following chapter (6), a more detailed discussion of this problem is provided, along with the description of sensitivity studies performed with the EMAC model in order to find the explanation for this difference.

6 On the difference between the trends of HCl and $ClONO_2$

A very interesting phenomenon that could be seen in the results from models and measurements presented in the previous chapter (5) but that had also been reported earlier for the FTIR measurements at Kiruna (by, e.g., Mikuteit, 2008; Kohlhepp et al., 2011) is a difference in the strengths of the HCl and $ClONO_2$ trends. From the decrease in chlorine source gases due to the Montreal Protocol, the two species would be expected to decrease at about the same rate. However, both models and measurements indicate a stronger decrease of $ClONO_2$ than of HCl. The reason for this is investigated in the present chapter. A direct comparison of the HCl and $ClONO_2$ trends from the previous chapter is presented in Section 6.1, and a possible explanation for the difference is discussed in Section 6.2. This theory is investigated by sensitivity studies with the EMAC model in Section 6.3, and conclusions are drawn in Section 6.4. The last part of this chapter (Section 6.5) discusses the FTIR data from Kiruna and Jungfraujoch with respect to the findings of the previous sections.

6.1 Evidence from FTIR measurements and model results

This section shortly discusses some results which were already presented in the previous chapter, i.e., trends of HCl and $ClONO_2$ as derived from FTIR measurements at 11 NDACC sites and from model results interpolated to these locations are shown. A detailed description of the data sets can be found in Section 5.1. For a better overview on the difference between the HCl and $ClONO_2$ trends, a direct comparison of these results is provided in Figure 6.1 for the FTIR data and the two time periods 1996–2009 and 2000–2009, and in Figure 6.2 for the model simulations by KASIMA and EMAC, for 2000–2009. The trends were determined by fitting a linear function and a Fourier series to daily data (with gaps in between in case of the FTIR measurements), and the error bars were estimated with the bootstrap method (for a more detailed description of the trend determination method please see Chapter 4).

For the time range 1996–2009, FTIR measurements are available from only 7 NDACC sites (Figure 6.1). Out of these 7 sites, 4 show a larger $ClONO_2$ than HCl decrease. According to the bootstrap error bars, the difference is significant at 3 of these sites. At the two northern hemisphere midlatitude sites Jungfraujoch and Zugspitze, the trends of the two chlorine species are approximately similar. The $ClONO_2$ trend is weaker than the HCl trend only at Harestua, but the difference is not significant. Ny Ålesund is not included in Figures 6.1 and 6.2 as we do not trust the resulting $ClONO_2$ trend because of the large variability in the time series, resulting from the strong seasonal cycle and irregular sampling due to the weather conditions, in combination with the long gap due to polar night. Also the Arrival Heights FTIR time series may be biased, as mentioned before. For the time range 2000–2009, measurements at

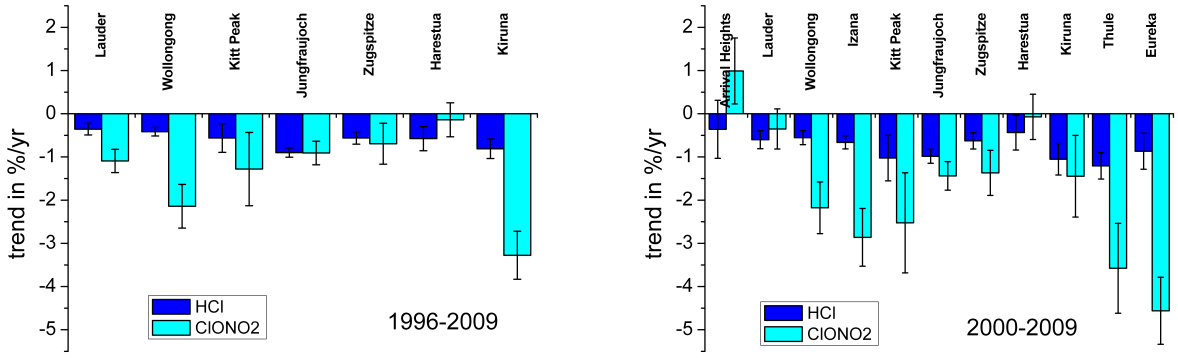

Figure 6.1: Comparison of HCl and $ClONO_2$ trends from FTIR measurements between 1996 and 2009 (left) at 7 NDACC FTIR sites and between 2000 and 2009 (right) at 11 sites, ordered from south to north. The trends were calculated by fitting a linear function combined with a first (at the sites poleward of 70°: Arrival Heights, Eureka, Thule) or third order Fourier series to the daily means. The errors were determined with the bootstrap method.

11 sites are available (Figure 6.1). At 8 of them, the $ClONO_2$ decrease is stronger than the HCl one, at 6 of these sites even significantly. Both Lauder and Harestua show a non-significantly (according to the bootstrap method) stronger decrease of HCl, while at Arrival Heights, $ClONO_2$ increases. This also may be a sampling bias, but interestingly, the signal shown by the EMAC model is similar, with a stronger trend of HCl at this site (see text below and Figure 6.2).

As an example, the trends of the two chlorine species from two of the model simulations are presented and compared in Figure 6.2. The KASIMA model simulates a significantly stronger decrease of $ClONO_2$ than of HCl at all sites. The strongest decreases of both gases occur in the northern hemisphere high latitudes and in the southern hemisphere, but the difference does not show a pronounced latitudinal dependency. In contrast, the difference between the $ClONO_2$ and HCl trends in the EMAC simulation depends on latitude: The $ClONO_2$ trend is significantly larger than the HCl one only at the high northern hemisphere sites Eureka and Thule and at the lower latitude sites Wollongong and Izaña. At the mid-latitude sites, $ClONO_2$ also decreases faster than HCl, but not significantly. Interestingly, the behaviour of EMAC at Arrival Heights also differs from the other sites, like for the FTIR results, with a stronger decrease of HCl in this case.

Concluding from this direct comparison of the $ClONO_2$ and HCl trends between 1996 and 2009 and 2000 and 2009, we can state that there is a pronounced or even significant difference between them in the measurements at many of the FTIR sites. Furthermore, the KASIMA model shows a stronger decrease of $ClONO_2$ than of HCl for all sites between 2000 and 2009. The EMAC model even seems to reproduce the latitudinal dependency of this difference seen in the FTIR measurements, with a stronger difference in the high and low latitudes than in the midlatitudes. This indicates that the models may

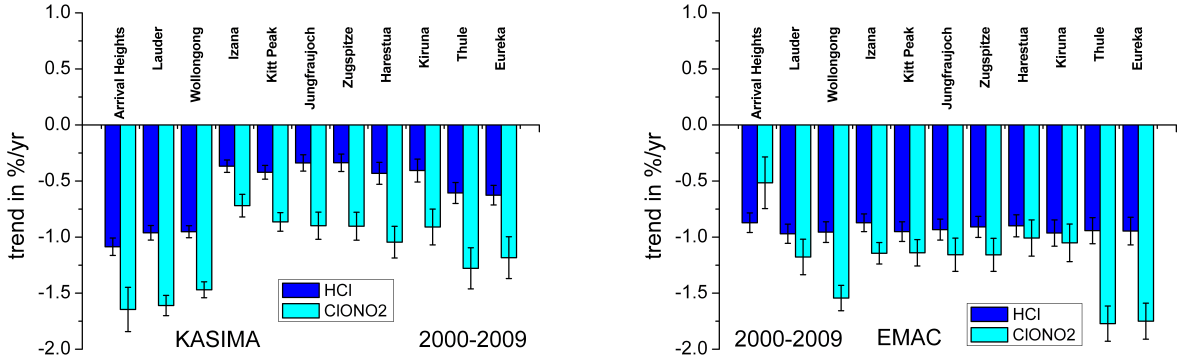

Figure 6.2: Comparison of HCl and $ClONO_2$ trends from KASIMA (left) and EMAC (right) between 2000 and 2009 at 11 NDACC sites, ordered from south to north. The trends were calculated by fitting a linear function combined with a third order Fourier series to the daily means. The errors were determined with the bootstrap method.

include the mechanism responsible for the differing trends which should therefore be understandable with sensitivity studies.

6.2 Coupling of the chlorine reservoir species with methane and nitrous oxide

As already described in Section 2.2, chlorine is released in the stratosphere from organic source gases (e.g., CFCs, HCFCs, and halons) mainly by photolysis and reaction with atomic oxygen ($O(^1D)$) and, to a lesser extent, with the hydroxyl radical (OH). These freed chlorine atoms then mostly react either with methane (CH_4) or ozone (O_3), forming HCl or chlorine monoxide (ClO), respectively:

$$Cl + CH_4 \rightarrow HCl + CH_3 \qquad [2.11]$$

$$Cl + O_3 \rightarrow ClO + O_2 \qquad [2.9]$$

The ClO produced by reaction [2.9] may react with nitrogen dioxide (NO_2) forming $ClONO_2$:

$$ClO + NO_2 + M \rightarrow ClONO_2 + M \qquad [2.12]$$

So, obviously, the most important other gases involved in the partitioning of chlorine between the two reservoir species HCl and $ClONO_2$ are CH_4, O_3, and NO_2. The main source of stratospheric NO_y is nitrous oxide (N_2O) (Legrand et al., 1989) via the reaction

$$N_2O + O(^1D) \rightarrow 2NO \qquad [6.1]$$

The nitric oxide (NO) produced there may react with O_3 forming NO_2:

$$NO + O_3 \rightarrow NO_2 + O_2 \qquad [2.5]$$

This reaction is in photochemical equilibrium with the reactions

$$NO_2 + h\nu \rightarrow NO + O \quad [6.2]$$

$$O + O_2 + M \rightarrow O_3 + M \quad [6.3]$$

These connections lead to the presumption that also the N_2O abundance may (indirectly) influence stratospheric chlorine partitioning. A different temporal evolution of NO_2 (or N_2O), CH_4, and O_3 therefore could result in differing trend magnitudes for HCl and $ClONO_2$. In addition, it must be considered that the rate constants of the reactions described above depend on atmospheric temperature. A decrease of stratospheric temperature from about 224 K by 4 K for example would lead to an increase of the rate constant of reaction [2.12] by about 6.2% (Table 6.1). In contrast, reactions [2.11] and [2.9] are slower for

Table 6.1: Examples for rate constant values of the major HCl and $ClONO_2$ production reactions, at two different temperatures, calculated according to Sander et al. (2011). The examples were chosen as to fit to the discussion in Section 6.4: T_1 roughly corresponds to the stratospheric temperature at about 30 km altitude in the year 2000 in the EMAC simulations discussed there, while T_2 represents a lower estimate of the temperature in the same region for the year 2050. The relative change in the rate constants was determined as $(k(T_2)-k(T_1))/k(T_1)$.

rate constant k	Cl + CH_4 [2.11]	Cl + O_3 [2.9]	ClO + NO_2 [2.12]
T_1 = 224 K	2.39×10^{-14}	9.41×10^{-12}	1.64×10^{-13}
T_2 = 220 K	2.15×10^{-14}	9.25×10^{-12}	1.74×10^{-13}
change ($T_1 \rightarrow T_2$)	-9.9%	-1.6%	+6.2%

such a lower temperature, by around 9.9% and 1.6%, respectively. So for a cooling of the stratosphere, relatively more $ClONO_2$ production and less HCl production than in a warmer stratosphere would be expected from the temperature dependency of the rate constants. In the end, the reaction rates determine the partitioning, and they depend both on the rate constants of the reactions and on the abundances of the involved species.

6.3 Sensitivity studies with EMAC

In order to investigate the possible influence of the CH_4 and N_2O trends on the difference between the trends of HCl and $ClONO_2$, sensitivity studies were performed with EMAC. This model was chosen because, like the FTIR measurements, it calculates stronger $ClONO_2$ than HCl decreases for the period 2000–2009, and especially also because it shows a similar dependency of this trend difference on latitude (see Section 6.1). Therefore, it is assumed that the responsible mechanism is contained correctly in the model. At first, an overview is given on the EMAC model and the simulations used for the sensitivity studies (Section 6.3.1). The correlation between the chlorine and CH_4 and N_2O total column abundances in the different simulations for the time range 2000–2050 is investigated in Section 6.3.2, and trends are

presented in Section 6.3.3 for the total columns and for the volume mixing ratio profiles of the involved species.

6.3.1 Model and simulations description

The EMAC (ECHAM/MESSy Atmospheric Chemistry) model is a combination of the 3-dimensional general circulation model (GCM) ECHAM5 with different modular submodels describing atmospheric processes (e.g., Jöckel et al., 2006; Kirner, 2008). The GCM and the submodels are coupled on-line via the interface MESSy (Modular Earth Submodel System) (please see http://www.messy-interface.org or Jöckel et al., 2005). The chemistry scheme is contained in the submodel MECCA (Module Efficiently Calculating the Chemistry of the Atmosphere) (Sander et al., 2005). The included chemical reactions are listed in the supplements to Sander et al. (2005) and Jöckel et al. (2006), for example. A detailed explanation of the EMAC model modular structure can be found in Jöckel et al. (2005) and its online supplement. The ECHAM5 base model is described by Roeckner et al. (2003a,b). EMAC simulates the atmosphere from the surface up to 0.01 hPa (about 80 km), on levels which follow the orography in the troposphere. This dependency of level pressure on surface pressure becomes weaker towards higher altitudes and is zero at the higher levels, above about 15 km (Kirner, 2008).

The simulations with EMAC analysed in the present work were conducted by O. Kirner at the Steinbuch Centre for Computing (SCC) of the Karlsruhe Institute of Technology (KIT). The horizontal resolution was "T42", i.e. about $2.8^\circ \times 2.8^\circ$, and 39 vertical layers were used. The time step was 600 s, and the model results were stored every 24 simulated hours. One reference simulation was performed, covering the time range 1958–2050. For this long-term simulation, the model ran freely after being initialised with meteorological fields from ERA-40 (ECMWF re-analyses). Thereby, sea surface temperature (SST) and sea ice cover (SIC) were taken from a coupled atmosphere-ocean simulation with the ECHAM5/MPI-OM model that used the A1B scenario from IPCC (2007). A comprehensive stratospheric chemistry scheme was included in the simulation. To define the boundary conditions for the ozone-depleting substances, i.e., CFCs, HCFCs, and halons, the scenario A1 from WMO (2007) was applied (see Figure 6.3). The surface volume mixing ratios of the greenhouse gases CH_4, N_2O, and CO_2 were prescribed according to the IPCC (2007) scenario A1B, thus they are consistent with SST and SIC. Figure 6.4 shows the temporal evolution of CH_4 and N_2O in this scenario, between 1960 and 2050. In the simulation, however, the prescribed CH_4, N_2O, and CH_4 mixing ratios depend on latitude, thereby accounting for the latitude-dependent annual cycle. The quasi-biennial oscillation (QBO) and the 11-year solar flux variation are not included. The sulfuric acid (H_2SO_4) mixing ratio is kept constant in the sense that the values derived from SAGE measurements for the year 1999 are repeated every year.

In addition to the reference simulation described above, two other simulations were performed with EMAC, for the time range 2000–2050. They were initialised with the meteorological and chemical fields from the reference simulation at the beginning of the year 2000. In one of the simulations, the CH_4 mixing ratio was fixed to the value of the year 2000 (global mean: about 1760 ppbv), while in the other

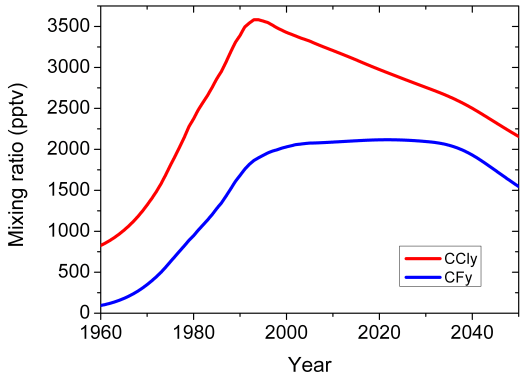

Figure 6.3: Temporal evolution of the CCl_y and CF_y surface volume mixing ratios according to the scenario A1 from WMO (2007), as prescribed as a lower boundary condition in the EMAC simulation used as a reference here, between 1960 and 2050. For the definition of CCl_y and CF_y please see page 56.

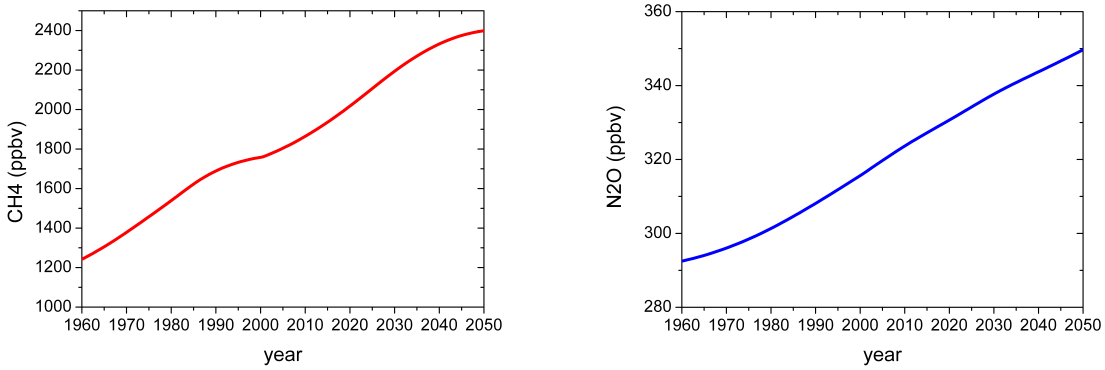

Figure 6.4: Temporal evolution of the CH_4 (left) and N_2O (right) surface volume mixing ratios according to the scenario A1B from IPCC (2007), as prescribed as a lower boundary condition in the EMAC simulation used as a reference here, between 1960 and 2050.

one, N_2O was fixed to its value of the year 2000 (global mean: about 316 ppbv). In the following, they are called the CH_4fix and N_2Ofix simulations, respectively. Apart from these two greenhouse gases, these simulations use the same boundary conditions and model setup as the reference simulation does.

6.3.2 Correlation of chlorine with methane and nitrous oxide

The linear correlation coefficient r represents a commonly used measure to determine whether two different quantities are (linearly) correlated. We are interested in the consequences of keeping the surface volume mixing ratio of CH_4 or N_2O constant especially on the HCl, $ClONO_2$, and NO_2 total column abundances. The linear correlation coefficient was determined between the total column differences in CH_4 and the differences in each of the other gases (HCl, $ClONO_2$, and NO_2) between the reference simulation and the one with constant CH_4. The analogous calculations were done for the simulation with constant N_2O. The correlation coefficient is defined as the ratio of the covariance σ_{xy} of two quantities x and y, and their standard deviations σ_x and σ_y (e.g., Taylor, 1988):

$$r = \frac{\sigma_{xy}}{\sigma_x \sigma_y} = \frac{\sum(x_i - \bar{x})(y_i - \bar{y})}{\sqrt{\sum(x_i - \bar{x})^2 \sum(y_i - \bar{y})^2}} \qquad [6.4]$$

where i is the summation index and indicates the daily values, while an overbar denotes an arithmetic mean. In our case, x represents the changes in one species, for example either CH_4 or N_2O for the CH_4fix and the N_2Ofix simulations, respectively, and y the changes in one of the other gases. The data used were the daily values of the total column abundances between 2000 and 2050, for the global mean (GM) and different latitude bins: 90–60°N (northern high latitudes, called NHL), 60–30°N (northern midlatitudes, NML), 15°N – 15 °S (tropics, TROP), 30–60°S (southern midlatitudes, SML), and 60–90°S (southern high latitudes, SHL). Because of the large variability in the stratospheric species above the high latitudes in winter and spring due to the polar vortex, we do not expect a strong correlation with the tropospheric species on a daily basis there. However, the high latitudes were included in the investigation of the EMAC sensitivity studies because FTIR measurements at the high latitude site Kiruna are discussed in Section 6.5. The resulting values for r are shown in Figure 6.5.

It is obvious that the two chlorine species exhibit a correlation with CH_4, especially for the global means, with a positive correlation of nearly 0.6 for HCl and an even stronger negative correlation with $ClONO_2$, amounting to nearly 0.8 (top panel in Figure 6.5). When separated according to the different latitude bins, the correlations for both species are highest in the midlatitudes and tropics, and smallest at the high latitudes. The positive correlation of CH_4 and HCl corresponds to the expectations from reaction [2.11], which describes the formation of HCl from Cl and CH_4. Obviously, as the total number of chlorine atoms is limited, the $ClONO_2$ total column abundances must be negatively correlated with CH_4 then.

For the comparison of the simulation with constant N_2O to the reference simulation, a positive correlation of the NO_2 change is found with the change in N_2O (right panel in Figure 6.5). With the other species, no correlation is detectable. As N_2O constitutes a major source of NO_2 (via reaction [6.1]), the

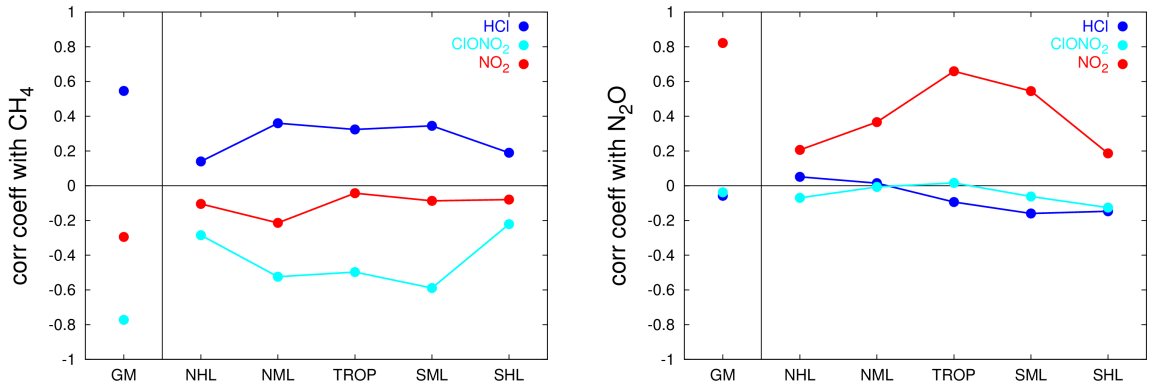

Figure 6.5: Linear correlation coefficients between different gases, determined from the three EMAC simulations, for daily values of the total column abundances between 2000 and 2050. The coefficients describe the dependency of the change in HCl, $ClONO_2$, and NO_2 when CH_4 (left) or N_2O (right) is kept constant on the value of the year 2000 instead of increasing according to the IPCC scenario A1B.

strong correlation found in Figure 6.5 agrees with the expectations. The correlation coefficient thereby is largest in the tropics because reaction [6.1] depends on sunlight via the existence of $O(^1D)$, and the availability of sunlight is much more regular in low than in high latitudes. The conclusion from this investigation of the correlations of CH_4 and N_2O with some other species is that EMAC basically shows what is expected from the chemical reactions discussed in Section 6.2. CH_4 constitutes a source for HCl, so they are positively correlated. As a result, the other stratospheric chlorine reservoir gas, $ClONO_2$, must be anticorrelated with CH_4. For N_2O, no strong connection was found with the chlorine species, only with NO_2. A difficulty in this analysis is the fact that HCl and $ClONO_2$ are stratospheric species, i.e., their mixing ratio peaks in the stratosphere, while N_2O and also CH_4 are primarily tropospheric gases. When determining the correlation between these species, the time lag resulting from the transport from the troposphere to the stratosphere (about 3 to 5 years) was not considered.

6.3.3 Chlorine trend sensitivity

In this section, the trends between 2000 and 2050 calculated from the three EMAC simulations described in Section 6.3.1 are presented. At first, the trends from the total column abundances of HCl, $ClONO_2$, CH_4, N_2O, NO_2, and O_3 are investigated, followed by the height dependency of the HCl and $ClONO_2$ volume mixing ratio (vmr) trends. O_3 was included in this investigation because it is the most important trace species in the stratosphere (Seinfeld and Pandis, 1998). Its temporal evolution is essential for life on earth, so it is interesting to also have a short look at it in the present EMAC simulations.

Total column trends

From the three EMAC simulations described in Section 6.3.1, trends have been calculated for the total column abundances of HCl, $ClONO_2$, CH_4, N_2O, NO_2, and O_3. The data used were daily values between 2000 and 2050, averaged over the same latitudes as in Section 6.3.2. A linear trend combined with a third-order Fourier series accounting for the seasonal cycle was fitted to the time series, and the error bars were determined with the bootstrap method, as explained in Chapter 4. Examples for the fits from the reference simulation are shown in Figure 6.6 for the global mean total column abundances of the six species mentioned above.

Figure 6.7 presents the latitude dependency of the trend results for these species. The CH_4 and N_2O trends of the CH_4fix and N_2Ofix simulations, respectively, also enable a certain check of the modifications made, and as expected, they are approximately zero everywhere. On the other hand, the CH_4 trends from the N_2Ofix simulation agree very well with those from the reference simulation (the trends from the reference simulation are hardly visible in Figure 6.7 because they are covered by the results from the N_2Ofix simulation). The same is the case for the N_2O trend from the CH_4fix simulation. In addition, it becomes obvious here that the N_2O trend contained in the applied scenario A1B from IPCC (2001) (about $0.22\%/\mathrm{yr}$) is considerably smaller than the CH_4 trend (about $0.84\%/\mathrm{yr}$).

From the HCl and $ClONO_2$ trend results for the different simulations, we can see that overall, keeping CH_4 constant on the level of the year 2000 has a stronger influence on the 2000–2050 trends than keeping N_2O constant on its 2000 level. HCl decreases more strongly if CH_4 is constant than it does in the two other simulations where CH_4 increases with time. This corresponds to the expectations from reaction [2.11] and from the positive correlation coefficient between the two species found in the previous section (6.3.2). If less CH_4 is available, less HCl is produced. Concerning $ClONO_2$, Section 6.3.2 showed a negative correlation with the CH_4 total column abundance. This is confirmed by the $ClONO_2$ trends which are more weakly negative if less CH_4 is available because in this case, more Cl atoms are bound in $ClONO_2$. The effect of keeping N_2O fixed on the HCl and $ClONO_2$ trends is only weak.

The general pattern of latitude dependence seen in the $ClONO_2$ trends does not change strongly if CH_4 or N_2O are kept constant: The total column abundances decrease most strongly in the tropics, and in the southern high latitudes, the decrease is even weaker than in the northern high latitudes. In all simulations, HCl decreases slightly stronger in the southern hemisphere than in the northern hemisphere, with the strongest decrease in the tropics. As for $ClONO_2$, the pattern of the HCl trends does not strongly change if CH_4 or N_2O are kept constant, except for the northern high latitudes where the HCl trend in the N_2Ofix simulation is slightly stronger than would be expected from the overall pattern and the other two simulations.

The fact that $ClONO_2$ quite distinctively shows the strongest relative decrease in the tropics in all three simulations can probably be explained by the latitudinal dependency of the total column abundances. As discussed in Section 2.2, photolysis of $ClONO_2$ (reactions [2.13] and [2.14]) is more effective in lower

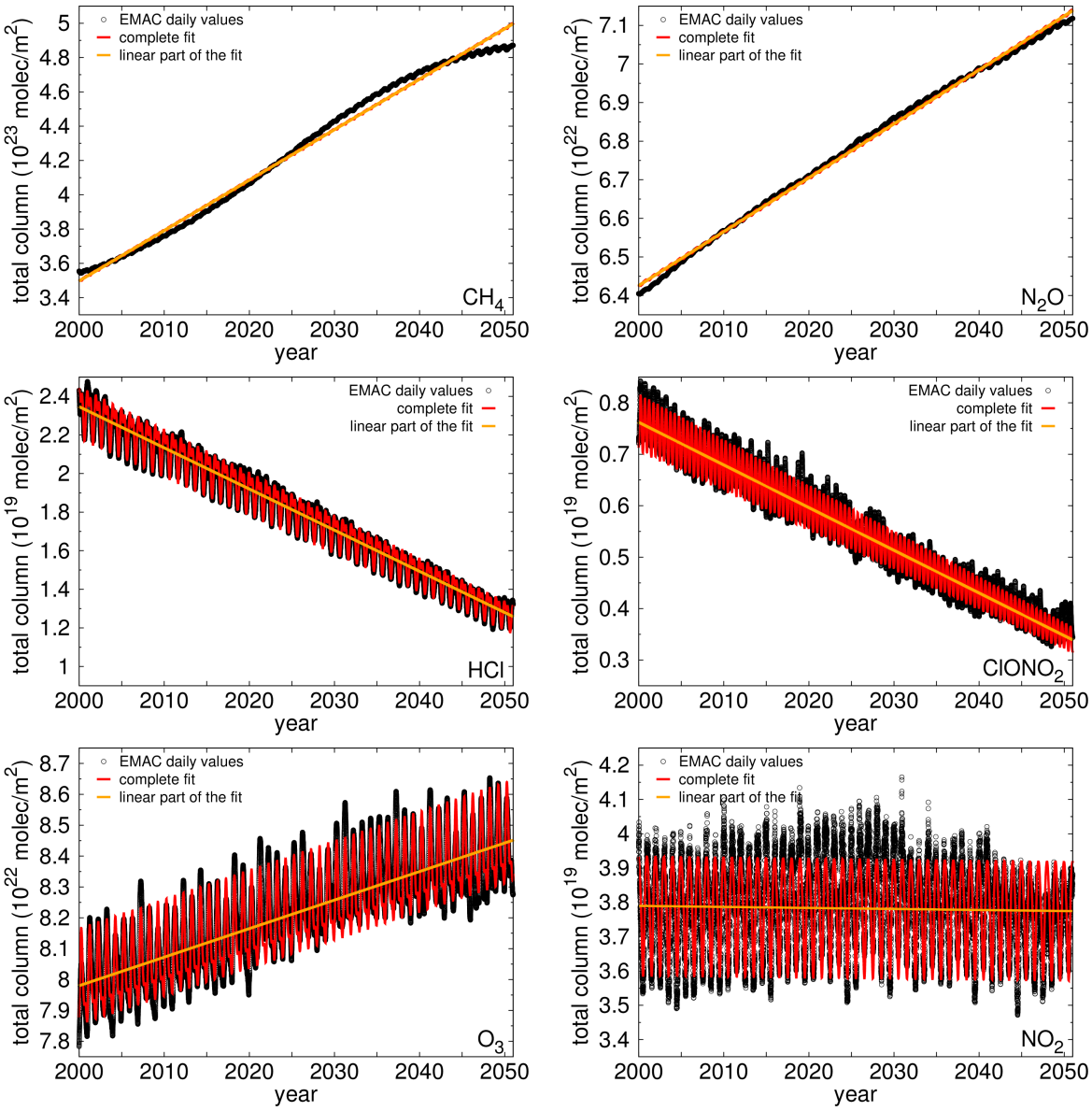

Figure 6.6: Examples of fits of function 4.1 to the globally averaged daily values of the CH_4, N_2O, HCl, $ClONO_2$, O_3, and NO_2 total column abundances calculated from the EMAC reference simulation, between 2000 and 2050. The fitting function consisted of a linear trend and a third-order Fourier series accounting for the seasonal cycle.

latitudes, leading to smaller $ClONO_2$ and larger ClO total column abundances above the tropical region than closer to the poles.

In the simulation with constant N_2O, the NO_2 total column abundance decreases with time at all latitudes. The decrease is weakest in the tropics. From reaction [2.12], we could expect the $ClONO_2$ and NO_2 trends to be positively correlated, but this is not visible in the correlation coefficients (Figure 6.5) either. In the latitudinal dependency of the trends, we even find some kind of anti-correlation, because as

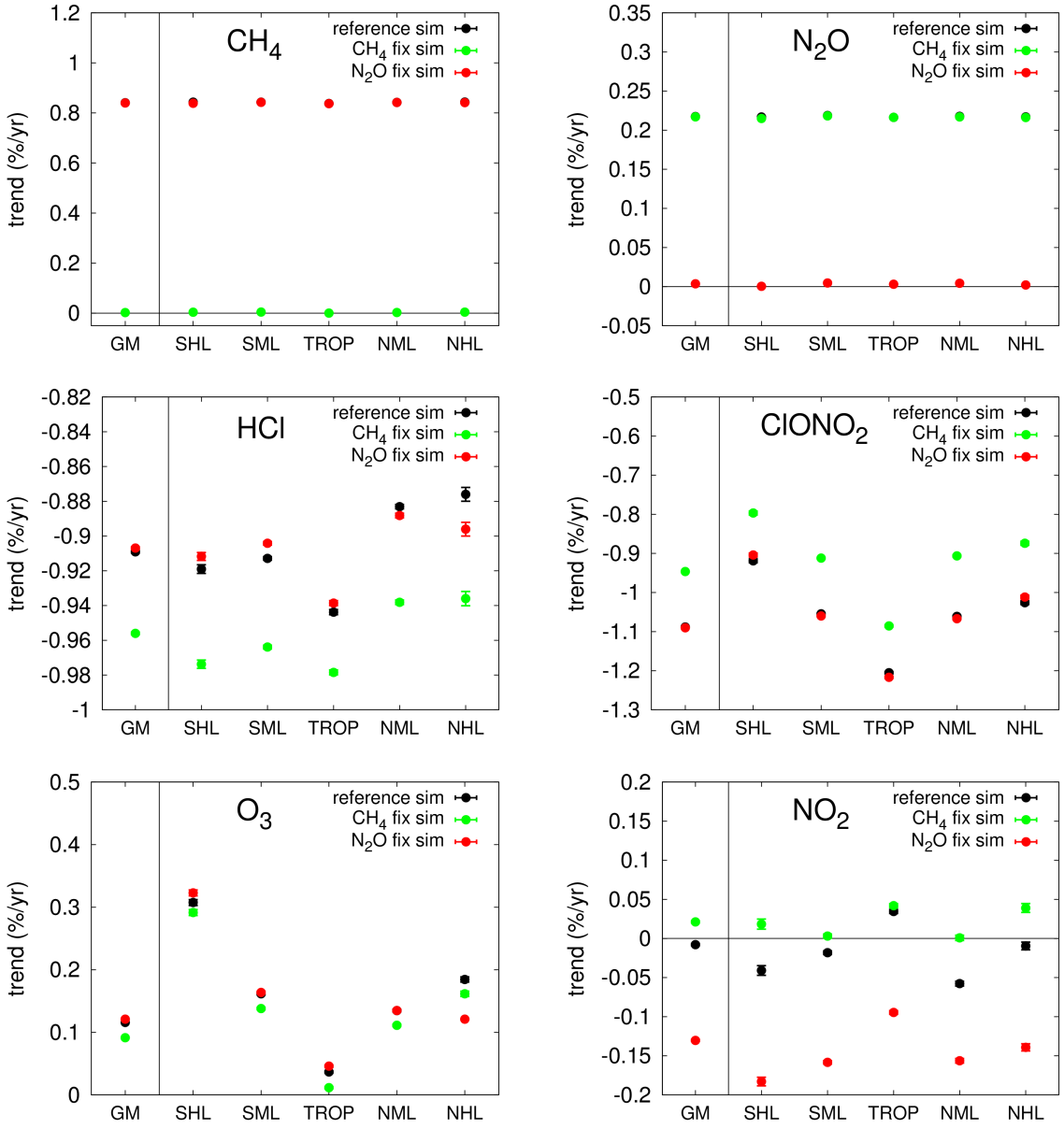

Figure 6.7: Latitudinal dependency of the trends of CH_4, N_2O, HCl, $ClONO_2$, O_3, and NO_2 total column abundances calculated from the three EMAC simulations between 2000 and 2050. The trends were determined with the bootstrap method by fitting a linear function combined with a third order Fourier series to the daily values. Please note the different y-scales. The CH_4 and N_2O trends from the reference simulation are hardly visible because they are covered by the results from the N_2Ofix and CH_4fix simulations, respectively.

described above, the $ClONO_2$ decrease is strongest in the tropics. In the reference simulation, NO_2 also decreases at most latitudes. A significant increase is simulated only for the tropical region. If CH_4 is constant, NO_2 increases or does not significantly change at all latitudes. However, the relative differences

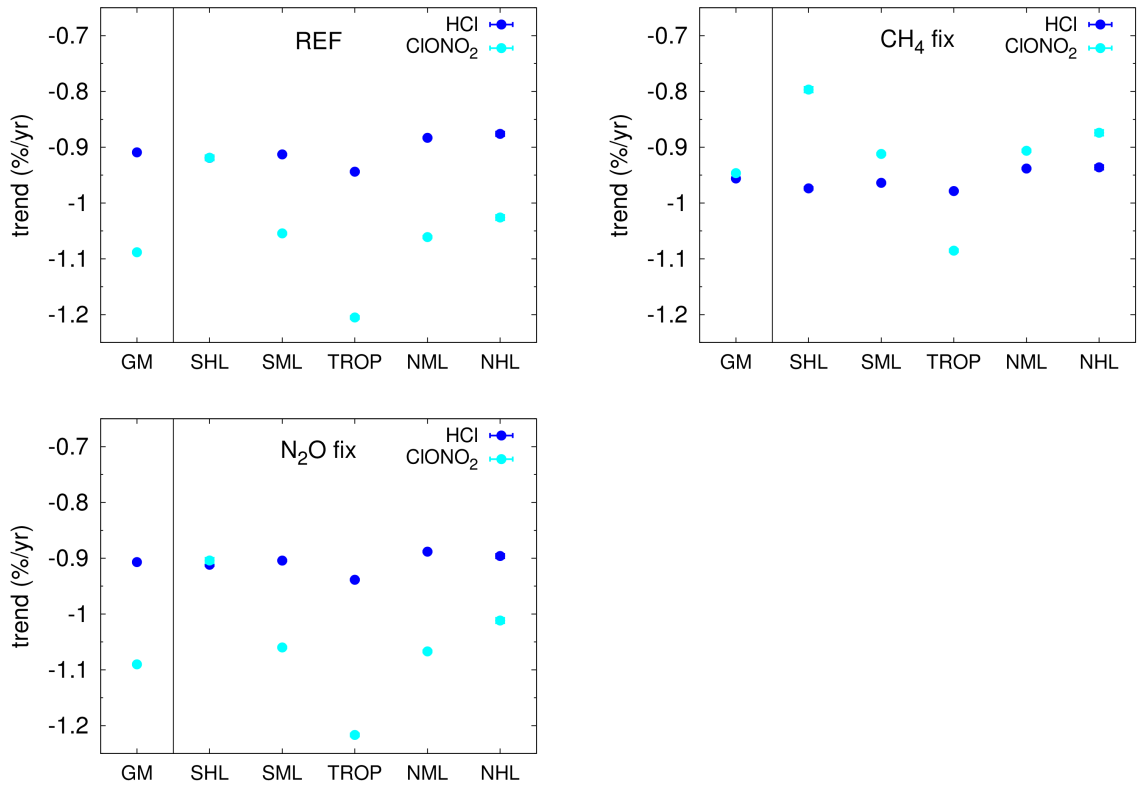

Figure 6.8: Comparison of the trends of HCl and $ClONO_2$ total column abundances calculated from the three EMAC simulations between 2000 and 2050 for different latitudes. The trends were determined with the bootstrap method by fitting a linear function combined with a third order Fourier series to the daily values.

between the three simulations in the NO_2 trends discussed above are very weak. NO_2 does not change strongly in any of the simulations.

The O_3 trends of all three simulations confirm a recovery of the stratospheric ozone layer. The strongest increases are simulated for the polar regions, with a maximum trend value in the southern high latitudes. The main reason for this is probably that the trends presented in Figure 6.7 are normalised values and the ozone depletion in the beginning of the simulation is strongest above the Antarctic.

In order to get a better overview on the influence of CH_4 and N_2O on the difference between the HCl and $ClONO_2$ trends, Figure 6.8 presents the latitudinal dependency of the difference for every simulation separately. As already obvious in Figure 6.7, the results for the chlorine trends from the N_2Ofix simulation are very similar to those from the reference simulation. On a global average (GM), $ClONO_2$ decreases stronger than HCl. When sorted according to latitude, this is also the case at all latitudes except at the southern high latitudes, where both chlorine species decrease at about the same rate. In contrast, in the CH_4fix simulation, HCl decreases faster than $ClONO_2$ at all latitudes except the tropics. On a global average, there is practically no difference between the trends.

As a conclusion from this investigation, we can state that changing the prescribed surface mixing ratio CH_4 trend in the EMAC model strongly influences the difference between the trends of the total column abundances of HCl and $ClONO_2$. A more detailed discussion can be found in the next Section (6.4).

Height-resolved trends

In order to investigate the height dependency of the difference in the HCl and $ClONO_2$ temporal evolution in the three EMAC simulations, trends were determined also for the volume mixing ratios on all 39 model levels. These calculations were performed for the same latitude bands as before, however, only the trends from the global means are shown here because the other results are qualitatively similar, with slightly larger error bars. For this investigation on the height dependency of the trends, only the annual means of the volume mixing ratios for every height were used, and a linear function was fitted to them. Otherwise, the trend (and trend error) analysis procedure was the same as described in Chapter 4.

Profiles of trends of HCl and $ClONO_2$, determined from the mixing ratios calculated in the three EMAC simulations, are presented in Figure 6.9. Only the stratospheric trends are shown here, for the layers 27 to 8, corresponding to about 223 to 0.9 hPa, or roughly 10 to 50 km altitude. As the pressure of the lower layers (27 to 23) depends weakly on orography, the pressure values on the y axis are only approximate values there. In the troposphere, the mixing ratios of HCl and $ClONO_2$ are quite small (Figure 2.4) so that it is very difficult to determine reliable trends. This is also the case for $ClONO_2$ in the mesosphere. For these reasons the results for the troposphere and mesosphere are not discussed here. Overall, it is obvious again that keeping CH_4 constant has a stronger effect on both the HCl and $ClONO_2$ trends than keeping N_2O constant. The pictures for the N_2Ofix and the reference simulation are very similar (Figure 6.9). In Figure A.1 of Appendix A.2, the same HCl and $ClONO_2$ profiles are plotted differently so that the difference in the trends between the three simulations can be compared directly. It is obvious from this figure that the difference in the $ClONO_2$ trend between the CH_4fix and the other two simulations does not vary strongly with height: The trend in the CH_4fix simulation is weaker at all model levels. In contrast, the HCl decrease in the CH_4fix simulation is stronger than in the other simulations in the stratosphere.

In the lower stratosphere, at most levels between about 220 and 70 hPa (layers number 27–22), the chlorine trends in the reference and N_2Ofix simulations agree within their bootstrap error bars (Figure 6.9). Above, the $ClONO_2$ decrease is stronger than the HCl one. In contrast, in the CH_4fix simulation, the trends of HCl and $ClONO_2$ are similar in the middle stratosphere, while in the upper and lower stratosphere, HCl decreases more strongly than $ClONO_2$.

In the following section (6.4), a detailed discussion on the results from the EMAC sensitivity studies is presented.

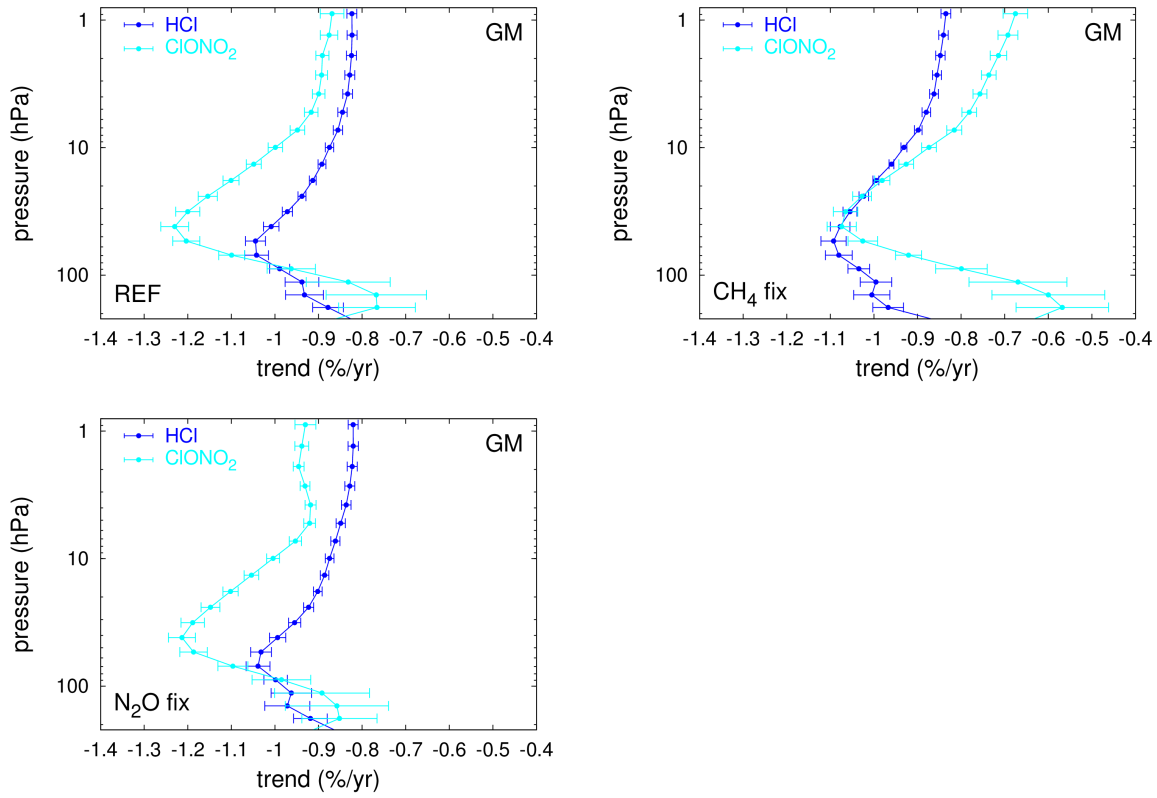

Figure 6.9: Profiles of the trends of HCl and $ClONO_2$ volume mixing ratios in the stratosphere (about 10 to 50 km altitude) calculated from the EMAC reference simulation (REF, top left panel), the CH_4fix simulation (top right panel), and the N_2Ofix simulation (lower left panel), between 2000 and 2050. The trends were determined with the bootstrap method by fitting a linear function to the global annual mean vmr values.

6.4 Discussion and conclusions from the sensitivity studies

Evidence from the EMAC sensitivity studies suggests that in case of the simulation used as reference here, the CH_4 trend has a stronger influence on the difference between the HCl and $ClONO_2$ trends than the N_2O trend does. However, we cannot exclude that this may in part result from the relative change in N_2O assumed by the A1B scenario being much smaller than the one in CH_4 (see Figures 6.4 and 6.7). The increase of CH_4 seems to be the reason for $ClONO_2$ decreasing faster than HCl in the reference simulation. From the comparison of the reference simulation with the CH_4fix simulation, it is obvious that the HCl decrease is stronger if CH_4 does not increase, and the $ClONO_2$ decrease is weaker. This corresponds very well to the assumption that reaction [2.11] producing HCl from Cl and CH_4 is less important if less CH_4 is available. Of course, only a limited amount of chlorine atoms is available so that the $ClONO_2$ trend must change accordingly. Due to the increase of CH_4, inorganic chlorine partitioning changes during the reference and N_2Ofix simulations such that the HCl production is increasingly

favoured relative to the $ClONO_2$ production, resulting in a stronger decrease of $ClONO_2$ than of HCl during 2000–2050. In contrast, in the CH_4fix simulation, no such strong effect can be detected in the HCl and $ClONO_2$ trends from the global mean total column abundances. They decrease at about the same rate, with the $ClONO_2$ decrease being slightly weaker than the HCl decrease. However, from the trend calculations for different latitude regions separately, a weaker decrease of $ClONO_2$ than of HCl is found at mid and high latitudes, but not in the tropics. This stronger decrease of HCl may be explicable by the temperature dependency of the rate coefficients of the reactions involved in chlorine partitioning. Due to the increase of the greenhouse gas mixing ratios, the troposphere warms and the stratosphere cools down (IPCC, 2007). An upper estimate for the temperature decrease at 30 km between 2000 and 2050 would be 4 K for the EMAC reference simulation (Kirner and Ruhnke, 2012, and P. Bohlinger, personal communication, 2012). This decrease is only about 0.4 and 0.2 K weaker in the CH_4fix and N_2Ofix simulations, respectively, than in the reference simulation. The fact that this difference is so small probably results mainly from the sea surface temperature (SST). The same SST (which stems from a coupled atmosphere-ocean model using the A1B greenhouse gas scenario) had to be used for all three simulations because EMAC only simulates the atmosphere. As a result, the SST increases as it is expected from the increasing CH_4 and N_2O abundances in the reference simulation, but it is probably slightly too high in both sensitivity simulations. This leads to higher tropospheric and lower stratospheric temperatures both in the CH_4fix and N_2Ofix simulations than expected from their greenhouse gas abundances.

The influence of a 4 K temperature decrease from about 224 K on the rate coefficients of reactions [2.11], [2.9], and [2.12] was discussed in Section 6.2 already. It is expected to result in a stronger relative $ClONO_2$ production at the end of the simulations compared to the beginning, leading to a weaker overall decrease of $ClONO_2$ than of HCl between 2000 and 2050 in all three simulations. However, as mentioned above, this effect is weakly visible in the CH_4fix simulation, but not at all in the other two (see Figure 6.8). So in case of the reference and N_2Ofix simulations, the favouring of $ClONO_2$ expected from the temperature decrease and the resulting changes in the rate coefficients is clearly overcompensated by the strong increase of the CH_4 mixing ratio. In other words, in the reference and N_2Ofix simulations, the effect of the increase of CH_4 manifests itself much stronger in the final rates of the reactions producing HCl and $ClONO_2$ than the change in the rate coefficients due to the temperature decrease does. In contrast, in the CH_4fix simulation, the influence of the temperature change on the rate constants does not seem to be overcompensated by any concentration changes in the involved species.

The roughly 0.3 K difference in stratospheric temperature between the three simulations around the year 2050 and the resulting influence on the rate coefficients is not expected strong enough to be detectable. However, it might be able to explain some of the differences between the N_2Ofix and the reference simulation in the HCl and $ClONO_2$ trends. As the stratosphere becomes slightly cooler during 2000–2050 in the reference than in the N_2Ofix simulation, HCl would be expected to decrease stronger in the reference than in the N_2Ofix simulation. This is the case in the southern hemisphere and tropics, and on the global average (Figure 6.7). In contrast, $ClONO_2$ would be expected to be slightly favoured at the

end of the reference simulation compared to the N_2Ofix one, leading to a weaker decrease in $ClONO_2$ between 2000 and 2050 in the reference than in the N_2Ofix simulation. This is true for the tropical and midlatitude regions, and very weakly also for the global mean (Figure 6.7). However, these differences in the chlorine trends between the reference and N_2O simulations might also be attributable to less availability of NO_2 for $ClONO_2$ production in the N_2Ofix simulation than in the reference simulation (Figure 6.7).

So as a final conclusion for this investigation on the reason for the difference between the HCl and $ClONO_2$ trends, we can state that there is considerable indication from EMAC model simulations that the CH_4 trend strongly influences this difference. The model shows only a very small difference between the trends if CH_4 is kept constant, while the HCl decrease is weaker and the $ClONO_2$ decrease stronger if CH_4 increases. For N_2O, no such strong influence on the difference between the chlorine species trends could be determined with the conducted simulations. Furthermore, in this analysis, the effect of changing rate coefficients due to the temperature changes on the partitioning between HCl and $ClONO_2$ is relatively small on a global average compared to the effect of the CH_4 increase.

6.5 The CH_4 stabilisation in the atmosphere between 1999 and 2006

In order to complete the circle, it would be nice to detect this influence of CH_4 on the chlorine trends found in the EMAC sensitivity studies also in atmospheric measurements. Usually no such experiments are possible in the real atmosphere. However, the CH_4 trend indeed changed during the period where FTIR measurements are available, so that an influence on the measured chlorine trends might be detectable. According to the fourth IPCC report, the tropospheric CH_4 volume mixing ratio increased strongly in the late 1970s and early 1980s (by up to 1%/yr), but this increase slowed down in the early 1990s and CH_4 was nearly constant between 1999 and 2005 (IPCC, 2007). Newer measurements, however, indicate that since 2007, it is on the rise again: Dlugokencky et al. (2009) found a global CH_4 increase of (8.3 ± 0.6) ppb in 2007 (corresponding to about (0.47 ± 0.04)%/yr) and of (4.4 ± 0.6) ppb in 2008 (corresponding to about (0.25 ± 0.04)%/yr). A study from FTIR total column measurements at four northern hemisphere high and midlatitude sites on average showed a slightly stronger increase between 2007 and 2009 (Angelbratt et al., 2011). In contrast to CH_4, N_2O is reported by IPCC (2007) to have increased approximately linearly at a rate of about 0.8 ppb/yr over the past few decades (until 2005), corresponding to very roughly 0.25%/yr. In order to illustrate this, the temporal evolution of the global mean surface volume mixing ratios as measured by the NOAA global air sampling network between 1979 and 2010 is shown in Figure 6.10.

The $ClONO_2$ decrease measured by the FTIR instrument at Kiruna for the time range 1996–2009 is significantly stronger than the corresponding one for HCl (Figure 6.1). In contrast, for the time range 2000–2009, no significant difference is detected, and both trends are slightly stronger than the HCl one for 1996–2009. In the following, it will be discussed whether this effect might be attributable to the above-mentioned stabilisation of CH_4 between 1999 and 2006. However, this plateau only lasted

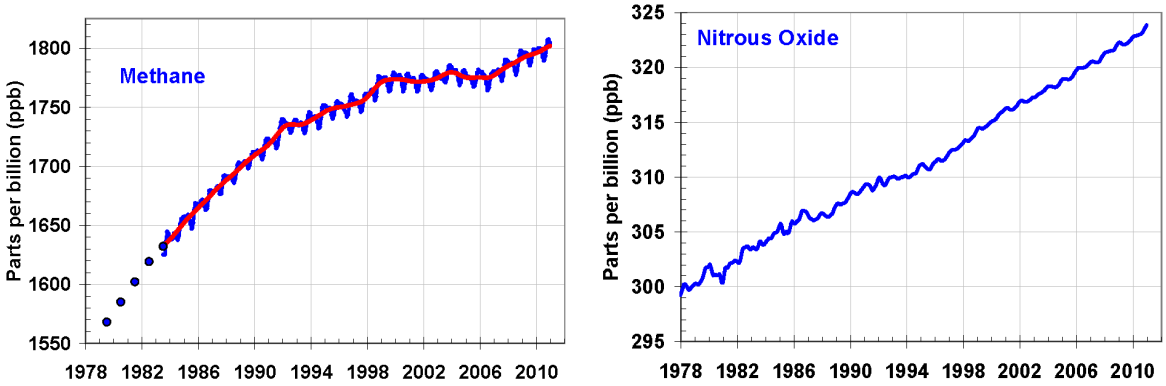

Figure 6.10: Temporal evolution of the globally averaged CH_4 (left) and N_2O (right) surface volume mixing ratios between 1979 and 2010, as measured by the NOAA global air sampling network. Figures taken from http://www.esrl.noaa.gov/gmd/aggi/.

for about 7 years, which is probably too short to reliably determine a CH_4 influence on stratospheric inorganic chlorine. In order to extend this investigation, in addition to the Kiruna site, measurements from the Jungfraujoch FTIR instrument were included. This site was chosen because the time series recorded there are very long and of very high quality. Furthermore, it represents another latitude region, being located in the middle of Europe, in contrast to the Arctic site Kiruna. For a more detailed description of these sites and their measurement specifications, please refer to Section 5.1.1 and Kohlhepp et al. (2012) and references therein.

For a comparison of the surface volume mixing ratio trend of CH_4 with total column trends of the primarily stratospheric species HCl and $ClONO_2$, the time lag due to transport from the troposphere to the stratosphere has to be considered. This time lag is assumed here to be very roughly equal to the stratospheric age-of-air which amounts to about 4 years for the Jungfraujoch and approximately 5 years for Kiruna in 20 km height (Stiller et al., 2008). So the beginning of the stabilisation of the surface CH_4 mixing ratio around 1999 reached the stratosphere above Jungfraujoch and Kiruna about 4–5 years later, around 2003/2004. For this reason, we split the available time period of HCl and $ClONO_2$ measurements in two, i.e., 1996–2003 and 2004–2009. The corresponding trend of stratospheric CH_4 is then expected to be positive for the first interval and roughly zero for the second one.

Considering the conclusions of Section 6.3.3 concerning the influence of the CH_4 abundance on stratospheric inorganic chlorine partitioning, we would therefore expect the HCl decrease to be weaker in the first period than in the second one, and vice versa for the $ClONO_2$ trend. As shown in Table 6.2, this is exactly what is found in the Kiruna trends. However, an obvious disadvantage of calculating trends for such short periods of only 8 and 6 years is that half of the results are not significantly different from 0, and most of them are not significantly different from each other either.

Possibly due to the favouring of HCl production resulting from the assumed stratospheric CH_4 increase between 1996 and 2003, no significant trend can be detected for HCl above Kiruna in this period, while

Table 6.2: Trends of HCl and $ClONO_2$ from FTIR measurements above Kiruna and the Jungfraujoch in % per year, for 1996–2009 and 2000–2009, calculated by fitting a linear function combined with a third order Fourier series to the daily means. The error bars were determined with the bootstrap method. Significant trends are in bold.

trend (%/yr)	1996–2003	2004–2009
Kiruna: HCl	-0.00 $\pm$ 0.50	-0.59 $\pm$ 0.88
Kiruna: $ClONO_2$	**-6.15 $\pm$ 1.40**	+3.76 $\pm$ 4.20
Jungfraujoch: HCl	**-0.65 $\pm$ 0.25**	**-0.42 $\pm$ 0.39**
Jungfraujoch: $ClONO_2$	+0.50 $\pm$ 0.71	**-0.87 $\pm$ 0.75**

the $ClONO_2$ decrease is significant and quite strong. In contrast, in the second period, $ClONO_2$ production is obviously favoured relative to HCl production, which again could at least partly be explained by the influence of CH_4 discussed in the previous sections. However, a quantification of the CH_4 impact is very difficult. The trend changes seen in the data are probably a combination of different effects, possibly also including the second one discussed in Section 6.4 concerning the dependency of the rate coefficients on stratospheric temperature.

At the Jungfraujoch, the trend results do not correspond to the expectations from the CH_4 stabilisation and to the trends determined for Kiruna. $ClONO_2$ shows no significant change between 1996 and 2003, and a decrease during the period 2004–2009. This would agree with the behaviour expected from the peak in stratospheric inorganic chlorine that was reached at the end of the 1990s. But in contrast, the HCl trend does not show these properties.

It was already discussed above that because HCl and $ClONO_2$ are stratospheric species, it is of course the CH_4 mixing ratio in the stratosphere that is responsible for their partitioning. As a result, the changes seen in the growth rate of the CH_4 surface volume mixing ratio (Figure 6.10) are smoothened by the mixing of air masses with different ages during the transport to the stratosphere. On the other hand, we use measurements of total column abundances of HCl and $ClONO_2$ so that the effect the changing CH_4 trend may have on some part of the atmosphere or stratosphere is also smoothened. Both facts make it even more difficult to detect the influence of the CH_4 plateau on stratospheric inorganic chlorine.

From the above-presented analysis of the atmospheric CH_4 stabilisation between 1999 and 2006, it can be concluded that there is a change in the HCl and $ClONO_2$ trends at Kiruna that may indeed be attributable to the varying availability of CH_4. However, other reasons for the differing chlorine trends for different time periods cannot be excluded. The plateau in the CH_4 mixing ratio time series was relatively short, only about 7 years, which makes a clear detection of a CH_4 influence on stratospheric chlorine partitioning difficult. Using total column abundances of the chlorine species is assumed to smoothen the possible effect of CH_4, so that alternatively, satellite data sets with a better vertical resolution might be useful for a similar analysis. However, the plateau reached in the stratospheric inorganic chlorine

time series occurred at about the same time as the stabilisation of the CH_4 abundance, during the end of the 1990s. This makes a separation of the influence of these two parameters on the HCl and $ClONO_2$ trends quite challenging, independently of the measurement type. But if the CH_4 abundance continues to increase more or less linearly during the next few years, the second trend change point in the CH_4 time series around 2006 might be helpful to determine the influence of CH_4 on stratospheric chlorine partitioning in atmospheric measurements.

7 Summary and outlook

The analyses presented in this thesis focus on trends of three stratospheric trace species, i.e., the two chlorine reservoir species HCl and $ClONO_2$, and the fluorine reservoir HF. The main interest in their temporal evolution results from the involvement of chlorine in the depletion of stratospheric ozone. In the present work, time series of FTIR measurements of total column abundances of the three species at 17 NDACC sites were compared with corresponding model output from simulations by the Bremen 2-D model, KASIMA, SLIMCAT, EMAC, and SOCOL. The primarily analysed time period was 2000–2009 as sufficient data are available from most of the measurement sites during this time. In the framework of studies on the sensitivity of the resulting trends, also the periods 1996–2009 and 2004–2009 were investigated. However, only at a few sites, significant differences between the trends for the different periods were detected. Another outcome of the sensitivity studies was the decision to determine the trends for the comparison between models and measurements by fitting a linear function combined with a (third- or first-order) Fourier series accounting for the seasonal cycle. The error bars when fitting this function were smaller than in the cases when only a linear function was fitted and when only the summer and autumn part of the time series was used. Because the solar absorption measurements with FTIR spectrometers depend on direct sunlight, no spectra can be recorded on cloudy days, nor during polar night. That leads to irregular sampling of the measurements, which may induce errors in the resulting trends. This sampling influence was investigated by comparing trends calculated from daily CTM output with those from the same time series on days with FTIR measurements only. Significant differences in the trends were found only at some polar sites, where the long-lasting polar night leads to large regular gaps in the time series. Furthermore, with a multiple linear regression approach, the influence of the 11-year solar cycle variation and of the quasi-biennial oscillation on the resulting trend was investigated for the species of interest here, at the sites Jungfraujoch and Kiruna. As no significant influence was detectable, the solar cycle and QBO time series were not included in the fitting function for the analysis and comparison of all data.

The comparison of the FTIR measurements with model data revealed an overall good agreement of the total column abundances and of their qualitative temporal evolution. The KASIMA and EMAC models tend to underestimate the HCl content, while SLIMCAT overestimates HF and $ClONO_2$, when compared to the FTIR measurements. The amplitude of the mean seasonal cycle of $ClONO_2$ is slightly too large in SLIMCAT in lower and midlatitudes, while the other models tend to underestimate it at the polar sites. The HCl and HF seasonal cycles are captured well by the models, except for the 2-D model showing a slightly too weak amplitude at many sites. Overall, the models are able to reproduce the decreasing

trend amounting to roughly -1 and -2%/yr in the HCl and $ClONO_2$ measurements, respectively, and the HF increase by about 1%/yr during the period 2000–2009. However, the measured chlorine decreases are stronger and the HF increases weaker in the northern than in the southern hemisphere, while this difference cannot be found in the model results. A possible reason for this hemispheric dependency of the FTIR trends is the distribution of the ODS emission sources, which concentrate in the northern hemisphere. The models obviously do not consider this fact.

At most of the included NDACC sites, $ClONO_2$ decreases stronger than HCl does, both in the measurements and the model results. This interesting and at first unexpected fact was described previously already by Mikuteit (2008), in the SPARC-CCMVal (2010) report and by Kohlhepp et al. (2011), for example. Sensitivity studies conducted with EMAC model simulations in the present work revealed a strong influence of the CH_4 abundance and its temporal evolution on the partitioning of inorganic chlorine into HCl and $ClONO_2$. The influence of N_2O, in contrast, was found to be much weaker. A strong increase in the CH_4 mixing ratio leads to HCl production being increasingly favoured at the cost of $ClONO_2$ production so that HCl decreases less strongly than $ClONO_2$ in this case.

An indication for the influence of CH_4 was then searched for also in the FTIR chlorine measurements at Kiruna and the Jungfraujoch because the stabilisation of the tropospheric CH_4 mixing ratio between 1999 and 2006 together with its increase before and afterwards seems to provide a unique setting for such an investigation. Especially the stronger decrease of $ClONO_2$ than of HCl above Kiruna during 1996–2009 may be attributable to the increasingly favoured HCl production as the CH_4 mixing ratio increases. In contrast, the HCl and $ClONO_2$ trends are approximately equal during 2000–2009, when CH_4 did not change as strongly. However, the Jungfraujoch FTIR data do not show this effect. At this site, it may be overcompensated by the peak in stratospheric inorganic chlorine occurring also at the end of the 1990s. The influence of this effect cannot be separated easily from the possible impact of the CH_4 stabilisation, especially for HCl. As described above, the CH_4 mixing ratio was approximately constant from 1999 until about 2006 but then started increasing again. In case it continues to increase at an approximately linear rate for the next few years, this second turning point in the CH_4 time series around 2006/2007 can be used to investigate the CH_4 influence on chlorine partitioning with atmospheric measurements. As a result of using total column abundances for the studies presented here, the CH_4 influence is probably weakened. From measurements with a higher vertical resolution, e.g., by satellites, more distinct results might be obtained.

As stated for example by WMO (2011), the decrease of the atmospheric chlorine (and bromine) content is not the only factor influencing the recovery of the stratospheric ozone layer, although it is the most important one. Due to climate change, stratospheric temperature decreases, leading to an enhanced ozone production rate in the upper stratosphere (e.g., Müller, 2012). In addition, the projected strengthening of the Brewer-Dobson circulation is expected to contribute to a faster return of the ozone abundance to its 1980 and 1960 values. So overall, global total ozone is estimated to recover more quickly than expected from the decrease in stratospheric halogen loading (Müller, 2012). One exception is the Antarctic, where

the ODS influence is relatively much stronger than the influence of climate change. So ozone recovery there corresponds more closely to the temporal evolution of the ODS concentrations and thus occurs later than in the rest of the world. Simulations also indicate that in the tropics, ozone levels may never return to the 1980 or 1960 conditions because the strengthening of the Brewer-Dobson circulation leads to a decrease of ozone production in the lower stratosphere (WMO, 2011; Müller, 2012). According to Ravishankara et al. (2009), along with the decrease in anthropogenic chlorine and bromine source gases, the importance of N_2O as an ODS will gradually increase within this century due to its projected increasing or at least continuing anthropogenic emission.

Stratospheric halogen levels are projected to return to 1960 levels only by the end of this century (WMO, 2011). So despite climate change and the increasing N_2O abundance, the stratospheric halogen loading will remain the most important factor influencing the ozone layer for many years to come. It is thus essential to continue monitoring the stratospheric inorganic chlorine content and its anthropogenic source gases. In this context, the global ground-based Network for the Detection of Atmospheric Composition Change is very important because it provides long time series which enable reliable trend determinations. In addition, atmospheric chemistry models and data from satellites with usually much shorter lifetimes need to be validated by such long-term measurements.

Acknowledgment

Hiermit möchte ich mich sehr herzlich bei Herrn Prof. Dr. Herbert Fischer für die interessante Themenstellung und die Übernahme des Referats bedanken, ebenso wie für die Durchsicht dieser Arbeit. Herrn Priv.-Doz. Dr. Michael Höpfner bin ich ebenfalls sehr dankbar für die Übernahme des Korreferats und die Durchsicht der vorliegenden Arbeit.

Besonderer Dank geht auch an meine direkten Betreuer Thomas Blumenstock und Roland Ruhnke für ihre ständige Unterstützung während meiner Promotionszeit, für unzählige Diskussionen interessanter Fragestellungen und für die Korrektur dieser Arbeit. Ebenso möchte ich Frank Hase und Ole Kirner für ihre Diskussionsbereitschaft und die Anmerkungen und Korrekturvorschläge zu Teilen der vorliegenden Arbeit danken. Für die Durchführung der Sensitivitätssimulationen mit EMAC bin ich Ole Kirner ebenfalls sehr dankbar.

I am very grateful to the members of the NDACC infrared working group (and their supporters) for measuring and providing the time series of HCl, $ClONO_2$, and HF total column abundances that were analysed in this thesis. It was a great pleasure working with them and meeting them at some very special places around the world. I would like to especially thank the group of Emmanuel Mahieu at Liège, Belgium, for providing newer time series until 2011 from the Jungfraujoch. They would like to acknowledge vital funding by the Belgian Science Policy Office (BELSPO), the F.R.S.-FNRS and the Fédération Wallonie-Bruxelles. Further thanks go to the International Foundation High Altitude Research Stations Jungfraujoch and Gornergrat (HFSJG, Bern) for supporting the facilities needed to perform the observations.

For providing me with the results from their simulations, I would like to thank the modellers (and their supporters) of the Bremen 2-D model, KASIMA, SLIMCAT, EMAC, and SOCOL very much, too.

In particular, I am very thankful to the co-authors of the paper on the comparison of models and measurements for the fruitful discussions concerning the results derived from their data.

The NCEP temperature and pressure profiles used for the retrieval of the FTIR results were provided by the NASA Goddard Automailer system. Furthermore, the QBO and solar cycle time series were measured and provided on their internet page by Freie Universität Berlin and Natural Resources Canada, respectively. Thank you very much for these data.

Meinen Kollegen danke ich für die sehr gute Nachbarschaft, die angenehme Arbeitsatmosphäre und ihre ständige Bereitschaft zur Diskussion bzw. Beantwortung von Fragen. Dies gilt besonders für meine wechselnden, aber immer sehr angenehmen Zimmerkollegen.

Ganz besonders möchte ich auch meinen Eltern und den Freunden danken, die Teile meiner Arbeit gelesen und kommentiert haben. Und nicht zuletzt bin ich meiner Familie und meinen Freunden sehr dankbar für ihre ständige Unterstützung während meiner Promotionszeit und besonders auch in deren Endphase.

Karlsruhe, im Juni 2012 *Regina Kohlhepp*

A Appendix

A.1 Measurement specifications of HCl, $ClONO_2$, and HF at the 17 NDACC sites

Table A.1: Specifications of the FTIR measurements of HCl at the 17 NDACC sites used for the comparison with the models in Chapter 5.

Measurement site	Spectral resolution [cm^{-1}]	Spectral microwindows [cm^{-1}]	Retrieved interfering species	Source of p/T profiles	Retrieval code	Spectroscopic database	Reference
Eureka DA8 (1997-2006)	0.004	2925.70-2926.10	NO_2	radiosondes, NCEP, US Sub-Arctic Winter Model	SFIT1.09e	HITRAN 1992 plus updates	Fast et al. (2011)
Eureka 125HR (2006-2009)	0.0035	2775.72-2775.80 2821.40-2821.62 2925.75-2926.05	O_3, CH_4, N_2O; HDO, N_2O; CH_4, NO_2, OCS, O_3	radiosondes, NCEP, US St. Atm.	SFIT2 v3.92C	HITRAN 2004 plus updates	Batchelor et al. (2009)
Ny Ålesund	0.005	2925.65-2926.25	CH_4	NCEP	GFIT	updated ATMOS linelist from GFIT package, v2.6.4	Notholt et al. (1995b)
Thule	0.0035	2727.60-2727.95 2775.60-2775.95 2925.70-2926.10	O_3, CH_4, HDO	NCEP	SFIT2 v3.93	HITRAN 2004 plus updates to 2007	Hannigan et al. (2009)
Kiruna	0.005	2727.73-2727.82 2775.73-2775.79 2819.52-2819.61 2821.52-2821.62 2843.60-2843.65 2904.09-2904.14 2923.65-2923.78 2925.80-2926.00 2942.70-2942.75 2961.04-2961.09 2963.25-2963.32 2995.76-2995.79	H_2O, O_3, CH_4	NCEP	PROFFIT	HITRAN 2004	Blumenstock et al. (2006)
Poker Flat	0.0035	2925.80-2926.00	H_2O, CH_4, NO_2, O_3	radiosondes, UKMO, CIRA86	SFIT2 v3.7	HITRAN 2004	Kagawa et al. (2007)

Table A.1: Continued: Specifications of the FTIR measurements of HCl at the 17 NDACC sites used for the comparison with the models in Chapter 5.

Measurement site	Spectral resolution [cm^{-1}]	Spectral microwindows [cm^{-1}]	Retrieved interfering species	Source of p/T profiles	Retrieval code	Spectroscopic database	Reference
Harestua		2925.60-2926.20 2925.75-2926.00	H_2O, CH_4, NO_2, HCl, O_3	NCEP	SFIT2 v3.81	HITRAN 2004	
Zugspitze	0.005	2925.74-2926.06	CH_4	Munich radiosonde	SFIT1.09e	HITRAN 1996	Sussmann and Schäfer (1997)
Jungfraujoch	0.003	2925.74-2926.06	CH_4, NO_2	NCEP	SFIT1.09c	HITRAN 1992	Rinsland et al. (2003)
Toronto	0.004	2925.80-2926.00	CH_4, NO_2, O_3	NCEP, US St. Atm.	SFIT2 v3.82B3	HITRAN 2004	Wiacek et al. (2007)
Tsukuba	0.0035	2925.69-2926.21	CH_4, H_2O	radiosondes at Tateno	SFIT1.09e	HITRAN 1996	Murata et al. (2005)
Izaña	0.0036	same as Kiruna	H_2O, O_3, CH_4	local radiosondes	PROFFIT	HITRAN 2004	Schneider et al. (2005)
Mauna Loa	0.0035	2925.69-2926.50	CH_4	radiosondes at Hilo	SFIT1	HITRAN 2000	Hannigan et al. (2009)
La Réunion	0.00513 and 0.00893	2925.70-2926.10	CH_4	NCEP	SFIT2 v3.9	HITRAN 2004 plus updates for H_2O, N_2O, HNO_3, C_2H_6	Senten et al. (2008)
Wollongong	0.0035	2925.80-2926.00	CH_4	NCEP	GFIT	HITRAN 2004	Rinsland et al. (2003)
Lauder	0.0035	2925.75-2926.05	CH_4, NO_2, H_2O, O_3	NCEP/ NCAR	SFIT2 v3.82B3	HITRAN 2000	Rinsland et al. (2003)
Arrival Heights	0.0035	2925.75-2926.05	CH_4, NO_2, H_2O, O_3	NCEP/ NCAR	SFIT2 v3.82B3	HITRAN 2000	Mahieu et al. (2008)

Table A.2: Specifications of the FTIR measurements of HF at the 17 NDACC sites used for the comparison with the models in Chapter 5.

Measurement site	Spectral resolution [cm^{-1}]	Spectral microwindows [cm^{-1}]	Retrieved interfering species	Source of p/T profiles	Retrieval code	Spectroscopic database	Reference
Eureka DA8 (1997-2006)	0.004	4038.78-4039.10	H_2O	radiosondes, NCEP, US Sub-Arctic Winter Model	SFIT1.09e	HITRAN 1992 plus updates	Fast et al. (2011)
Eureka 125HR (2006-2009)	0.0035	4038.78-4039.10	H_2O, HDO, CH_4	radiosondes, NCEP, US St. Atm.	SFIT2 v3.92C	HITRAN 2004 plus updates	Batchelor et al. (2009)

Table A.2: Continued: Specifications of the FTIR measurements of HF at the 17 NDACC sites used for the comparison with the models in Chapter 5.

Measurement site	Spectral resolution [cm^{-1}]	Spectral microwindows [cm^{-1}]	Retrieved interfering species	Source of p/T profiles	Retrieval code	Spectroscopic database	Reference
Ny Ålesund	0.005	4038.60-4039.24	H_2O	NCEP	GFIT	updated ATMOS-linelist from GFIT package, v2.6.4	Notholt et al. (1995a)
Thule	0.0035	4000.80-4001.20 4038.75-4039.20	H_2O, CH_4, HDO	NCEP	SFIT2 v3.93	HITRAN 2004 plus updates to 2007	Hannigan et al. (2009)
Kiruna	0.0075	4000.90-4001.05 4038.85-4039.08	H_2O	NCEP	PROFFIT	HITRAN 2004	Blumenstock et al. (2006)
Poker Flat	0.0035	4038.804-4039.15	H_2O	radiosondes, UKMO, CIRA86	SFIT2 v3.7	HITRAN 2004	Kagawa et al. (2007)
Harestua		4038.10-4039.50 4038.86-4039.05	H_2O, HDO, CH_4, HF	NCEP	SFIT2 v3.81	HITRAN 2004	
Zugspitze	0.0078	4038.80-4039.10	H_2O column	Munich Radiosonde	SFIT1.09e	HITRAN 1996	Sussmann and Schäfer (1997)
Jungfraujoch	0.004	4038.80-4039.105	CH_4, NO_2	NCEP	SFIT1.09c	HITRAN 1992	Zander et al. (2008)
Toronto	0.004	4038.77-4039.13	H_2O, HDO, CH_4	NCEP, US St. Atm.	SFIT2 v3.82B3	HITRAN 2004	Wiacek et al. (2007)
Tsukuba	0.0035	4038.80-4039.10	H_2O, HDO, CH_4	radiosonde	SFIT1.09e	HITRAN 1996	Murata et al. (2005)
Izaña	0.0036	4000.90-4001.05 4038.85-4039.08	H_2O	local radiosondes	PROFFIT	HITRAN 2004	Schneider et al. (2005)
Mauna Loa	0.0035	4038.85-4039.05	H_2O	radiosondes at Hilo	SFIT1	HITRAN 2000	Hannigan et al. (2009)
La Réunion	0.0072	4038.70-4039.05	H_2O	NCEP	SFIT2 v3.9	HITRAN 2004 updates for H_2O, N_2O, HNO_3, C_2H_6	Senten et al. (2008)
Wollongong	0.0035	4038.81-4039.09	H_2O	NCEP	GFIT	HITRAN 2004	Mahieu et al. (2008)
Lauder	0.0035	4038.78-4039.01	H_2O, HDO, CH_4	NCEP/ NCAR	SFIT2 v3.82B3	HITRAN 2000	Reisinger et al. (1994)
Arrival Heights	0.0035	4038.78-4039.10	H_2O, HDO, CH_4	NCEP/ NCAR	SFIT2 v3.82B3	HITRAN 2000	Reisinger et al. (1994)

Table A.3: Specifications of the FTIR measurements of $ClONO_2$ at the 12 NDACC sites used for the comparison with the models in Chapter 5.

Measurement site	Spectral resolution [cm^{-1}]	Spectral microwindows [cm^{-1}]	Retrieved interfering species	Source of p/T profiles	Retrieval code	Spectroscopic database	Reference
Eureka DA8 (1997-2006)	0.004	779.550-781.100	O_3, H_2O, CO_2, C_2H_2	radiosondes, NCEP, US Sub-Arctic Winter Model	SFIT1.09e	HITRAN 1992 plus updates	Fast et al. (2011)
Eureka 125HR (2006-2009)	0.0035	779.850-780.450 782.550-782.870 938.300-939.300	CO_2, O_3, HNO_3; O_3, CO_2, H_2O, HNO_3; CO_2	radiosondes, NCEP, US St. Atm.	SFIT2 v3.92C	HITRAN 2004 plus updates	Batchelor et al. (2009)
Ny Ålesund	0.005	778.640-782.800	O_3, CO_2, H_2O, C_2H_2	NCEP	GFIT	updated ATMOS-linelist from GFIT package, v2.6.4	Notholt et al. (1995b)
Thule	0.01	780.120-780.320 780.700-781.250	O_3, CO_2	NCEP	SFIT2 v3.93	HITRAN 2004 plus updates to 2007	Hannigan et al. (2009)
Kiruna	0.005	779.000-779.800 780.000-780.300 780.300-781.300	H_2O, CO_2, O_3, HNO_3, C_2H_2	NCEP	PROFFIT	HITRAN 2004	Blumenstock et al. (2006)
Harestua		779.500-780.700 779.905-780.340	CO_2, H_2O, O_3, $ClONO_2$, HNO_3	NCEP	SFIT2 v3.81	HITRAN 2004	
Zugspitze	0.0036	779.300-780.600 780.050-780.355	H_2O, O_3, CO_2	Munich radiosonde	SFIT2 v3.8	HITRAN 1996 with Birk parameters for $ClONO_2$	Sussmann and Schäfer (1997)
Jungfraujoch	0.005	779.300-780.600 780.050-780.355	Wide: H_2O, O_3, CO_2; Narrow: O_3, HNO_3, COF_2	NCEP	SFIT2 v3.81	HITRAN 1996 including Birk and Wagner line parameters	Rinsland et al. (2003)
Izaña	0.0036	779.000-779.800 780.000-780.300 780.300-781.300	H_2O, CO_2, O_3, HNO_3, C_2H_2	local radiosondes	PROFFIT	HITRAN 2004	Schneider et al. (2005)
Wollongong	0.0035	779.300-780.600 780.050-780.355	Wide: O_3, H_2O, CO_2, C_2H_2; Narrow: none	NCEP	SFIT2 v3.92	HITRAN 2004	Rinsland et al. (2003)
Lauder	0.0035	779.300-780.600 780.050-780.355	Wide: O_3, H_2O, CO_2, C_2H_2; Narrow: none	NCEP/ NCAR	SFIT2 v3.82B3	HITRAN 2000	Rinsland et al. (2003)
Arrival Heights	0.0035	779.300-780.600 780.050-780.355	Wide: O_3, H_2O, CO_2, C_2H_2; Narrow: none	NCEP/ NCAR	SFIT2 v3.82B3	HITRAN 2000	Rinsland et al. (2003)

A.2 Trend profiles of HCl and $ClONO_2$ from EMAC

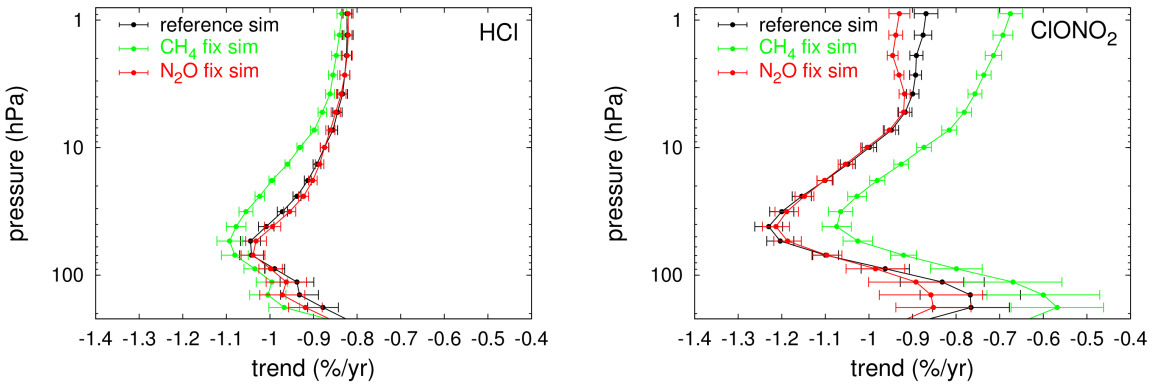

Figure A.1: Profiles of the trends of HCl (left) and $ClONO_2$ (right) volume mixing ratios calculated from the three EMAC simulations discussed in Chapter 6, between 2000 and 2050. The trends were determined with the bootstrap method by fitting a linear function to the global annual mean vmr values. This figure is just another way of plotting the results already shown in Figure 6.9. This was done in order to see the difference between the simulations more clearly.

B List of Figures

C List of Tables

D Bibliography

Ahrens, C. D.: Meteorology Today. An introduction to weather, climate, and the environment, West Publishing Company, St Paul, Minnesota, USA, 5 edn., 1994.

Angelbratt, J., Mellqvist, J., Blumenstock, T., Borsdorff, T., Brohede, S., Duchatelet, P., Forster, F., Hase, F., Mahieu, E., Murtagh, D., Petersen, A. K., Schneider, M., Sussmann, R., and Urban, J.: A new method to detect long term trends of methane (CH_4) and nitrous oxide (N_2O) total columns measured within the NDACC ground-based high resolution solar FTIR network, Atmos. Chem. Phys., 11, 6167–6183, doi:10.5194/acp-11-6167-2011, 2011.

Atkinson, R., Baulch, D. L., Cox, R. A., Crowley, J. N., Hampson, R. F., Hynes, R. G., Jenkin, M. E., Rossi, M. J., and Troe, J.: Evaluated kinetic and photochemical data for atmospheric chemistry: Volume I - gas phase reactions of O_x, HO_x, NO_x and SO_x species, Atmos. Chem. Phys., 4, 1461–1738, 2004.

Atkinson, R., Baulch, D. L., Cox, R. A., Crowley, J. N., Hampson, R. F., Hynes, R. G., Jenkin, M. E., Rossi, M. J., and Troe, J.: Evaluated kinetic and photochemical data for atmospheric chemistry: Volume II, gas phase reactions of organic species, Atmos. Chem. Phys., 6, 3625–4055, 2006.

Baldwin, M. P., Gray, L. J., Dunkerton, T. J., Hamilton, K., Haynes, P. H., Randel, W. J., Holton, J. R., Alexander, M. J., Hirota, I., Horinouchi, T., Jones, D. B. A., Kinnersley, J. S., Marquardt, C., Sato, K., and Takahashi, M.: The quasi-biennial oscillation, Reviews of Geophysics, 39, 179–229, 2001.

Batchelor, R. L., Kolonjari, F., Lindenmaier, R., Mittermeier, R. L., Daffer, W., Fast, H., Manney, G., Strong, K., and Walker, K. A.: Four Fourier transform spectrometers and the Arctic polar vortex: instrument intercomparison and ACE-FTS validation at Eureka during the IPY springs of 2007 and 2008, Atmos. Meas. Tech., 3, 51–66, 2010.

Beer, R.: Remote sensing by Fourier transform spectroscopy, in: Chemical analysis. A series of monographs on analytical chemistry and its applications, edited by Winefordner, J. D., vol. 120, John Wiley & Sons, Inc., 1992.

Blumenstock, T., Kopp, G., Hase, F., Hochschild, G., Mikuteit, S., Raffalski, U., and Ruhnke, R.: Observation of unusual chlorine activation by ground-based infrared and microwave spectroscopy in the late Arctic winter 2000/01, Atmos. Chem. Phys., 6, 897–905, 2006.

Brasseur, G. and Solomon, S.: Aeronomy of the middle atmosphere, Atmospheric Sciences Library, D. Reidel Publishing Company, Dordrecht, Holland, 2 edn., 1986.

Bühlmann, P.: Bootstraps for Time Series, Statistical Science, 17, 52–72, 2002.

Chapman, S.: A theory of upper atmospheric ozone, Memoirs of the Royal Meteorological Society, 3, 103–125, 1930.

Chipperfield, M. P., Burton, M., Bell, W., Paton-Walsh, C., Blumenstock, T., Coffey, M. T., Hannigan, J. W., Mankin, W. G., Galle, B., Mellqvist, J., Mahieu, E., Zander, R., Notholt, J., Sen, B., and Toon, G. C.: On the use of HF as a reference for the comparison of stratospheric observations and models, J. Geophys. Res., 102, 12 901–12 919, 1997.

Chubachi, S.: A special ozone observation at Syowa station, Antarctica, from Feb.1982 to Jan 1983, in: Atmospheric ozone: Proceedings of the Quadrennial Ozone Symposium held in Halkidiki, Greece, 3-7 September 1984, edited by Zerefos, C. S. and Ghazi, A., D. Reidel Publ. Comp., Dordrecht, 1984.

Considine, G. D., Deaver, L. E., Remsberg, E. E., and III, J. M. R.: Analysis of near-global trends and variability in Halogen Occultation Experiment HF and HCl data in the middle atmosphere, J. Geophys. Res., 104, 24 297–24 308, 1999.

Crutzen, P. J.: The influence of nitrogen oxides on the atmospheric ozone content, Q. J. R. Meteorol. Soc., 96, 320–325, 1970.

Davison, A. C. and Hinkley, D. V.: Bootstrap Methods and Their Application, Cambridge University Press, 1997.

Davison, A. C. and Kuonen, D.: An Introduction to the Bootstrap with Applications in R, Statistical Computing and Statistical Graphics Newsletter, 13, 6–11, 2002.

Dlugokencky, E. J., Bruhwiler, L., White, J. W. C., Emmons, L. K., Novelli, P. C., Montzka, S. A., Masarie, K. A., Lang, P. M., Crotwell, A. M., Miller, J. B., and Gatti, L. V.: Observational constraints on recent increases in the atmospheric CH_4 burden, Geophys. Res. Lett., 36, L18 803, doi: 10.1029/2009GL039780, 2009.

Duchatelet, P.: Fluorine in the atmosphere: Inorganic fluorine budget and long-term trends based on FTIR measurements at Jungfraujoch, PhD thesis at the University of Liège, Belgium, 2011.

Duchatelet, P., Demoulin, P., Hase, F., Ruhnke, R., Feng, W., Chipperfield, M., Bernath, P., Boone, C., Walker, K., and Mahieu, E.: Hydrogen fluoride total and partial column time series above the Jungfraujoch from long-term FTIR measurements: Impact of the line-shape model, characterization of the error budget and seasonal cycle, and comparison with satellite and model data, J. Geophys. Res., 115, 2010.

Dunkerton, T.: On the Mean Meridional Mass Motions of the Stratosphere and Mesosphere, J. Atmos. Sci., pp. 2325–2333, 1978.

Efron, B.: Bootstrap Methods: Another Look at the Jackknife, The Annals of Statistics, 7, 1–26, 1979.

Efron, B.: Second Thoughts on the Bootstrap, Statistical Science, 18, 135–140, 2003.

Efron, B. and Tibshirani, R.: Bootstrap Methods for Standard Errors, Confidence Intervals, and Other Measures of Statistical Accuracy, Statistical Science, 1, 54–75, 1986.

Efron, B. and Tibshirani, R.: Statistical Data Analysis in the Computer Age, Science, New Series, 253, 390–395, 1991.

Efstathiou, M. N. and Varotsos, C. A.: On the 11 year solar cycle signature in global total ozone dynamics, Meteorol. Appl., doi:10.1002/met.1287, 2012.

Farman, J. C., Gardiner, B. G., and Shanklin, J. D.: Large losses of total ozone in Antarctica reveal seasonal ClO_x/NO_x interaction, Nature, 315, 207–210, 1985.

Fast, H., Mittermeier, R. L., and Makino, Y.: A ten-year record of Arctic trace gas total column measurements at Eureka, Canada, from 1997 to 2006, Atmosphere-Ocean, 49, 67–94, 2011.

Froidevaux, L., Livesey, N. J., Read, W. G., Salawitch, R. J., Waters, J. W., Drouin, B., MacKenzie, I. A., Pumphrey, H. C., Bernath, P., Boone, C., Nassar, R., Montzka, S., Elkins, J., Cunnold, D., and Waugh, D.: Temporal decrease in upper atmospheric chlorine, Geophys. Res. Lett., 33, L23 812, doi:10.1029/2006GL027600, 2006.

García, O. E., Schneider, M., Redondas, A., González, Y., Hase, F., Blumenstock, T., and Sepúlveda, E.: Investigating the long-term evolution of subtropical ozone profiles applying ground-based FTIR spectrometry, Atmos. Meas. Tech. Discuss., 5, 3431–3471, doi:10.5194/amtd-5-3431-2012, 2012.

Gardiner, T., Forbes, A., de Mazière, M., Vigouroux, C., Mahieu, E., Demoulin, P., Velazco, V., Notholt, J., Blumenstock, T., Hase, F., Kramer, I., Sussmann, R., Stremme, W., Mellqvist, J., Strandberg, A., Ellingsen, K., and Gauss, M.: Trend analysis of greenhouse gases over Europe measured by a network of ground-based remote FTIR instruments, Atmos. Chem. Phys., 8, 6719–6727, 2008.

Gatz, D. F. and Smith, L.: The standard error of a weighted mean concentration – I. Bootstrapping vs. other methods, Atmos. Environ., 29, 1185–1193, 1995.

Gisi, M., Hase, F., Dohe, S., and Blumenstock, T.: Camtracker: a new camera-controlled high precision solar tracker system for FTIR spectrometers, Atmos. Meas. Tech., 4, 47–54, 2011.

Goncalves, S. and White, H.: Bootstrap Standard Error Estimates for Linear Regression, Journal of the American Statistical Association, 100, 970–979, 2005.

Graedel, T. E. and Crutzen, P. J.: Chemie der Atmosphäre, Spektrum Akademischer Verlag, 1994.

Gray, L. J., Beer, J., Geller, M., Haigh, J. D., Lockwood, M., Matthes, K., Cubasch, U., Fleitmann, D., Harrison, G., Hood, L., Luterbacher, J., Meehl, G. A., Shindell, D., van Geel, B., and White, W.: Solar influences on climate, Rev. Geophys., 48, RG4001, 2010.

Griffiths, P. R. and de Haseth, J. A.: Fourier Transform Infrared Spectrometry, in: Chemical analysis. A series of monographs on analytical chemistry and its applications, edited by Elving, P. J. and Winefordner, J. D., vol. 83, John Wiley & Sons, Inc., 1986.

Hamann, K.: Untersuchung des Trends halogenhaltiger Verbindungen in der Stratosphäre, Diploma thesis at the Institute for Meteorology and Climate Research (IMK-ASF), University of Karlsruhe, 2007.

Hase, F.: Inversion von Spurengasprofilen aus hochaufgelösten bodengebundenen FTIR-Messungen in Absorption, Wissenschaftliche Berichte, FZKA-Report No. 6512, Forschungszentrum Karlsruhe, Germany, 2000.

Hase, F., Blumenstock, T., and Paton-Walsh, C.: Analysis of the instrumental line shape of high-resolution Fourier transform IR spectrometers with gas cell measurements and new retrieval software, Appl. Opt., 38, 3417–3422, 1999.

Hase, F., Hannigan, J. W., Coffey, M. T., Goldman, A., Höpfner, M., Jones, N. B., Rinsland, C. P., and Wood, S. W.: Intercomparison of retrieval codes used for the analysis of high-resolution, ground-based FTIR measurements, J. Quant. Spectrosc. Rad. Transfer, 87, 25–52, 2004.

IPCC: Intergovernmental Panel on Climate Change: Climate Change 2001: Synthesis Report. A Contribution of Working Groups I, II and III to the Third Assessment Report of the Intergovernmental Panel on Climate Change, edited by: Watson, R. T. and the Core Writing Team, Cambridge University Press, Cambridge, UK, and New York, USA, 2001.

IPCC: Intergovernmental Panel on Climate Change: Climate Change 2007: The Physical Science Basis. Contribution of Working Group I to the Fourth Assessment Report of the Intergovernmental Panel on Climate Change [Solomon, S., D. Qin, M. Manning, Z. Chen, M. Marquis, K.B. Averyt, M.Tignor and H.L. Miller (eds.)], Cambridge University Press, Cambridge, UK and New York, USA, 2007.

Jöckel, P., Sander, R., Kerkweg, A., Tost, H., and Lelieveld, J.: Technical Note: The Modular Earth Submodel System (MESSy) - a new approach towards Earth System Modeling, Atmos. Chem. Phys., 2005.

Jöckel, P., Tost, H., Pozzer, A., Brühl, C., Buchholz, J., Ganzeveld, L., Hoor, P., Kerkweg, A., Lawrence, M. G., Sander, R., Steil, B., Stiller, G., Tanarhte, M., Taraborrelli, D., van Aardenne, J., and Lelieveld, J.: The atmospheric chemistry general circulation model ECHAM5/MESSy1: consistent simulation

of ozone from the surface to the mesosphere, Atmos. Chem. Phys., 6, 5067–5104, doi:10.5194/acp-6-5067-2006, 2006.

Jones, A., Urban, J., Murtagh, D. P., Sanchez, C., Walker, K. A., Livesey, N. J., Froidevaux, L., and Santee, M. L.: Analysis of HCl and ClO time series in the upper stratosphere using satellite data sets, Atmos. Chem. Phys., 11, 5321–5333, 2011.

Kirner, O.: Prozessstudien der stratosphärischen Chemie und Dynamik mit Hilfe des Chemie-Klima-Modells ECHAM5/MESSy1, Dissertation am Institut für Meteorologie und Klimaforschung der Universität Karlsruhe (TH) und des Forschungszentrums Karlsruhe, 2008.

Kirner, O. and Ruhnke, R.: The development of ozone in the Stratosphere and Mesosphere performed in EMAC long-term simulations with different boundary conditions for CO_2, CH_4, N_2O, and ODS, Poster at the European Geosciences Union (EGU) General Assembly, Vienna, April 22–27, 2012.

Kohlhepp, R., Barthlott, S., Blumenstock, T., Hase, F., Kaiser, I., Raffalski, U., and Ruhnke, R.: Trends of HCl, $ClONO_2$ and HF column abundances from ground-based FTIR measurements in Kiruna (Sweden) in comparison with KASIMA model calculations, Atmos. Chem. Phys., 11, 4669–4677, 2011.

Kohlhepp, R., Ruhnke, R., Chipperfield, M. P., de Mazière, M., Notholt, J., Barthlott, S., Batchelor, R. L., Blatherwick, R. D., Blumenstock, T., Coffey, M. T., Duchatelet, P., Fast, H., Feng, W., Goldman, A., Griffith, D. W. T., Hamann, K., Hannigan, J. W., Hase, F., Jones, N. B., Kagawa, A., Kaiser, I., Kasai, Y., Kirner, O., Kouker, W., Lindenmaier, R., Mahieu, E., Mittermeier, R. L., Monge-Sanz, B., Murata, I., Nakajima, H., Morino, I., Palm, M., Paton-Walsh, C., Reddmann, T., Rettinger, M., Rinsland, C. P., Rozanov, E., Schneider, M., Senten, C., Sinnhuber, B.-M., Smale, D., Strong, K., Sussmann, R., Taylor, J. R., Vanhaelewyn, G., Warneke, T., Whaley, C., Wiehle, M., and Wood, S. W.: Observed and simulated time evolution of HCl, $ClONO_2$, and HF total column abundances, Atmos. Chem. Phys., 12, 3527–3557, 2012.

Kramer, I.: Zeitreihen troposphärischer Spurengase abgeleitet aus bodengebundenen FTIR-Messungen, Wissenschaftliche Berichte, FZKA-Report No. 7297, Forschungszentrum Karlsruhe, Germany, 2007.

Kraus, H.: Die Atmosphäre der Erde. Eine Einführung in die Meteorologie, Springer-Verlag Berlin, Heidelberg, 3 edn., 2004.

Labitzke, K. and van Loon, H.: Associations between the 11-year solar cycle, the QBO and the atmosphere. Part I: the troposphere and stratosphere in the northern hemisphere in winter, J. Atmos. Terr. Phys., 50, No.3, 197–206, 1988.

Lait, L., Newman, P., and Schoeberl, R.: Using the Goddard Automailer, URL `http://code916.gsfc.nasa.gov/Dataservices`, 2005.

Lary, D. J., Waugh, D. W., Douglass, A. R., Stolarski, R. S., Newman, P. A., and Mussa, H.: Variations in stratospheric inorganic chlorine between 1991 and 2006, Geophys. Res. Lett., 34, 2007.

Legrand, M. R., Stordal, F., Isaksen, I. S. A., and Rognerud, B.: A model study of the stratospheric budget of odd nitrogen, including effects of solar cycle variations, Tellus, 41B, 413–426, 1989.

Lindenmaier, R., Strong, K., Batchelor, R. L., Chipperfield, M. P., Daffer, W. H., Drummond, J. R., Duck, T. J., Fast, H., Feng, W., Fogal, P. F., Kolonjari, F., Manney, G. L., Manson, A., Meek, C., Mittermeier, R. L., Nott, G. J., Perro, C., and Walker, K. A.: Unusually low ozone, HCl, and HNO3 column measurements at Eureka, Canada during winter/spring 2011, Atmos. Chem. Phys., 12, 3821–3835, doi:10.5194/acp-12-3821-2012, 2012.

Liou, K.-N.: An introduction to atmospheric radiation, Academic Press, Inc., Orlando, Florida, USA, 1980.

Lu, H., Gray, L. J., Baldwin, M. P., and Jarvis, M. J.: Life cycle of the QBO-modulated 11-year solar cycle signals in the Northern Hemispheric winter, Q. J. R. Meteorol. Soc., 135, 1030–1043, 2009.

McLinden, C. A. and Fioletov, V.: Quantifying stratospheric ozone trends: Complications due to stratospheric cooling, Geophys. Res. Lett., 38, L03 808, doi:10.1029/2010GL046012, 2011.

Meier, A., Toon, G. C., Rinsland, C. P., Goldman, A., and Hase, F.: Spectroscopic atlas of atmospheric microwindows in the middle infra-red, IRF Technical Report 048, 2004.

Meschede, D.: Gerthsen Physik, Springer Verlag, Berlin, Heidelberg, New York, 21 edn., 2002.

Mikuteit, S.: Trendbestimmung stratosphärischer Spurengase mit Hilfe bodengebundener FTIR-Messungen, Wissenschaftliche Berichte, FZKA-Report No. 7385, Forschungszentrum Karlsruhe, Germany, 2008.

Molina, L. T. and Molina, M. J.: Production of Cl_20_2 from the Self-Reaction of the ClO Radical, J. Phys. Chem., 91, 433–436, 1987.

Molina, M. J. and Rowland, F. S.: Stratospheric sink for chlorofluoromethanes: chlorine atom-catalysed destruction of ozone, Nature, 249, 810–812, 1974.

Müller, R.: Introduction, in: Stratospheric Ozone Depletion and Climate Change, edited by Müller, R., chap. 1, RSC Publishing, Cambridge, UK, 2012.

Muncaster, R., Bourqui, M. S., Chabrillat, S., Viscardy, S., Melo, S., and Charbonneau, P.: Modelling the effects of (short-term) solar variability on stratospheric chemistry, Atmos. Chem. Phys. Disc., 11, 32 455–32 497, 2011.

Nakicenovic, N., Alcamo, J., Davis, G., de Vries, B., Fenhann, J., Gaffin, S., Gregory, K., Grübler, A., Jung, T. Y., Kram, T., Rovere, E. L. L., Michaelis, L., Mori, S., Morita, T., Pepper, W., Pitcher, H., Price, L., Riahi, K., Roehrl, A., Rogner, H.-H., Sankovski, A., Schlesinger, M., Shukla, P., Smith, S., Swart, R., van Rooijen, S., Victor, N., and Dadi, Z.: Special Report on Emissions Scenarios: A Special Report of Working Group III of the Intergovernmental Panel on Climate Change, Cambridge University Press, Cambridge, UK, URL http://www.grida.no/climate/ipcc/emission/index.htm, 2000.

Newchurch, M. J., Yang, E.-S., Cunnold, D. M., Reinsel, G. C., Zawodny, J. M., and Russell, J. M. I.: Evidence for slowdown in stratospheric ozone loss: First stage of ozone recovery, J. Geophys. Res., 108, 4507, 2003.

Newman, P. A., Daniel, J. S., Waugh, D. W., and Nash, E. R.: A new formulation of equivalent effective stratospheric chlorine (EESC), Atmos. Chem. Phys., 7, 4537–4552, 2007.

Paltridge, G. W. and Platt, C. M. R.: Developments in Atmospheric Science, vol. 5, Elsevier Scientific Publishing Company, Amsterdam, Oxford, New York, 1976.

Petty, G. W.: A first course in atmospheric radiation, Sundog Publishing, Madison, Wisconsin, USA, 2004.

Pidwirny, M.: Introduction to the atmosphere, in: Fundamentals of Physical Geography, 2 edn., URL http://www.physicalgeography.net/fundamentals/chapter7.html, 2006.

Plumb, R. A.: Stratospheric Transport, J. Meteor. Soc. Japan, 80, 793–809, 2002.

Ravishankara, A. R., Daniel, J. S., and Portmann, R. W.: Nitrous Oxide (N_2O): The Dominant Ozone-Depleting Substance Emitted in the 21st Century, Science, 326, 123, doi:10.1126/science.1176985, 2009.

Reisinger, A. R., Jones, N. B., Matthews, W. A., and Rinsland, C. P.: Southern hemisphere mid-latitude ground based measurements of $ClONO_2$, method of analysis, seasonal cycle, and long-term trend, J. Geophys. Res., 100, 23 183–23 193, 1995.

Rinsland, C. P., Levine, J. S., Goldman, A., Sze, N. D., Ko, M. K. W., and Johnson, D. W.: Infrared measurements of HF and HCl total column abundances above Kitt Peak, 1997-1990: Seasonal cycles, long-term increases, and comparisons with model calculations, J. Geophys. Res., 96, 15 523–15 540, 1991.

Rinsland, C. P., Nicholas, B. J., Connor, B. J., Logan, J. A., Pougatchev, N. S., Goldman, A., Murcray, F. J., Stephen, T. M., Pine, A. S., Zander, R., Mahieu, E., and Demoulin, P.: Northern and southern hemisphere ground-based infrared spectroscopic measurements of tropospheric carbon monoxide and ethane, J. Geophys. Res., 103, 28 197–28 218, 1998.

Rinsland, C. P., Mahieu, E., Zander, R., Jones, N. B., Chipperfield, M. P., Goldman, A., Anderson, J., III, J. M. R., Demoulin, P., Notholt, J., Toon, G. C., Blavier, J.-F., Sen, B., Sussmann, R., Wood, S. W., Meier, A., Griffith, D. W. T., Chiou, L. S., Murcray, F. J., Stephen, T. M., Hase, F., Mikuteit, S., Schulz, A., and Blumenstock, T.: Long-term trends of inorganic, J. Geophys. Res., 108, 4252, 2003.

Rodgers, C. D.: Inverse Methods for Atmospheric Sounding: Theory and Praxis, World Scientific Publishing Co., Singapore, 2000.

Roeckner, E., Bäuml, G., Bonaventura, L., Brokopf, R., Esch, M., Giorgetta, M., Hagemann, S., Kirchner, I., Kornblueh, L., Manzini, E., Rhodin, A., Schlese, U., Schulzweida, U., and Tompkins, A.: The atmospheric general circulation model ECHAM5. PART I: Model description, MPI-Report 349, Hamburg, Germany, 2003a.

Roeckner, E., Brokopf, R., Esch, M., Giorgetta, M., Hagemann, S., Kornblueh, L., Manzini, E., Schlese, U., and Schulzweida, U.: The atmospheric general circulation model ECHAM5. PART II: Sensitivity of Simulated Climate to Horizontal and Vertical Resolution, MPI-Report 354, Hamburg, Germany, 2003b.

Rosenfield, J. E., Frith, S. M., and Stolarski, R. S.: Version 8 SBUV ozone profile trends compared with trends from a zonally averaged chemical model, J. Geophys. Res., 110, D12 302, doi: 10.1029/2004JD005466, 2005.

Rothman, L. S., Gamache, R. R., Tipping, R. H., Rinsland, C. P., Smith, M. A. H., Benner, D. C., Devi, V. M., Flaud, J.-M., Camy-Peyret, C., Perrin, A., Goldman, A., Massie, S. T., Brown, L. R., and Toth, R. A.: The HITRAN molecular database: editions of 1991 and 1992, J. Quant. Spectrosc. Ra., 48, 469–507, 1992.

Rothman, L. S., Rinsland, C. P., Goldman, A., Massie, S. T., Edwards, D. P., Flaud, J.-M., Perrin, A., Camy-Peyret, C., Dana, V., Mandin, J.-Y., Schroeder, J., Mccann, A., Gamache, R. R., Wattson, R. B., Yoshino, K., Chance, K. V., Jucks, K. W., Brown, L. R., Nemtchinov, V., and Varanasi, P.: The HITRAN molecular spectroscopic database and HAWKS (HITRAN atmospheric workstation): 1996 edition, J. Quant. Spectrosc. Ra., 60, 665–710, 1998.

Rothman, L. S., Barbe, A., Benner, D. C., Brown, L. R., Camy-Peyret, C., Carleer, M. R., Chance, K., Clerbaux, C., Dana, V., Devi, V. M., Fayt, A., Flaud, J.-M., Gamache, R. R., Goldman, A., Jacquemart, D., Jucks, K. W., Lafferty, W. J., Mandin, J.-Y., Massie, S. T., Nemtchinov, V., Newnham, D. A., Perrin, A., Rinsland, C. P., Schroeder, J., Smith, K. M., Smith, M. A. H., Tang, K., Toth, R. A., Auwera, J. V., Varanasi, P., and Yoshino, K.: The HITRAN molecular spectroscopic database: edition of 2000 including updates through 2001, J. Quant. Spectrosc. Ra., 82, 5–44, 2003.

Rothman, L. S., Jacquemart, D., Barbe, A., Benner, D. C., Birk, M., Brown, L. R., Carleer, M. R., Jr., C. C., Chance, K., Coudert, L. H., Dana, V., Devi, V. M., Flaud, J.-M., Gamache, R. R., Goldman,

A., Hartmann, J.-M., Jucks, K. W., Maki, A. G., Mandin, J.-Y., Massie, S. T., Orphal, J., Perrin, A., Rinsland, C. P., Smith, M. A. H., Tennyson, J., Tolchenov, R. N., Toth, R. A., Auwera, J. V., Varanasi, P., and Wagner, G.: The HITRAN 2004 molecular spectroscopic database, J. Quant. Spectrosc. Ra., 96, 139–204, 2005.

Sander, R., Kerkweg, A., Jöckel, P., and Lelieveld, J.: Technical note: The new comprehensive atmospheric chemistry module MECCA, Atmos. Chem. Phys., 5, 445–450, doi:10.5194/acp-5-445-2005, 2005.

Sander, S. P., Friedl, R. R., Golden, D. M., Kurylo, M. J., Huie, R. E., Orkin, V. L., Moortgat, G. K., Ravishankara, A. R., Kolb, C. E., and Molina, M. J.: Chemical Kinetics and Photochemical Data for Use in Atmospheric Studies, Evaluation Number 14, JPL Publication 02-25, 2002.

Sander, S. P., Friedl, R. R., Golden, D. M., Kurylo, M. J., Moortgat, G. K., Keller-Rudek, H., Wine, P. H., Ravishankara, A. R., Kolb, C. E., Molina, M. J., Finlayson-Pitts, B. J., Huie, R. E., and Orkin, V. L.: Chemical Kinetics and Photochemical Data for Use in Atmospheric Studies, Evaluation Number 15, JPL Publication 06-2, Jet Propulsion Laboratory, Pasadena, 2006.

Sander, S. P., Abbatt, J., Barker, J. R., Burkholder, J. B., Friedl, R. R., Golden, D. M., Huie, R. E., Kolb, C. E., Kurylo, M. J., Moortgat, G. K., Orkin, V. L., and Wine, P. H.: Chemical Kinetics and Photochemical Data for Use in Atmospheric Studies, Evaluation No. 17, JPL Publication 10-6, Jet Propulsion Laboratory, Pasadena, URL `http://jpldataeval.jpl.nasa.gov`, 2011.

Schneider, M., Blumenstock, T., Chipperfield, M. P., Hase, F., Kouker, W., Reddmann, T., Ruhnke, R., Cuevas, E., and Fischer, H.: Subtropical trace gas profiles determined by ground-based FTIR spectroscopy at Izaña (28° N, 16° W): Five-year record, error analysis, and comparison with 3-D CTMs, Atmos. Chem. Phys., 5, 153–167, 2005.

Seinfeld, J. H. and Pandis, S. N.: Atmospheric chemistry and physics: From air pollution to climate change, John Wiley & Sons, Inc., USA, 1998.

Sepúlveda, E., Schneider, M., Hase, F., García, O. E., Gomez-Pelaez, A., Dohe, S., Blumenstock, T., and Guerra, J. C.: Long-term validation of total and tropospheric column-averaged CH4 mole fractions obtained by mid-infrared ground-based FTIR spectrometry, Atmos. Meas. Tech. Discuss., 5, 1381–1430, doi:10.5194/amtd-5-1381-2012, 2012.

Sinnhuber, B.-M., von der Gathen, P., Sinnhuber, M., Rex, M., König-Langlo, G., and Oltmans, S. J.: Large decadal scale changes of polar ozone suggest solar influence, Atmos. Chem. Phys., 6, 1835–1841, doi:10.5194/acp-6-1835-2006, 2006.

SPARC-CCMVal: SPARC Report on the Evaluation of Chemistry-Climate Models, V. Eyring, T. G. Shepherd, D. W. Waugh (Eds.), SPARC Report No. 5, WCRP-132, WMO/TD-No. 1526, URL `http://www.atmosp.physics.utoronto.ca/SPARC`, 2010.

Steinbrecht, W., Hassler, B., Claude, H., Winkler, P., and Stolarski, R. S.: Global distribution of total ozone and lower stratospheric temperature variations, Atmos. Chem. Phys., 3, 1421–1438, 2003.

Stiller, G. P., von Clarmann, T., Höpfner, M., Glatthor, N., Grabowski, U., Kellmann, S., Kleinert, A., Linden, A., Milz, M., Reddmann, T., Steck, T., Fischer, H., Funke, B., Lopez-Puertas, M., and Engel, A.: Global distribution of mean age of stratospheric air from MIPAS SF_6 measurements, Atmos. Chem. Phys., 8, 677–695, 2008.

Taylor, J. R.: Fehleranalyse: Eine Einführung in die Untersuchung von Unsicherheiten in physikalischen Messungen, VCH Verlagsgesellschaft mbH, Weinheim, Germany, 1988.

Tipler, P. A.: Physik, Spektrum Akad. Verl., Heidelberg, Berlin, Oxford, 1 edn., 1994.

Vigouroux, C., de Mazière, M., Demoulin, P., Servais, C., Hase, F., Blumenstock, T., Kramer, I., Schneider, M., Mellqvist, J., Strandberg, A., Velazco, V., Notholt, J., Sussmann, R., Stremme, W., Rockmann, A., Gardiner, T., Coleman, M., and Woods, P.: Evaluation of tropospheric and stratospheric ozone trends over Western Europe from ground-based FTIR network observations, Atmos. Chem. Phys., 8, 6865–6886, 2008.

von Clarmann, T.: Zur Fernerkundung der Erdatmosphäre mittels Infrarotspektrometrie: Rekonstruktionstheorie und Anwendung, Wissenschaftliche Berichte, FZKA-Report No. 6928, Forschungszentrum Karlsruhe, Germany, 2003.

von Hobe, M. and Stroh, F.: Stratospheric Halogen Chemistry, in: Stratospheric Ozone Depletion and Climate Change, edited by Müller, R., chap. 3, RSC Publishing, Cambridge, UK, 2012.

Wallace, L. and Livingston, W. C.: Spectroscopic observations of atmospheric trace gases over Kitt Peak, 3, Long-term trends of hydrogen chloride and hydrogen fluoride from 1978 to 1990, J. Geophys. Res., 96, 15 513–15 521, 1991.

Wallace, L. and Livingston, W. C.: Thirty-five year trend of hydrogen chloride amount above Kitt Peak, Arizona, Geophys. Res. Lett., 34, L16 805, 2007.

Wallace, L., Livingston, W., and Hall, D. N. B.: A twenty-five year record of stratospheric hydrogen chloride, Geophys. Res. Lett., 24, 2363–2366, 1997.

Washenfelder, R. A., Toon, G. C., Blavier, J.-F., Yang, Z., Allen, N. T., Wennberg, P. O., Vay, S. A., Matross, D. M., and Daube, B. C.: Carbon dioxide column abundances at the Wisconsin Tall Tower site, J. Geophys. Res.-Atmos., 111, D22 305, 2006.

Weatherhead, E. C., Reinsel, G. C., Tiao, G. C., Meng, X.-L., Choi, D., Cheang, W.-K., Keller, T., DeLuisi, J., Wuebbles, D. J., Kerr, J. B., Miller, A. J., Oltmans, S. J., and Frederick, J. E.: Factors affecting the detection of trends: Statistical considerations and applications to environmental data, J. Geophys. Res., 103, 17 149–17 161, 1998.

WMO: Scientific Assessment of Ozone Depletion: 2002, World Meteorological Organization: Global ozone research and monitoring project, Report no. 47, Geneva, Switzerland, 2003.

WMO: Scientific Assessment of Ozone Depletion: 2006, World Meteorological Organization: Global ozone research and monitoring project, Report no. 50, Geneva, Switzerland, 2007.

WMO: Scientific Assessment of Ozone Depletion: 2010, World Meteorological Organization: Global ozone research and monitoring project, Report no. 52, Geneva, Switzerland, 2011.

Zander, R., Roland, G., Delbouille, L., Saval, A., Farmer, C. B., and Norton, R. H.: Column abundance and the long-term trend of hydrogen chloride (HCl) above the Jungfraujoch station, J. Atmos. Chem., 5, 395–404, 1987.

Zander, R., Mahieu, E., Demoulin, P., Duchatelet, P., Roland, G., Servais, C., Mazière, M. D., Reimann, S., and Rinsland, C. P.: Our changing atmosphere: Evidence based on long-term infrared solar observations at the Jungfraujoch since 1950, Sci. Total Environ., 391, 184–195, 2008.